ISSN 1028-8546

Volume XXV, Number 4
Section: En
December, 2019

Azerbaijan Journal of Physics

Fizika

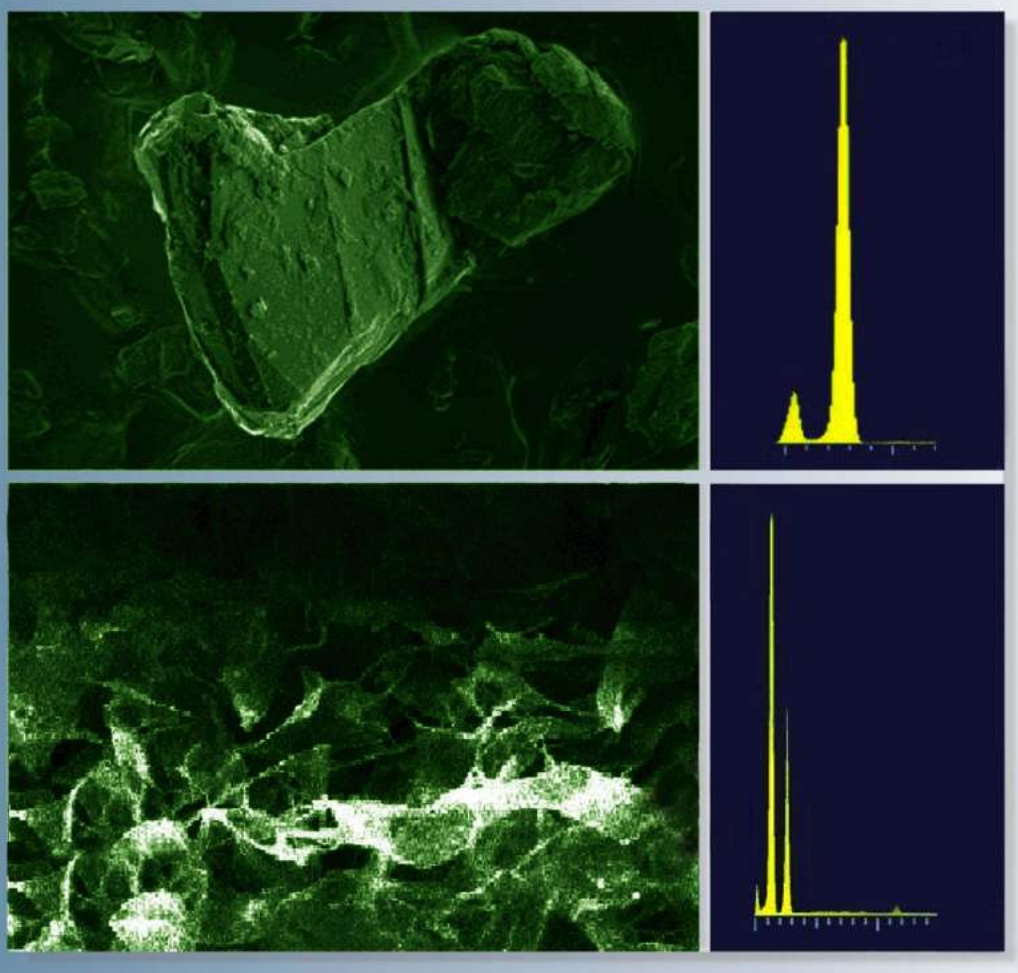

www.physics.gov.az

G.M. Abdullayev Institute of Physics
Azerbaijan National Academy of Sciences
Department of Physical, Mathematical and Technical Sciences

Published from 1995
Ministry of Press and Information
of Azerbaijan Republic,
Registration number 514, 20.02.1995

ISSN 1028-8546
vol. XXV, Number 04, 2019
Series: En

Azerbaijan Journal of Physics

FIZIKA

G.M. Abdullayev Institute of Physics
Azerbaijan National Academy of Sciences
Department of Physical, Mathematical and Technical Sciences

PUBLISHING OFFICE

131, H. Javid ave., AZ-1143, Baku
ANAS, G.M. Abdullayev Institute of Physics

Tel.: (99412) 539-51-63, 539-32-23
Fax: (99412) 537-22-92
E-mail: jophphysics@gmail.com
Internet: www.physics.gov.az
https://jophphysics.wixsite.com/ajpphysics

Published at "**AZERİ-DİZAYN**"
196, Nizami str., Baku
Typographer: Filipp Podosinnikov

Sent for printing on: __.__. 201_
Printing approved on: __.__. 201_
Physical binding:_____
Number of copies:_____200
Order:_____

It is authorized for printing:

VISCOSYMETRIC AND DENSYTOMETRIC STUDY IN WATER - PEG-KCl SYSTEMS

E.A. MASIMOV, B.G. PASHAYEV, N.F. ORUJOVA
Baku State University, Physics Department
E-mail: p.g.bakhtiyar@gmail.com

In this work, the dynamic viscosity and density of water-PEG-KCl was measured in the temperature range 293.15-323.15K and 0-0.001 mole fraction of PEG. PEG fractions with a molar mass 1000, 1500, 3000, 4000, 6000 were investigated and the concentration of KCl was considered to be 0.01-mole fraction. Using the results of the experiment, the activation parameters of the viscous flow and the partial molar volumes of PEG were calculated. It has been established that, with increasing concentration and the molecular mass, the solution becomes more structured.

Keywords: water solution, PEG, KCl, activation parameters of viscous flow, partial molar volume.
PACS: 61.20. Ne, 66.20.+d, 82.60.Lf, 61.25.Hq

1. INTRODUCTION

Polyethylene glycol (PEG) is one of the most studied polymers, as it is widely used in many industries (pharmacology, cosmetology, biotechnology etc.) [1-9]. One reason for the extensive use of PEG is that it has many molecular mass fractions. The PEG does not adversely affect the organism's immune system, it does not have toxic properties and is quickly cleansed from the body [1]. The PEG's large molecular mass fractions are heat-resistant and it is resistant to atmospheric moisture. PEG - all the molecular mass fractions are well soluble in water. It is supposed that (OH) groups in the PEG macromolecule to form hydrogen bonds with the water molecule of $-O-$ and $-H$ atoms. CH_2 groups in the PEG macromolecule create the hydrophobic effect [10]. Most of the PEG functions occur in the water environment. Therefore, studying the structural properties of water-PEG systems and the study of structural changes in the solution by adding the third component has great scientific and practical significance.

Here the structural features of the system of water-PEG-KCl at temperature 293.15-323.15 K and 0-0.001 partial molar concentration of PEG was investigated by means of methods viscosimetry and pycnometer. The dynamic viscosity and density of aqueous solutions were measured at observed temperature and concentration intervals. Based on experimental results dependence of activation Gibbs energy of viscous flow ($\Delta G_\eta^{\neq}$), activation enthalpy of viscous flow ($\Delta H_\eta^{\neq}$), activation entropy of viscous flow ($\Delta S_\eta^{\neq}$) and the partial molar volume of PEG ($\tilde{V}$) in solution of studied systems on the concentration of PEG were analyzed.

2. EXPERIMENTAL AND THEORETICAL PART

Objects of study: water-PEG-KCl was used as our objects of research. PEG fractions with a molar mass 1000, 1500, 3000, 4000, 6000 were investigated and the concentration of KCl was considered to be 0.01 mole fraction. Used PEG and KCl are chemical pure. Bidistilled water was used in the preparation of the solutions. The viscosity was measured by capillary viscosimeter and density was measured by pycnometer.

Due to activation Gibbs energy of viscous flow ($\Delta G_\eta^{\neq}$) according to Frenkel and Eyring theory [10] of liquid viscous flow

$$\Delta G_\eta^{\neq} = RT \ln \frac{\eta}{\eta_0} \tag{1}$$

is defined by this expression. Due to Eyring theory [10] $\eta_0 = \frac{N_A h \rho}{M}$. Here is R- universal gas constant, N_A - is the Avogadro number, h-is the Planck's constant, and M-is the molecular weight of solution, determined according to equation $M = \sum_{i=1}^{N} x_i M_i$. Here x_i and M_i are the molar fraction and molar weight of the i-th component, respectively. Dynamic viscosity (η) and density (ρ) of the solution at different temperatures were determined experimentally.

The activation enthalpy of viscous flow ($\Delta H_\eta^{\neq}$) was determined by the equation [10-12]

$$\Delta H_\eta^{\neq} = R \frac{\partial \ln \cdot (\eta / \eta_0)}{\partial (1/T)} \tag{2}$$

Thus, $\Delta G_\eta^{\neq}$ and $\Delta H_\eta^{\neq}$ were calculated by (1) and (2). The $\Delta G_\eta^{\neq}$ and $\Delta H_\eta^{\neq}$ values were used for determining the activation entropy of viscous flow ($\Delta S_\eta^{\neq}$) by the known thermodynamic equation [10]

$$\Delta G_\eta^{\neq} = \Delta H_\eta^{\neq} - T\Delta S_\eta^{\neq} \tag{3}$$

The partial molar volume ($\tilde{V}$) of the solute in solution was determined by the equation [10, 13]

$$\tilde{V} = V_m + (1-x) \cdot \left(\frac{\partial V_m}{\partial x} \right)_{p,T} \tag{4}$$

where V_m is the molar volume of the solution:

131, H. Javid ave., AZ-1143, Baku
ANAS, G.M.Abdullayev Institute of Physics
E-mail: jophphysics@gmail.com

$$V_m = \frac{M}{\rho} = \frac{1}{\rho}\sum_{i=1}^{N} x_i M_i \,.$$

3. RESULTS AND DISCUSSION

The system of water-PEG-KCl at the temperature 293,15 K dependence of the activation Gibbs energy of viscous flow ($\Delta G_\eta^{\neq}$), the activation enthalpy of viscous flow ($\Delta H_\eta^{\neq}$) on the PEG's concentration is shown in table 1 and 2, dependence activation entropy of viscous flow ($\Delta S_\eta^{\neq}$) on the PEG concentration (x) is shown in fig. 1.

It seems in table 1, table 2 and fig. 1, $\Delta G_\eta^{\neq}$, $\Delta H_\eta^{\neq}$ and $\Delta S_\eta^{\neq}$ the parameters are increased by increasing the concentration at the given temperature and increasing with the increased molar mass at the given temperature and concentration.

It should be noted that, $\Delta G_\eta^{\neq}$ is the energy used for activation 1 *mole* molecule, $\Delta H_\eta^{\neq}$ represents the changes in the solution in terms of energy and $\Delta S_\eta^{\neq}$ characterized the changes in solution in terms of structure. Thus, increased $\Delta G_\eta^{\neq}$ with the growth of concentration indicates that more energy can be consumed for overcoming the potential of molecule, while increase in $\Delta H_\eta^{\neq}$ indicates the system has steadier structure, increase in $\Delta S_\eta^{\neq}$ determines the system is becoming more structured [8-12]. Due to dependence of viscous flow parameters on concentration (table 1, table 2 and fig. 1) it is possible to tell that, in process of increase in concentration of PEG in solution has a stronger structure and more structured.

Structural properties of aqueous solutions are also characterized by the partial molar volume of components of solution. It is known that the partial molar volume of *i*-th component is equivalent to a change of volume at the addition of 1 *mol* from this component [10, 13]. The dependence of partial molar volume ($\tilde{V}$) of PEG on concentration (x) of PEG in system water-PEG-KCl for PEG's various molar mass at 293.15 K is shown in table 3.

Table 3 shows that partial molar volume of PEG in solution decreases with increase in concentration at the given temperature and the partial molar volume of PEG increase with increasing molecular mass at the given temperature and concentration. Calculation shows that partial molar volume $\left(\frac{\tilde{V}}{n}\right)_{av}$ of PEG in one monomer at given temperature and concentration practically doesn't depend on the molecular mass of PEG. In fig. 2 the dependence of PEG of various molar mass of average value of partial molar volume in a monomer on concentration at temperature 293.15 *K* is shown. We can describe this dependence with the equation

$$\left(\frac{\tilde{V}}{n}\right)_{av} = 1907623{,}2x^2 - 5694{,}2x + 38{,}3$$

It is possible to assume that the volume portion of big sizes associations in space, the fractional share of its separate parts is less than the sum of volume portion of and vice versa. According to model of the two-structured water [10, 14, 15], water consists of clusters of the different size and clusters of molecules of free liquid which are attached to hydrogen binding. Due to dependence of partial molar volume on concentration it is possible to assume that the molecules of PEG are connected first of all by hydrogen binding with free molecules of water. It leads to reduction of partial molar volume of PEG due to increasing in concentration in solution. This indicates that the solution has become more structured due to increase in PEG concentration.

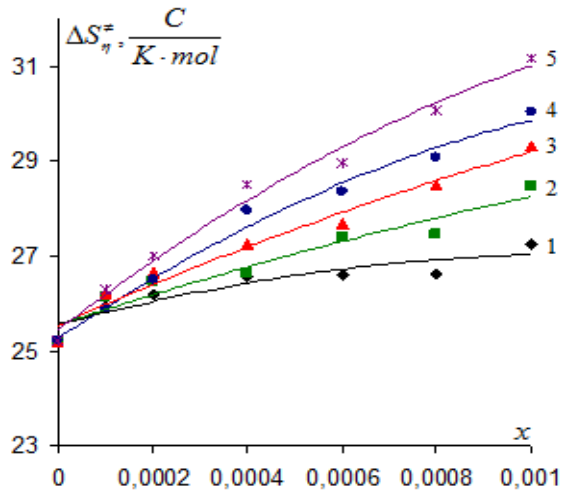

Fig. 1. Dependence activation entropy of viscous flow of water-PEG-KCl system on PEG concentration ($x_{KCl} = 0.01$, $T = 293.15K$).1-PEG(1000), 2-PEG (1500), 3 -PEG (3000), 4-PEG (4000), 5 -PEG (6000)

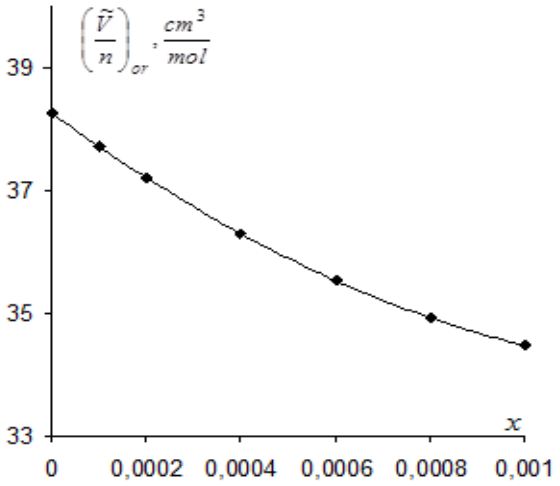

Fig. 2. Dependence of the average value of the partial molar volume of the PEG per monomer on concentration of PEG in system water-PEG-KCl ($x_{KCl} = 0.01$ $T = 293.15K$)

Table 1

Dependence activation Gibbs energy of viscous flow ($\Delta G_{\eta}^{\neq}, J/mol$) of water-PEG-KCl system on PEG concentration (x) ($x_{KCl} = 0.01$, $T = 293.15K$)

x	$M_{PEG} = 1000$	$M_{PEG} = 1500$	$M_{PEG} = 3000$	$M_{PEG} = 4000$	$M_{PEG} = 6000$
0	9274	9274	9274	9274	9274
0.0001	9353	9444	9543	9592	10504
0.0002	9487	9585	9847	10177	11346
0.0004	9544	10009	10580	10909	13427
0.0006	9749	10297	10999	11502	15248
0.0008	9803	10883	11409	12371	16164
0.001	10051	11146	12061	13016	17572

Table 2

Dependence activation entalphy of viscous flow ($\Delta H_{\eta}^{\neq}, J/mol$) of water-PEG-KOH system on PEG concentration (x) ($x_{KCl} = 0.01$, $T = 293.15K$)

x	$M_{PEG} = 1000$	$M_{PEG} = 1500$	$M_{PEG} = 3000$	$M_{PEG} = 4000$	$M_{PEG} = 6000$
0	16665	16665	16665	16665	16665
0.0001	17007	17110	17230	17180	18214
0.0002	17156	17340	17660	17948	19266
0.0004	17339	17814	18568	19106	21784
0.0006	17546	18331	19113	19818	23736
0.0008	17599	18932	19767	20893	24981
0.001	18041	19489	20657	21818	26712

Table 3

The dependence of the partial molar volume ($\tilde{V}, cm^3/mol$) of PEG in water-PEG-KCl systems on PEG concentration (x) ($x_{KCl} = 0.01$, $T = 293.15K$)

x	$M_{PEG} = 1000$	$M_{PEG} = 1500$	$M_{PEG} = 3000$	$M_{PEG} = 4000$	$M_{PEG} = 6000$
0	848	1310	2670	3602	5017
0.0001	837	1284	2632	3535	4983
0.0002	827	1261	2597	3471	4950
0.0004	811	1221	2534	3356	4889
0.0006	797	1189	2480	3258	4833
0.0008	788	1167	2436	3175	4782
0.001	781	1153	2403	3108	4736

4. CONCLUSION

Apparently, the dependence of both the activation entropy of viscous flow and the concentration of partial molar volume of the PEG in solution indicates that concentration as for both fractional PEGs taken at this temperature and for increase in molecular mass for the concentrated and various fractioned PEGs, the solutions becomes more structured. It is possible to assume that, in the studied system, around PEG's molecules water molecules are collected (first of all free molecules of water) by means of hydrogen bindings and certain size aggregates are formed. With increasing both concentration and molecular mass of PEG the number of such aggregates increases and their size increase, that leads to more structured solution. Indeed, since the K^+ and Cl^- ions are hydrated in the water-PEG-KCl system, the structure will be different from the structure of the water-PEG system.

[1] *J.H. Sung, D.C. Lee, H.J. Park.* Polymer, v. 48, p.p. 4205-4212, 2007.

[2] *Y. Chen.* Journal of Polymer Science: Part A: Polymer Chemistry, v. 42, p.2263-2271, 2004.

[3] *M.A. Sibileva, E.V. Tarasova.* Russian Journal of Physical Chemistry, v.78, №7, p.p. 1240-1244, 2004.

[4] *S.B.Kharchenko,R.M.Kannan.*Macromolecules, v. 36, p.407-415, 2003.

[5] *T. Furukawa, K. Ishizu*. Macromolecules, v. 36, p.p. 434-439, 2003.
[6] *F.F. Bailey, J.V. Koleske.* Poly (Ethylene Oxide). Academic press: New York, p. 173, 1976.
[7] *I.V.Shulyak, E.I.Grushova, A.M.Semenchenko*. Russian Journal of Physical Chemistry, v. 85, № 3, p.p. 419-422, 2011.
[8] *E.A. Masimov, B.G. Pashayev, H.Sh. Hasanov, Sh.N. Hajiyeva.* Russian Journal of Physical Chemistry, v. 93, № 6, p.p. 1054-1058, 2019.
[9] *E.A. Masimov, B.G. Pashayev, H.Sh. Hasanov.* Russian Journal of Physical Chemistry, v. 93, no.5, p.p. 779-781, 2019.
[10] *E.A. Masimov, H.Sh. Hasanov, B.G. Pashayev.* Liquid viscosity. Baku, "Publishing House Laman", p. 285, 2016.
[11] *E.A. Masimov, B.G. Pashayev, H.Sh. Hasanov, N.H. Hasanov*. Russian Journal of Physical Chemistry, v. 89, № 7, p. 1244-1247, 2015.
[12] *A.A. Tager.* Physico-chemistry of polymers. M.: Scientific world, p. 576, 2007.
[13] *P.Atkins, DePaula.* J. Physical chemistry. Oxford University Press. p. 1067, 2006.
[14] *G. Nemethy.* The structure of water and the thermodynamic properties of aqueous solutions. Istituto superiore di sanita-V.le Regina Elena, 299-Roma. vol. VI fascicolo speciale 1, p. 492-592, 1970.
[15] *V. Kalous, Z.Pavlichek.* Biophysical chemistry. Moscow «Mir», p. 267-273, 1985.

Received: 04.07.2019

ANALYSIS FIDUCIALLY DISTRIBUTIONS OF POSSIBLE REALIZATIONS OF TECHNICAL AND ECONOMIC PARAMETERS OF POWER UNITS

E.M. FARHADZADEH, A.Z. MURADALIYEV,
T.K. RAFIYEVA, A.A. RUSTAMOVA
Azerbaijan Scientific-Research and Design-Prospecting Institute of Energetic
94, H. Zardabi ave., AZ1012
e-mail: elmeht@rambler.ru

To fiducially distributions of multivariate random variables, i.e. random variables, which estimations depend from of some attributes and their versions concern. A bright example of multivariate random variables is technical and economic parameters of power units of power stations. Laws fiducially distributions depend on power units of factors (attributes) influencing an overall performance. Therefore, unlike set of one-dimensional random variables, fiducially distributions characterized not by the concrete law of distribution, and only experimentally established statistical function of distribution and the histogram. Boundary values fiducially interval defined not by a significance value, and the set combination of versions of attributes. At classification of multivariate data on the set significant versions of attributes, the number of possible realizations decreases. However, unlike a confidential interval of estimations of parameters of distribution of sample of general set, the width fiducially interval decreases, that corresponds to increase of accuracy of calculation of individual reliability. One of versions of possible realizations of technical and economic parameters is the realizations caused by "rough" mistakes at calculation or corresponding non-stationary modes. The automated system of recognition of these erroneous realizations essentially raises objectivity of comparison and ranging of power units. But development of algorithm of the automated system is preceded with the graphic analysis fiducially distributions of the technical and economic parameters, allowing to formulate corresponding criteria.

Keywords: accuracy, reliability, fiducially interval, safety, efficiency, power unit.
PACS: 84.30.Jc

1. INTRODUCTION

Transformation of technical and economic parameters (TEP) power units of thermal power stations (TPS), with the purpose of transition to integrated parameters, demands overcoming of some methodical difficulties. These difficulties caused:

Increase in relative number of units of the capital equipment (objects) which service life exceeds normative value [1]. For new objects, operational reliability and safety were consider provided as a factory the manufacturer and kept at performance of corresponding factory instructions and rules. In process of increase in service life of objects, the size of residual deterioration increases. Thus, instructions of instructions and rules all in a smaller measure correspond to a real technical condition of objects, i.e. their real reliability and safety. Considering, that replacement of objects at excess of normative term of their service on new is economically inexpedient, and practically - is unreal, the overall performance of these objects provided mainly intuitively. Thus, the personnel know, that reliability of work and safety of service of such objects have essentially decreased (essentially the number of obvious defects) increases, and possible consequences of this decrease became so significant, that have appeared inadmissible. Recommendations necessarily the organizations of maintenance service and repair of objects according to their technical condition known also. However, methodical instructions on maintenance service and repair of objects of "growing old" type are absent;

Having agreed, that at comparison of an overall performance of objects, which service life is close to normative and even more than normative term, it is necessary to consider not only profitability, but also reliability of work, and safety of service [2], it is necessary to have in view of, that the methodology of such account requires essential perfection. Moreover, there are no methods and algorithms of calculation of an integrated parameter of separate properties of an overall performance - reliability, profitability and safety. For example, it is impossible to compare safety of service of power units;

Statistical data about monthly average values TEP of power units depend on the big number of versions of attributes. It both capacity, and type of power units, their loading and an operating mode, a level of operation and service life, and many other things. Therefore, realizations TEP cannot be considered homogeneous and to carry to sample of general set. It is set of possible realizations of multivariate data. To apply to the statistical analysis of multivariate data known methods of the analysis for samples from general set, it is inadmissible [3]. At their use initial preconditions of these methods (type of the law of distribution, number of realization) are broken, that, in opinion of authors of these methods, leads to essential increase of risk of the erroneous decision. Methods of the statistical analysis of multivariate data are specific to each object and demand the further development;

The estimation of an integrated parameter of an overall performance can be executed on the basis of fiducially the approach [4]. For what it is necessary to develop corresponding algorithm and criterion of decision-making. Labor input and bulkiness of the manual account are so great, that necessity of transition to computer technologies does not raise the doubts. These technologies should come to the end with results of the decision of operational problems and be

131, H. Javid ave., AZ-1143, Baku
ANAS, G.M.Abdullayev Institute of Physics
E-mail: jophphysics@gmail.com

formalized in the form of the document providing methodical support of the personnel;

In present clause in section 2 the graphic analysis fiducially distributions TEP of boiler installations (BI) power units 300 MW on gas black oil fuel, in section 3 - the analysis of frontier intervals fiducially distributions (prigrin) is resulted, and in section 4 is given the conclusions of results of the analysis of distributions TEP.

2. ANALYSIS FIDUCIALLY DISTRIBUTIONS TEP

In [5, 6] we had been considered features of distribution of following four monthly average values TEP of BI power units 300 MW on gas black oil fuel:
- temperature of a feed water (T_{fw})with normalize value $\varepsilon(T_{fw})$ and statistical function fiducially distributions (s.f.f.d.) F*(T_{fw});
- the charge of the electric power in system of own needs (o.n) (E_t) with normalize value $\varepsilon(E_t)$ and s.f.f.d. $F^*(E_t)$;
- efficiency net (η_n) with normalize value $e(\eta_n)$ and s.f.f.d. $F^*(\eta_n)$;
- the specific charge of conditional fuel (b_f) with normalize value $\varepsilon(b_f)$ and s.f.f.d. $F^*(b_f)$.

Normalize values were calculated in conformity with following algorithm:

$$\text{If } A_i=1,\ \varepsilon_1(P_{i,j}) = (\overline{P_i^f} - P_{i,j}) / \overline{P_i^f} - \underline{P_i^f}$$
$$\text{If } A_i=1,\ \varepsilon_0(P_{i,j}) = (P_{i,j}) - \underline{P_i^f}) / \overline{P_i^f} - \underline{P_i^f} \quad (1)$$

Here, A-factor of orientation TEP. If with increase TEP overall performance BI will increase, A=1. Otherwise A=0; $P_{i,j}$ a-symbol of j-th possible realization of i-th TEP, with i=1,n_p and j=1,m_i, where n_p - number TEP, m_i - number of possible realizations of i-th TEP; $\underline{P_i^f}$ and $\overline{P_i^f}$ -accordingly, the bottom and the top boundary values fiducially interval of i-th TEP.

The essence of formulas for calculation of relative change $\varepsilon(P_{i,j})$ is simple enough. First, it is easy to notice, that $\varepsilon_1(P_{i,j}) + \varepsilon_0(P_{i,j}) = 1$. The formula for $\varepsilon_1(P_{i,j})$ is used, if $\overline{P_i^f}$ concerns to the most preferable realization TEP. For example, the high efficiency is more preferable than low efficiency. The deviation from $\overline{P_i^f}$ more, the an overall performance below. If the size $\underline{P_i^f}$ the formula applied for $\varepsilon_0(P_{i,j})$ is preferable. For example, small values of the charge of the electric power for own needs it is more preferable, than greater. It is established, that unlike a confidential interval, boundary values fiducially interval should will be defined at analysis TEP not "mechanically" proceeding from the set size of factor of the importance, in summary exceptions of set of possible values (for example, within a year) not typical realizations. "Rough" mistakes and possible realizations TEP concern to them in non-stationary operating modes BI.

Below we shall continue the graphic analysis and of some others independent TEP BI power units 300 MW with the purpose of transition to the generalized algorithm of automated analysis TEP of power units. Possible realizations of following TEP considered:

- temperature of leaving gases, T_{lg}, with A=0
- the charge of thermal energy on o.n., E_t with A=0
- factor of surplus of air, K_a, with A=0
- suction air on a path, ΔS, with A=0
- temperature of air after RWH, T_a, with A=1
- efficiency brutto, η_b, with A=1

In fig. 1 are resulted s.f.f.d. listed above absolute values TEP.

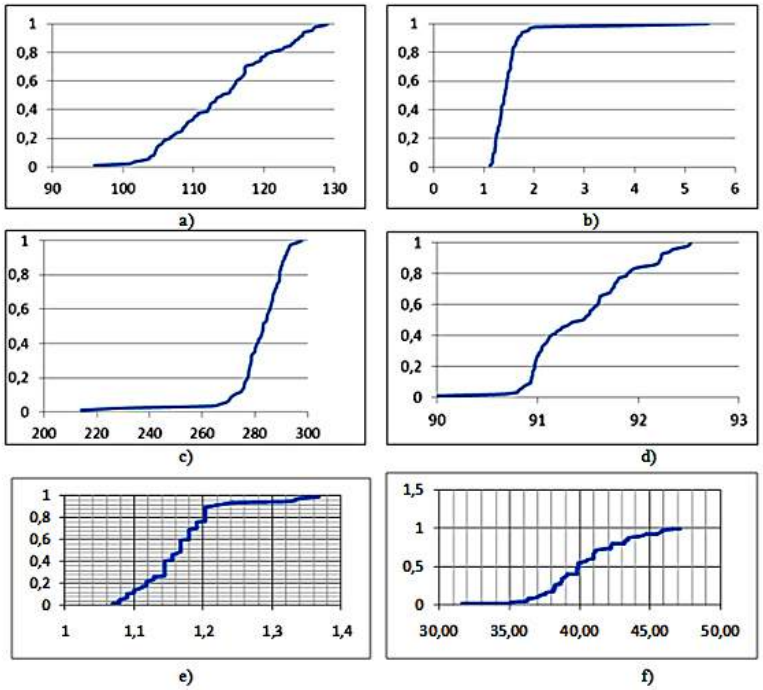

Fig. 1. Fiducially distributions of possible realizations TEP a - $F^*(T_{lg})$; b - $F^*(E_t)$; c - $F^*(T_a)$; d - $F^*(\eta_b)$; e - $F^*(K_a)$; f - $F^*(\Delta S)$.

As follows from this figure, for:

$$\left.\begin{array}{l}
\text{Fig. 1a } \left(\underline{T^f_{lg,\alpha/2}} - T_{lg,min}\right) = \left(T_{lg,max} - \overline{T^f_{lg,\alpha/2}}\right) \text{ at } A=0 \\
\text{Fig. 1b } \left(\underline{E^f_{t,\alpha/2}} - E_{t,min}\right) < \left(E_{t,max} - \overline{E^f_{t,\alpha/2}}\right) \text{ at } A=0 \\
\text{Fig. 1c } \left(\underline{T^f_{a,\alpha/2}} - T_{a,min}\right) > \left(T_{a,max} - \overline{T^f_{a,\alpha/2}}\right) \text{ at } A=0 \\
\text{Fig. 1d } \left(\underline{K^f_{a,\alpha/2}} - K_{a,min}\right) < \left(K_{a,max} - \overline{K^f_{a,\alpha/2}}\right) \text{ at } A=0 \\
\text{Fig. 1e } \left(\underline{\eta^f_{b,\alpha/2}} - \eta_{b,min}\right) < \left(\eta_{b,max} - \overline{\eta^f_{b,\alpha/2}}\right) \text{ at } A=0 \\
\text{Fig. 1f } \left(\underline{\Delta S^f_{\alpha/2}} - \Delta S_{min}\right) = \left(\Delta S_{max} - \overline{\Delta S^f_{\alpha/2}}\right) \text{ at } A=0
\end{array}\right\} \quad (2)$$

Parities (2) confirm essential dependence of the sizes fiducially interval from frontier intervals (named by us prigrin) even at a "mechanical" estimation of critical values fiducially interval with a significance value $\alpha/2$. In fig. 2, histograms of distribution normalize values of possible realizations considered TEP are resulted.

Elimination "rough" erroneous and of some not typical realizations TEP, has led to elimination of dissymmetric distributions. Full elimination of not typical realizations leads to practically uniform distribution TEP inside fiducially interval.

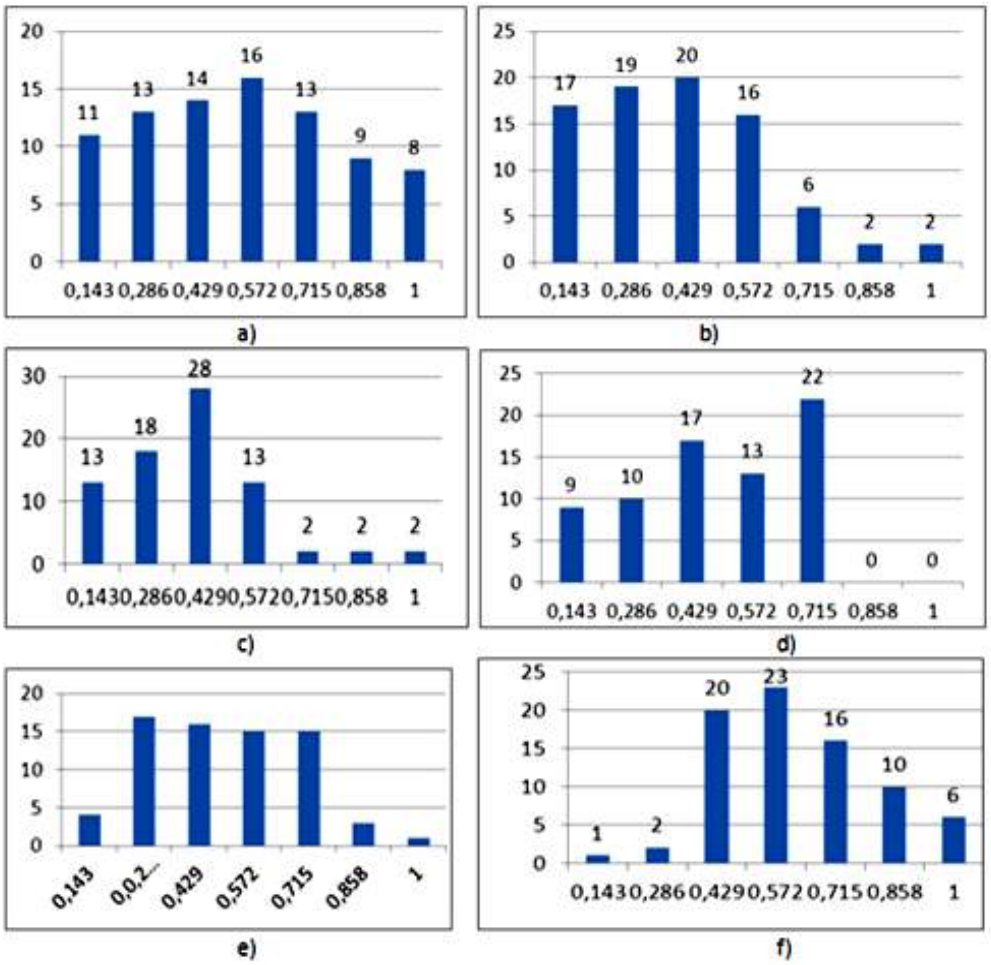

Fig. 2. Histograms of distribution of possible realizations normalize TEP for: a - T_{lg}; b - E_t; c - K_a; d - η_b; e - T_a; f - ΔS.

3. ANALYSIS OF FRONTIER INTERVALS (PRIGRIN)

In table 1, codes of the power units are resulted, allowing estimate mid-annual parameters of a technical condition of power units. First two figures of codes designate a serial number of month, and the third figure - a serial number of the power unit.

Codes of power units correspond to relative deviations TEP placed in ascending order. Thus, the codes presented by table 1 allocate power units, TEP, which have the greatest $\varepsilon(P_i)$.

Table 1

Codes of realizations TEP right prigruns

N n/n	$F^*[\varepsilon(P_{i.j})]$	$\varepsilon(T_{lg.j})$	$\varepsilon(E_{t.j})$	$\varepsilon(\eta_{b.j})$	$\varepsilon(T_{a.j})$	$\varepsilon(K_{a.j})$	$\varepsilon(\Delta S_j)$
1	0,89	0,92	0,16	0,15	0,32	118	0,46
2	0,91	0,62	0,32	0,42	0,41	128	0,21
3	0,92	0,35	0,54	126	0,91	0,96	0,62
4	0,93	0,25	0,26	0,37	114	106	0,35
5	0,94	0,65	114	0,16	121	114	0,42
6	0,96	0,72	0,67	0,22	0,72	0,42	106
7	0,97	0,75	124	124	117	0,45	0,74
8	0,98	0,45	0,45	124	124	0,55	0,76
9	0,99	115	126	0,36	0,16	0,46	0,12
10	1	125	0,94	0,31	126	0,48	0,86

The primary analysis of data of this table shows:

– most often from the general number of the presented data the overestimated values ε (P_i) were observed on the average for the sixth (25%), the fifth (20 %) and the second (18 %) power units;

– for the period November- April it was observed almost in 2,5 times more than the overestimated values of relative deviations TEP, than in second half of year (May- October) months. In many respects defined by character of change of loading of power stations;

– simultaneous discrepancy of realizations of two and more TEP the power unit to shown requirements met only twice, that with probability it is not less than 0,999 confirms actual independence considered TEP;

– at the sixth power unit relative deviation TEP was overestimated for suction air (ΔS) - 31%, the charge of thermal energy on own needs (E_t) - 25% and temperatures of air after RWH (T_a) - 19%. The fifth power unit most «a weak part» had a temperature of leaving gases (T_{lg}) - 58%, and for the second power unit all considered TEP in regular intervals differed the discrepancy to shown requirements.

4. CONCLUSION

1. It is necessary to consider as the major problem of power system engineering of maintenance service and repair of the capital equipment which service life is approximately equal or exceeds normative;

2. For the new equipment reliability and safety of work guaranteed by a manufacturer during normative service life under condition of performance of factory instructions, Rules of technical operation and safety of service. The control of reliability and safety thus is important for revealing a level of operation. At the long operation of the capital equipment equal or exceeding normative service life, the account of reliability and safety from desirable transformed in obligatory. Consequences from refusals can be so significant, that become inadmissible.

3. Analysis fiducially distributions of possible realizations TEP has allowed to establish following general laws:

- fiducially distributions TEP are asymmetric;
- essential dependence of width fiducially interval from a significance value of its boundary values is observed. Even at α =0,05 sizes fiducially interval decrease in some times;
- elimination "rough" erroneous and of some not typical realizations TEP leads to elimination of asymmetry of distributions TEP and transition for of some TEP to practically uniform distribution;
- independence TEP causes absence of simultaneous discrepancy of realizations of several TEP to shown requirements;
- assumption of an admissibility of equality of significance values of boundary values fiducially interval wrongly. The risks of the erroneous decision show in decrease in accuracy and reliability of calculation fiducially interval.

[1] *A.F. Dyakov.* The bulletin of the Russian Academy of Science, 2012, № 3, p.214-224.

[2] *N.I. Voropai, G.V. Kovalev,* etc. The concept of maintenance of reliability in electric power industry. Open Company ID «Energy», 2013, p.304.

[3] *A.I. Orlov.* Polythematic network electronic scientific magazine of Kuban SAU, 2013, 90 (06).

[4] *I.V. Pavlov.* About fiducially the approach at construction of confidential borders for functions of many unknown parameters. The report SA the USSR, 1981, v. 258, p.1314-1317.

[5] *E.M. Farhadzadeh, A.Z. Muradalyiev, T.K. Rafiyeva, A.A. Rustamova.* Maintenance of a faultlessness of data at the automated analysis of technical and economic parameters of boiler installations of power units. M.: Power system № 9, 2019.

[6] *E.M. Farhadzadeh, A.Z. Muradalyiev, T.K. Rafiyeva, A.A. Rustamova.* Maintenance of reliability of methodical support of a management of objects EPS. M., Electricity, №10, 2019.

Received: 25.09.2019

MILLIMETER VIBRATIONAL – ROTATIONAL TRANSITIONS OF GOSH-CONFORMER OF ISOPROPYL ALCOHOL MOLECULE AT J<50

A.A. ADILOV, Ch.O. QAJAR, S.A. MUSAYEVA, A.S. GASANOVA
G.M. Abdullayev Institute of Physics of Azerbaijan NAS
131, H. Javid ave., Baku, AZ 1143
e-mail: atasultan@mail.ru, Qajar666@mail.ru, sm@stp.az

The search of millimeter rotational and vibrational-rotational transitions of gosh-conformer of isopropyl alcohol molecule up to J≤50 (rotational principal quantum number) is carried out using the spectra of gosh-conformer of isopropyl alcohol molecule earlier identified by authors and their inclusions in inverse spectroscopic task. 51 millimeter rotational and vibrational-rotational transitions in main vibrational state up to J≤50 are identified. The reduced Hamiltonian used in total format, well enough describes the rotational and vibrational-rotational transitions of gosh-conformer of isopropyl alcohol molecule complicated by internal rotation. This work is supported by the Science Development Foundation under the President of the Republic of Azerbaijan. Grant № EİF-BGM-2-BRFTF-1-2012/2013-07/04/1.

Keywords: radiospectrometer, Hamiltonian, internal rotation, millimeter wave spectrum, vibrational-rotational spectrum, tunneling splitting, spectroscopic parameters.
PACS: 33.20.-t

INTRODUCTION

The investigations of rotational spectrum of isopropyl alcohol (trans – conformer) in centimeter range has been began by Imanov, Abdurakhmanov, Yolchiyev [1] and later by Hirota [2]. The works by investigation of rotational and vibrational-rotational transitions of gosh-conformer of isopropyl alcohol molecule have been began by Hirota [3]. The gosh-conformers of isopropyl alcohol molecule in our works [4,7,8,10] are investigated with use of reduced Hamiltonian. In these works the rotational, quartic and sixthtic constants are improved with accuracy and the internal rotation parameters are defined. The millimeter spectrum of isopropyl alcohol is recorded on hybrid spectrometer and the catalog more than 7000 spectral lines is written. The accuracy of measurement of spectral line frequencies is in the limit 0,05-0,15 MHz and depends on intensity and inter-disposition of spectral lines. The spectroscopically pure sample of isopropyl alcohol by OP-2 OCCh 11-5 type (99,4% of the main product) is used without further purification. Quade - Lin Hamiltonian is reduced for more detailed study of rotational and vibrational-rotational spectrum and more correct definition of parameters of gosh-conformer internal rotation of isopropyl alcohol molecule in [10]. 340 transitions are identified using this Hamiltonian. However, in this work all parameters of internal rotation and sixthtic constants of centrifugal perturbation we can't define because of the lack of experiment material.

CALCULATION

The task of the continuation of identification with high J of rotational and vibrational-rotational spectra of gosh-conformer of isopropyl alcohol molecule is investigated in the present work. Hamiltonian in matrix form used in the present work, has the following form:

$$H = \begin{vmatrix} \langle s|H|s\rangle & \langle s|H|a\rangle \\ \langle a|H|s\rangle & \langle a|H|a\rangle \end{vmatrix} \tag{1}$$

where

$$\langle s|H|s\rangle = A_s J_x^2 + B_s J_y^2 + C_s J_s^2 - \Delta_j^s J^4 - \Delta_{jk}^s J^2 J_z^2 - \Delta_k^s J_z^4 - 0.5(\delta_j^s J^2 + \delta_k^s J_z^2, J_+^2 + J_-^2) +$$
$$+ H_j^s J^6 + H_{jk}^s J^4 J_z^2 + H_{kj}^s J^2 J_z^4 + H_k^s J_z^6 + 0.5(h_J^s J^4 + h_{jk}^s J^2 J_z^2 + h_k^s J_z^4, J_+^2 + J_-^2)$$
$$\langle a|H|a\rangle = \Delta + A_a J_x^2 + B_a J_y^2 + C_a J_z^2 - \Delta_j^a J^4 - \Delta_{jk}^a J^2 J_z^2 - \Delta_k^a J_z^4 - 0.5(\delta_j^a J^2 + \delta_k^a J_z^2, J_+^2 + J_-^2) +$$
$$+ H_j^a J^6 + H_{jk}^a J^4 J_z^2 + H_{kj}^a J^2 J_z^4 + H_k^a J_z^6 + 0.5(h_j^a J^4 + h_{jk}^a J^2 J_z^2 + h_k^a J_z^4, J_+^2 + J_-^2)$$
$$\langle s|H|a\rangle = 0.5 R_{yx}^{sa}\{J_y, J_x\}_+ + 0.5 R_{zx}^{sa}\{J_z, J_x\}_+ + i P_{yJ}^{sa} J^2 J_y + i P_{zJ}^{sa} J^2 J_z + i 0.5 P_{yx}^{sa}\left\{J_y, J_x^2\right\}_+$$
$$+ i 0.5 P_{zx}^{sa}\left\{J_z, J_x^2\right\}_+$$
$$\langle a|H|s\rangle = \langle s|H^*|a\rangle \ , \ R_{\alpha x}^{as} = -R_{\alpha x}^{sa}, P_{\alpha j}^{as} = -P_{\alpha j}^{sa}, P_{\alpha x}^{as} = -P_{\alpha x}^{sa} \ , \text{where: } \alpha = z, y$$

131, H. Javid ave. , AZ-1143, Baku
ANAS, G.M. Abdullayev Institute of Physics
E-mail: jophphysics@gmail.com

$A_s, B_s, C_s, A_a, B_a, C_a$ are rotational constants correspondingly for symmetrical and antisymmetrical state, $\Delta^s_j, \Delta^s_{jk}, \Delta^s_k, \delta^s_j, \delta^s_k, \Delta^a_j, \Delta^a_{jk}, \Delta^a_k, \delta^a_j, \delta^a_k$ are quartic members of centrifugal perturbation correspondingly for symmetrical and antisymmetrical state $H^s_j, H^s_{jk}, H^s_{kj}, H^s_k, h^s_j, h^s_{jk}, h^s_k, H^a_j, H^a_{jk}, H^a_{kj}, H^a_k, h^a_j, h^a_{jk}, h^a_k$ are sixthtic members of centrifugal perturbation correspondingly for symmetrical and antisymmetrical state, $\Delta, R^{sa}_{yx}, R^{sa}_{zx}, P^{sa}_{yj}, P^{sa}_{zj}, P^{sa}_{yx}, P^{sa}_{zx}$ are parameters obtained in the result of interaction of two states (symmetrical and antisymmetrical ones), i.e. by other words the internal rotation parameters.

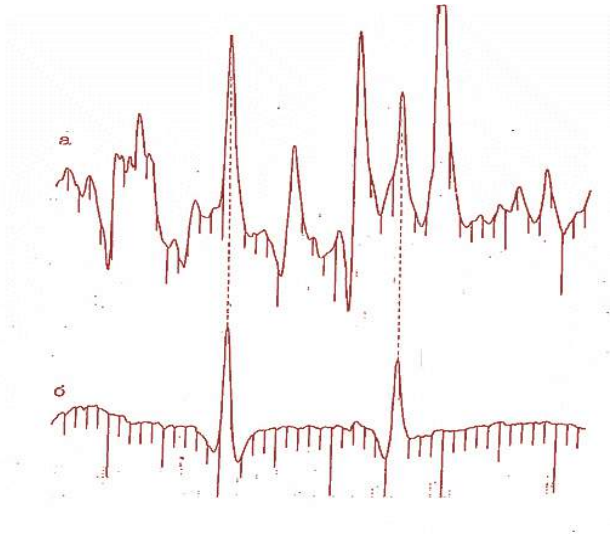

Fig. 1. The record of isopropyl alcohol molecule with Stark modulation (a) and modulation by RF -MW double resonances (b) at pumping $a12_{-1} - a12_{-2}$ 7.586 MHz, probing transitions $a12_0 - a12_{-2}$ 43580.759 MHz and $a12_1 - a12_{-1}$ 43614.287 MHz.

Table 1

The millimeter rotational transitions of isopropanol molecule (gosh-form)

Transitions	Experimental frequencies (MHz)	$N_{ex.} - \nu_{th}$ (MHz)	Transitions	Experimental frequencies (MHz)	$N_{ex.} - \nu_{th}$ (MHz)
J τ - J τ			J τ - J τ		
1	2	3	1	2	3
a 13 7 - a 13 4	42582.600	0.3270	s 37 9 - a 37 8	70319.610	70319.610
a 13 4 - a 13 2	39246.290	0.0093	a 38 38 - s 38 37	48093.760	48093.760
a 14 11 - a 14 9	33927.910	-0.3944	s 38 14 - a 38 13	56222.980	56222.980
a 14 14 - s 14 13	49068.870	0.3848	s 38 8 - a 38 7	77843.080	77843.080
s 15 5 - s 15 2	76019.900	-0.3373	s 37 33 - s 38 33	61782.500	61782.500
a 15 6 - a 15 4	39365.218	-0.2971	a 39 39 - s 39 38	48523.790	-0.1832
a 16 7 - a 16 5	40175.580	0.0080	a 39 32 - s 39 33	39889.330	-0.3088
a 16 6 - a 16 4	33306.820	0.2464	s 39 15 - a 39 14	56347.150	-0.2687
a 17 12 - a 17 10	38787.410	-0.3613	s 39 11 - a 39 10	71443.890	-0.0096
a 18 18 - a 18 15	42695.040	0.2290	s 39 18 - s 39 17	50303.060	-0.0686
s 18 8 - s 18 6	34136.650	-0.2608	a 40 40 - s 40 39	49000.480	0.2199
s 23 10 - s 23 8	51080.970	0.1346	a 40 33 - s 40 34	40097.640	0.1361
s 25 11 - a 25 10	47216.680	-0.3317	a 41 38 - s 41 39	69013.090	-0.0528
s 26 13 - s 26 11	47840.700	0.0572	s 41 13 - a 41 12	72387.160	0.0994
s 27 1 - a 27 0	57154.070	0.1360	a 42 35 - s 42 36	40612.280	-0.2570
a 27 12 - a 27 10	53221.120	-0.2651	a 42 19 - a 42 18	69923.840	-0.2982
s 27 2 - a 27 -1	57154.070	0.1328	a 43 43 - s 43 42	50752.130	-0.2008
s 28 26 - s 28 24	45142.950	0.0405	s 43 17 - a 43 16	64953.530	0.3053
s 30 13 - s 30 11	62196.240	0.3642	s 43 15 - a 43 14	73060.020	0.1277
s 32 27 - s 32 25	64516.870	0.3885	s 44 20 - a 44 19	76780.910	0.1036
a 33 29 - a 33 26	41672.700	0.0403	s 44 32 - a 43 33	76834.760	0.0138
a 33 17 - a 33 14	64180.390	0.2463	a 45 38 - s 45 39	41686.610	0.0907
a 35 17 - s 35 16	53131.420	-0.3419	a 47 47 - s 47 46	54045.310	-0.0571
s 36 34 - a 36 33	46967.540	0.2280	a 48 41 - s 48 42	43212.040	0.1084
a 37 30 - s 37 31	39556.270	-0.2362	a 48 33 - s 47 34	69768.440	-0.0657
s 37 11 - a 37 10	63299.790	-0.0874			

Here $\tau = K_{-1} - K_1$ where K_{-1}, K_1 are projections of total angular moments on molecular axis for states of symmetric tops (extended and thinned symmetric tops).

CONCLUSION

51 millimeter rotational and vibrational-rotational transitions of gosh-conformer of isopropyl alcohol molecule up to J≤50 are identified.

All earlier identified rotational and vibrational-rotational transitions of gosh-conformer of isopropyl alcohol molecule up to J≤50 in frequency range 25 – 78 GHz and 240-496GHz are included in the solution of inverse problem.

[1] *A.A. Abdurakhmanov, M.N. Yolchiyev, L.M.Imanov*. Transactions of AN of Az. SSR, PhTMS series, 1969, №4, pp. 30-35.

[2] *S. Kondo, E. Hirota.* J. Mol. Spectrosc, 1970, v. 34, № l, pp. 97-107.

[3] *E. Hirota.* J.Chem. Phys., 1979, v. 83, № 11, pp. 1457-1465.

[4] *O.N. Ulenikov, A.B. Malikova, Ch.O. Qajar, S.A. Musaev, A.A. Adilov and M.I. Mehtiev.* J. Mol. Spectrosc, 1991, 144, pp. 262-269.

[5] *S.A. Musayev.* Transactions of AN of Az.SSR, PhTMS series, 2000, v. 2000, №6, pp.155-161.

[6] *M.R. Aliyev*. The forbidden rotational transitions in molecules, UFN, 1976, vol.119, №3, p.557-571.

[7] *A.A. Adilov, J.A. Jafarov, Ch.O. Qajar, S.A.Musayev*. JAS, vol. 75, №5, pp. 659- 665.

[8] *A.A. Adilov, J.A. Jafarov, Ch.O, Qajar, S.B.Kazimova, S.A. Musayev.* The millimeter and submillimeter spectra of gosh-conformer of isopropanol molecule, Institute of Physics of Azerbaijan NAS, Baku, Azerbaijan, 2009.

[9] *S.A. Musayev.* AJP Fizika, vol.7, №2, pp 50-56, 2001.

[10] *A.A. Adilov*. The internal rotation and double quantum resonances, PhD thesis on phys.-math. sciences, 1994, Baku, Inst. of Photoelectronics of Azerbaijan NAS.

[11] *S.A. Musayev*. Hybrid radiospectrometer, internal rotation and centrifugal agitation of high orders in molecules of ethanol and isopropanol, Doctoral thesis on phys.-math. sciences, Baku, Institute of Physics of Azerbaijan NAS, 2002.

[12] *A. Maeda, I.R. Medvedev, F.C. De Lucia, E.Herbst.* The Astrophysical Supplement Series, 166, 2006, pp. 650-658.

[13] *E. Hirota, Y. Kawashima.* J. Mol. Spectrosc., 207, 2001, pp.243-253.

[14] *Ch.O. Qajar, S.A. Musayev, E.Ch. Saidov*. DTE, 4, 1991, pp. 134-137.

[15] *Ch.O. Qajar, S.A. Musayev, E.Ch. Saidov*. DTE, 4, 1992, pp. 129-136.

[16] *Ch.O. Qajar, S.A. Musayev, J.A. Jafarov, I.Z.Movsumov, I.M. Kagramanova*. Preprint 001, 1997, Institute of Photoelectronics of Azerbaijan NAS.

[17] *Ch.O. Qajar, S.A. Musayev, S.B. Kazimova, A.A. Abdullayev, M.E. Aliyev, A.S. Hasanova.* Preprint 002, 2004, Institute of Physics of Azerbaijan NAS.

[18] *Ch.O. Qajar, A.A. Adilov, S.A. Musayev, J.A.Jafarov, A.S. Hasanov*. The forbidden rotational-osillational transitions of gosh-conformer of isopropyl alcohol, AJP Fizika, vol.XX, №4, section: Az, pp.24-26, 2014.

Received: 25.09.2019

ABSORPTION AND LUMINESCENCE IN $Bi_{1-x}Sb_x$ ALLOYS

T.R. MEHDIYEV, Kh.A. GASANOVA
G.M. Abdullayev Institute of Physics of Azerbaijan NAS
131, H. Javid ave., Baku, AZ 1143

The photoluminescence spectra of $Bi_{0.97}Sb_{0.03}$, $Bi_{0.88}Sb_{0.12}$, and $Bi_{0.85}Sb_{0.15}$ alloys are presented at a temperature of 300 K in the range from 250 nm to 650 nm of the spectrum. The analysis of the spectra is carried out by decomposition into Lorentz-Gaussian components. Photoluminescence spectra were studied on LS-55 spectrometer (Perkin-Elmler) with Monck-Gillieson monochromator at room temperature in the wavelength range 300–700 nm at excitation from radiation 150W xenon source: 237 nm (5.23 eV), 285 nm (4.35 eV), 298 nm (4.16eV), 337nm (3.678eV), 377nm (3.288eV), 423nm (2.93eV). The accuracy of setting the wavelength is ± 1.0 nm, the reproducibility of the setting of the wavelength is ± 0.5 nm. The investigations carried out now, show that most crystalline media containing bismuth have inherent broad (50-80 nm) bands (blue (with luminescence lifetime $\tau \approx$ 1-2 μs) and red ($\tau \approx$ 5-12 μs)) luminescence. Even in the case of single crystals with bismuth, wide absorption and luminescence bands were observed, which was associated with the electron-phonon interaction of an optical center that is unusual for rare-earth ions, in which optical electrons are screened from the external field of the ligands.

Keywords: absorption, luminescence, $Bi_{1-x}Sb_x$ alloys.
PACS: 71.20. Nr, 72.20.My, 72.20.Fr, 73.50.Jt

INTRODUCTION

In recent decades, bismuth-antimony alloys have attracted attention, not only as a class of some of the best materials for thermoelectricity and cooling in the cryogenic temperature range, but also by the possibilities of using, for example, to create highly efficient laser information systems. At present, optical amplifiers have already been created in the range of 1420-1460 nm with parameters meeting the conditions for their use in information communication systems, and the maximum power of bismuth laser has reached 20 W at an efficiency of up to 50%. A serious obstacle to the improvement of these systems is the lack of an adequate model of the IR bismuth active center. Note that none of the discussed theoretical models doesn't satisfy to the modern experimental data [1].

Bismuth-antimony solid solutions are also interesting because various groups of electronic levels change their energy depending on the composition of Bi and Sb semimetals. The nature of the overlapping bands leading to semimetal behavior for elementary Bi and Sb is different. The bands dramatically change energy depending on the composition, and at values of *x* from 0.07 to 0.23 a real semiconductor is observed [2]. In narrow-gap semiconductor compositions, the states of the valence and conduction bands can be inverted in energy and, accordingly, surface states change, and the basal plane 111 or 001 has threefold rotation symmetry and topological surface states intersecting the Fermi energy an odd number of times. The Fermi surface for electrons in surface states is rather complicated, however, the composition $Bi_{0.9}Sb_{0.1}$ is almost an ideal material for studying topological surface states.

Studies conducted to date have shown that most crystalline media containing bismuth have inherent broad (50-80 nm) bands (blue (with luminescence lifetime $\tau \approx$ 1-2 μs) and red ($\tau \approx$ 5-12 μs)) luminescence. Even in the case of single crystals with bismuth, wide absorption and luminescence bands were observed, which was associated with the electron-phonon interaction of optical center that is unusual for rare-earth ions, in which optical electrons are screened from the external field of the ligands. The analysis of published works showed that most of them were devoted to the study of bismuth in ordered media, which are known to be convenient media for studying the features and structure of optical centers, of which various hypotheses were proposed.

EXPERIMENTAL PART

The photoluminescence spectra of the $Bi_{0.97}Sb_{0.03}$, $Bi_{0.88}Sb_{0.12}$, and $Bi_{0.85}Sb_{0.15}$ alloys at a temperature of 300 K in the range from 250 nm to 650 nm of the spectrum are shown in fig. 1 and 5. An analysis of the spectra by decomposition into Lorentz-Gaussian components is shown in fig. 2-4 and in table 1. Photoluminescence spectra were studied on LS-55 spectrometer (Perkin-Elmler) with a Monck-Gillieson monochromator at room temperature in the wavelength range 300–700 nm when excited from a 150-watt xenon source: 237 nm (5.23 eV), 285 nm (4.35 eV), 298 nm (4.16eV), 337nm (3.678eV), 377nm (3.288eV), 423nm (2.93eV). The accuracy of setting the wavelength is ±1.0 nm, the reproducibility of the setting of the wavelength is ± 0.5 nm.

Comparison of experimentally obtained photoluminescence spectra for the $Bi_{0.97}Sb_{0.03}$, $Bi_{0.88}Sb_{0.12}$ and c. $Bi_{0.85}Sb_{0.15}$ alloys at the temperature 300 K in the range from 250 nm to 650 nm with theoretical calculations by pseudopotential method, in which the fitting of Bi and Sb pseudopotentials to the experimentally investigated optical absorption spectra [3], is given in table 1.

As indicated, a feature of bismuth-antimony solid solutions is the existence of various groups of electronic levels, the energies of which vary depending on the composition of the Bi and Sb semimetals, and a semimetal-semiconductor phase transition is observed at x values from 0.07 to 0.23 [2].

Note that the formation of spectral bands indicating a phase transition to semimetal behavior for

131, H. Javid ave., AZ-1143, Baku
ANAS, G.M.Abdullayev Institute of Physics
E-mail: jophphysics@gmail.com

elementary Bi and Sb, and their compounds are different. As an example, experimental studies of materials containing bismuth showed that blue luminescence (≈400-500nm) arises as a result of the $^3P_1 \rightarrow {}^1S_0$ electronic transition between the energy levels of the Bi^{3+} ion, while the appearance of red luminescence (≈590-640nm) is due to the transition $^2P_{3/2}(1) \rightarrow {}^2P_{1/2}$, bound to the Bi^{2+} ion.

Similarly, the appearance of bright blue luminescence in the spectral region from 470 nm to 515 nm upon excitation of 280 nm in antimony materials was attributed to Sb^{3+} [4]. The Stokes shift of Sb^{3+} in the compound $Ca_{10}(PO_4)_6(F,Cl)$ reaches 19000 cm^{-1}, which is usually observed for other materials at low temperatures [5]. Comparison of the energies of electronic transitions obtained from experimental photoluminescence spectra for the $Bi_{0.97}Sb_{0.03}$, $Bi_{0.88}Sb_{0.12}$ and $Bi_{0.85}Sb_{0.15}$ alloys at a temperature of 300 K in the range from 250 nm to 650 nm (see table 1) and theoretical calculations of the band structure pseudopotential method, in which, in order to establish reliable energy spectra, we used the fitting of Bi and Sb pseudopotentials to experimentally studied optical absorption spectra [3,6], to a first approximation, showed good agreement between them.

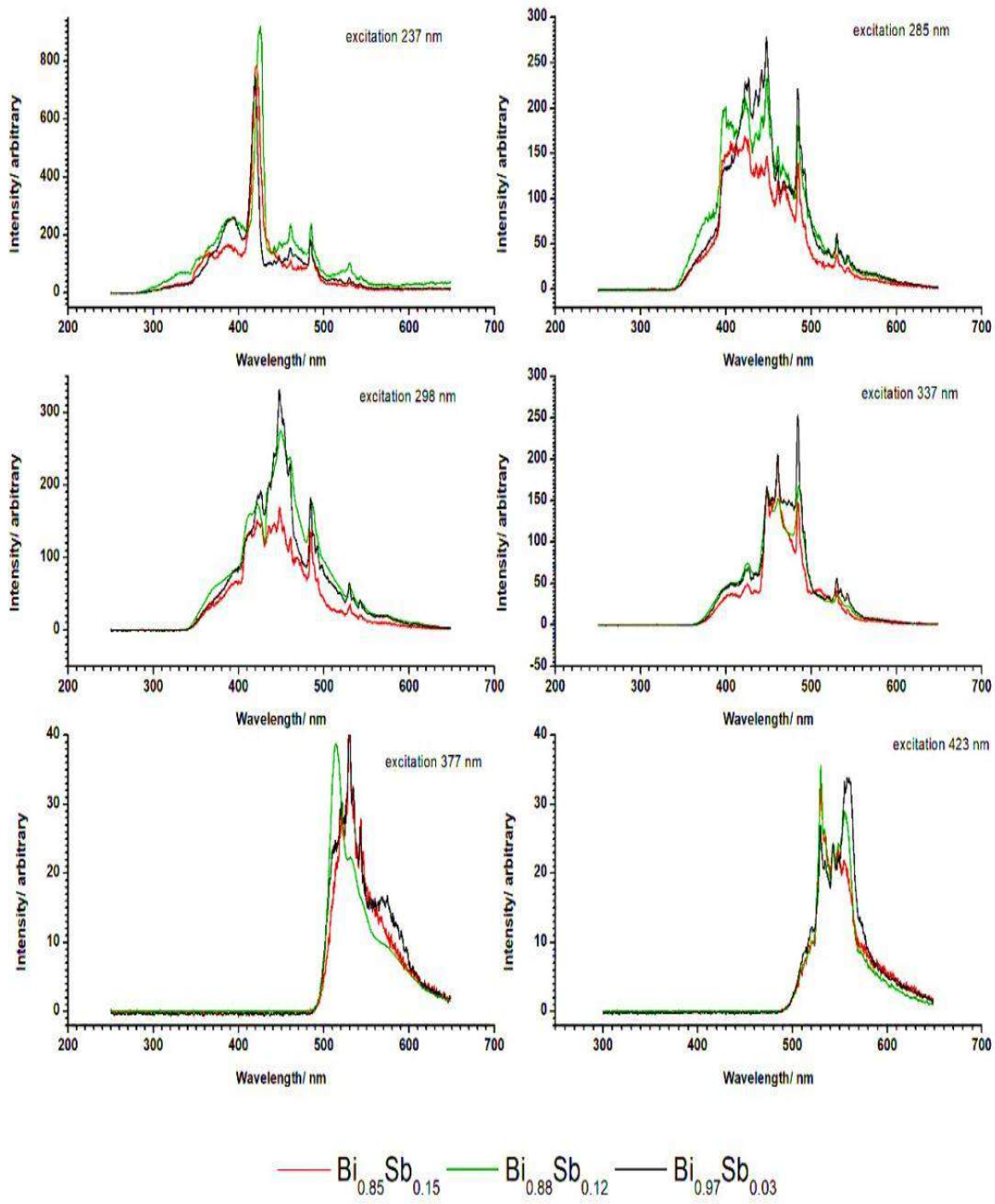

Fig. 1. Luminescence spectra of $Bi_{1-x}Sb_x$ alloys grouped by excitation lines.

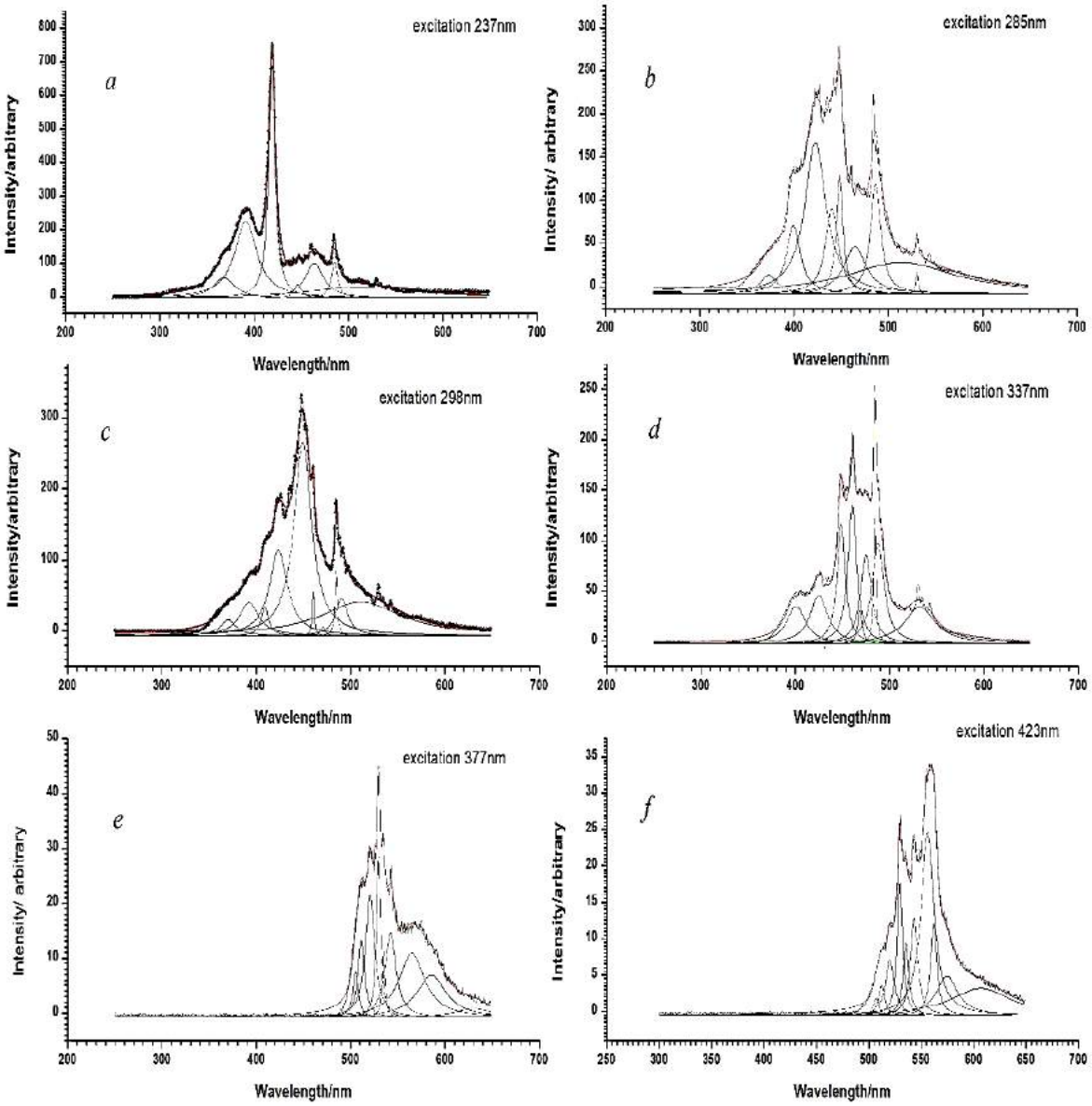

Fig.2. Decomposition of the luminescence spectra of $Bi_{0.97}Sb_{0.03}$ into Lorentz-Gaussian components (indicated in blue). The resulting spectrum is indicated in red.

In table 1, the luminescence maxima corresponding to pseudopotential calculations of the band structures of bismuth and antimony are highlighted in red. However, as one would expect, the photoluminescence spectra of $Bi_{0.97}Sb_{0.03}$, $Bi_{0.88}Sb_{0.12}$ and $Bi_{0.85}Sb_{0.15}$ have a more complex picture of transitions related by luminescence to the "blue" (400-500) nm and "red" (590-640) nm spectral bands, as well as their overlap. The observed pattern of electronic transitions is substantially complicated by the fact that bismuth and antimony are among the heavy p-elements, like Sn, Pb, and Tl, which in some of their compounds (for example, $Bi_{1-x}Sb_x$) have a valence of two units less than the group number. This phenomenon, called the inert pair effect, is structurally observed in distortions of the coordination environment of metal ions. The trivalent Bi^{3+} and Sb^{3+} ions have electronic coordination [Xe] $4f^{14}5d^{10}6s^2$ и [Kr] $4d^{10}5s^2$, that is, the $6s_2$ pair becomes "stereo chemically active" due to the fact that it is not on the spherical orbital, it is asymmetrically displaced relative to the center of the ion (similar to what happens when the formation of hybridized *sp* -orbitals). As a result, various types of structure distortion may occur [7]. On the other hand, analysis of the data on the radii of antimony and bismuth ions can easily notice a large difference between them. [8].

ion	0	-1	-2	-3	-4	-5
Sb	0.161	0.114	0.095	0.082	0.075	0.062
Bi	0.182	0.148	0.117	0.102	0.086	0.075

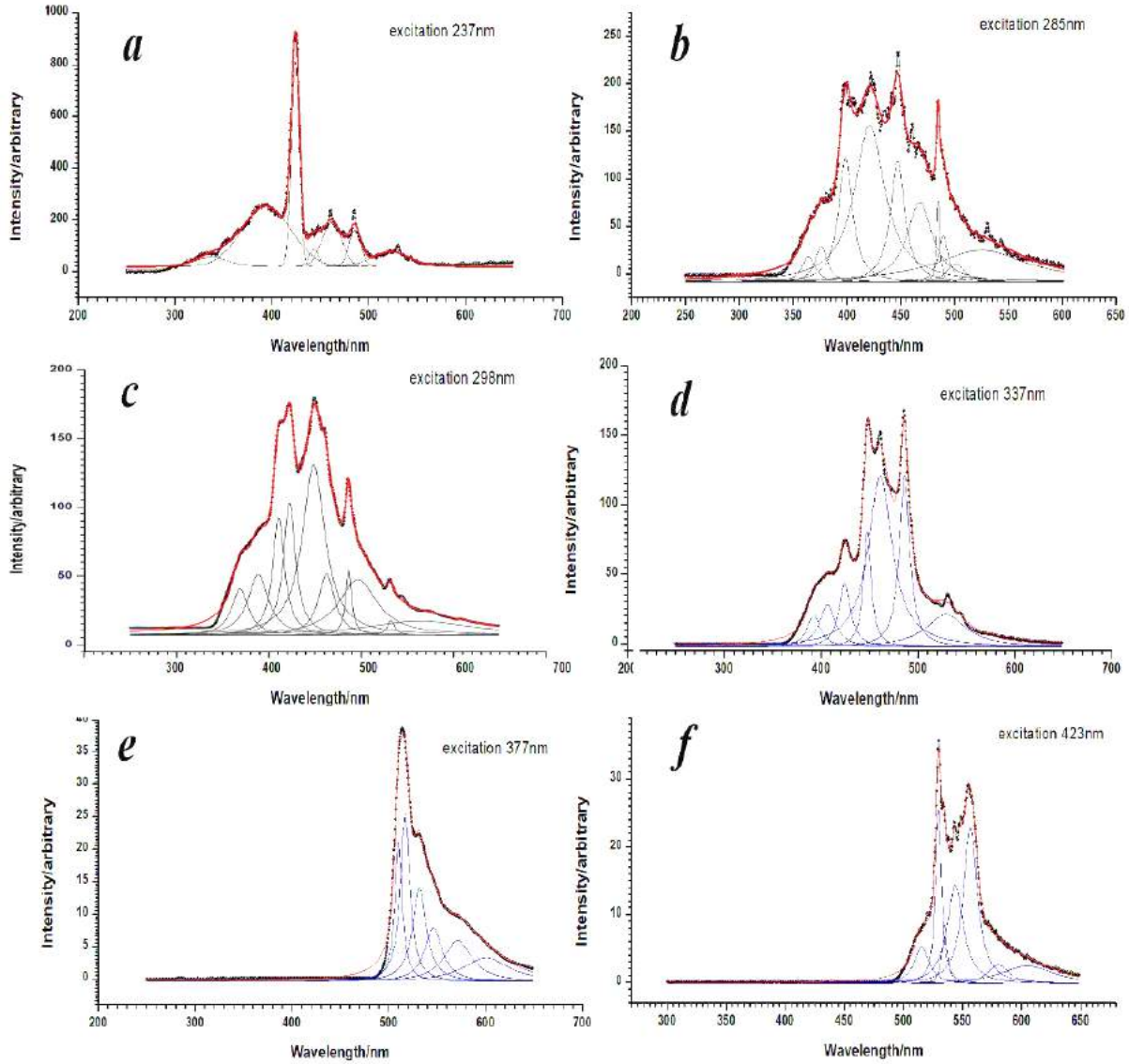

Fig.3. Decomposition of the luminescence spectra of $Bi_{0.88}Sb_{0.12}$ into Lorentz-Gaussian components.

As a result, arising geometric distortions of the structure of $Bi_{1-x}Sb_x$ compositions with respect to pure starting components should lead to a decrease in symmetry, splitting of degenerate states, i.e., to the Jan-Teller effect, or the need to take into account vibronic interactions. Note that a complete classification of possible point groups of crystals subjected to Jahn-Teller strains is given in [9]. To describe the Jahn-Teller (or vibronic) interactions of electrons with nuclei, they often resort to the formalism of potential energy surfaces. In the quadratic approximation, the potential energy surface corresponds to second-order hypersurface E(Q), which is parameterized by the constants F_i and K_i and, in the one - dimensional case it degenerates to the parabolic curves shown schematically in figures (a, b, c) below.

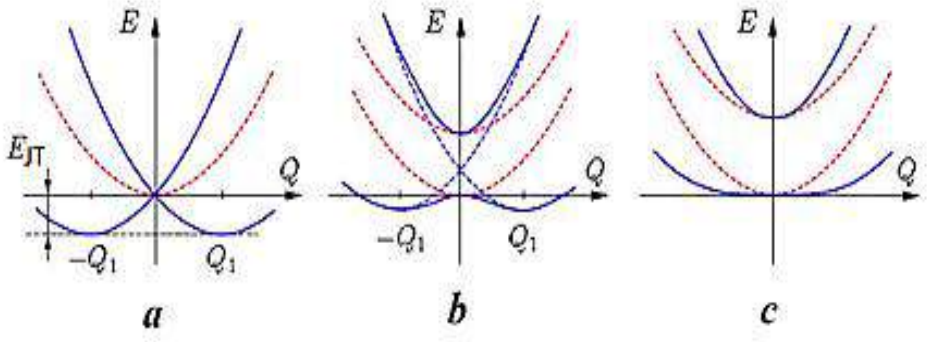

The dashed line in the graph is the initial adiabatic potential for the highly symmetric undeformed nuclear configuration Q=0. Taking the Jahn-Teller effect into account leads to splitting of this curve into two components with minima at the points Q_i=0. In general, the number of intersecting branches of the adiabatic potential is equal to the degree of degeneracy electronic levels *N*. Thus, the minimum at the zero point disappears and new states ±Qi appear, which correspond to low-symmetric deformed system configurations. The statement of system instability in Q=0 is called the simple Jahn-Teller effect. However, phenomena similar to the Jahn-Teller effect can be observed in systems with quasi degeneracy [10,11]. By definition, in the presence of quasi degeneracy, the electronic levels are quite close, but do not coincide, which is depicted as being close to each other by disjoint potential curves (see fig. b, c). Taking into account the Jahn-Teller pseudo-effect leads to the fact that the initial system at the point Q=0 either softens (fig. c) or becomes unstable (fig. b). Note that almost all molecular systems are subject to PEJT, in contrast to the simple effect of JT, which strictly requires degeneration of levels.

Periodically located translation Jahn-Teller centers may be subject to the cooperative effect. With sufficient approximation of neighboring centers, the external molecular field of each ceases to be isotropic. The nonequivalence of the effects leads to the stabilization of one of the possible directions of deformation for each center. In this case, one can observe the structural phase transition from the state of crystal with dynamically disordered Jahn-Teller systems to the state with completely static centers. This type of vibronic interactions is called the cooperative Jan-Teller effect. The mentioned correlation of deformations can be destroyed by strong temperature vibrations of the lattice. The fracture temperature of an ordered system of static centers depends on the strength of Jahn-Teller effect in particular Jahn-Teller crystal. Note that, when this is important, it is important to take into account the environment of the ion, that is, the influence of the asymmetric components of the crystal field of the lattice as the effect of some external potential. Theoretically, this means that the imposition of a small external disturbance can stabilize the system in one of the low-symmetry states. In this case, the static Jan-Teller effect occurs. An external disturbance can also create additional Qi distortions in the already deformed Jahn-Teller system (see the fig. a, b, c). If the forces of the external low-symmetric action are greater than the Jahn-Teller forces, then the Jahn-Teller effect can be completely suppressed. In crystals of anionic complexes, a complete removal of JT distortions can be expected where the Jahn-Teller ion is chemically modified, or there is a strong coordination bond of the ion with other components of the complex. In the case of small perturbations, the so-called vibronic amplification [10,12] can be observed, and the coefficient of vibronic amplifications completely depends on the elastic constants of the molecular framework and the perturbation force (for example, in Cu^2, Mn^3, etc., this coefficient reaches ≈40). In systems with a small external influence, the forces of external perturbations can play a stabilizing role if they make the Jahn-Teller minima on the surface of potential energy nonequivalent and the system is at the deepest minimum. Thus, the redistribution of minima on the surface of potential energy should not be isotropic. On the contrary, a highly symmetric environment is not able to stabilize the deformations of the Jahn-Teller ion. In crystals, such nonequivalent interactions are transmitted through the van der Waals forces, hydrogen bonds, and the cooperative Jahn-Teller effect.

Figure 6 shows the excitation spectra of (a) and luminescence (b) of $Bi_{0.97}Sb_{0.03}$ (semi-metallic state). The maximum of the spectral line 257nm of the excitation spectrum, according to the principle of Levshin's mirror symmetry, corresponds to a maximum of 419nm luminescence, relative to the label 338nm. Inverted specularly relative to the label, the excitation spectrum (indicated in blue) is combined with the luminescence spectrum. If we assume that a maximum of 257nm (4.82eV) corresponds to the $^1S_0 \rightarrow {}^1P_1$ transition in Bi^{3+}, then the $^3P_1 \rightarrow {}^1S_0$, transition, corresponding in this case to the maximum of 419nm (2.96eV) of the luminescence spectrum, should, according to pseudopotential calculations of the bismuth band structure [6], occur on the line of symmetry $L_s \rightarrow L_a$. The observed Stokes shift is 261nm. However, we note that the $^3P_1 \rightarrow {}^1S_0$ transition is observed not only in all $Bi_{1-x}Sb_x$ compositions, but also on the luminescence spectra upon excitations by 298 nm (4.16eV) and 337nm (3.678eV) radiation. The latter turns out to be explainable, since the luminescence spectrum of $Bi_{0.97}Sb_{0.03}$ shows similar but low-intensity structures, which are confirmed upon excitation at 285 nm (4.35eV), 298 nm (4.16eV) and 337 nm (3.678eV) (see fig. 5a). The sequence of their location from each other corresponds to: 190meV between 1-2 spectra; 80 meV between 2-3 spectra (or 270 meV between 1-3 spectra), which are close in value to the vibrational frequencies, and may well indicate the presence of cooperative PEJT, as well as indicated in [13], the Johns-Peierls transition. A similar structure is found in the $Bi_{1-x}Sb_x$ spectra under excitations of 377nm and 423nm (see figs. 1–5), and the luminescence spectra for all the studied compositions are outwardly similar. On the luminescence spectra of $Bi_{1-x}Sb_x$ (fig. 1), it is easy to see how the overlap of the luminescence spectra of Bi and Sb changes.

However, if the presence of “blue” luminescence in Bi1-xSbx was not in doubt, then the presence of a weak “red” is possible only when Bi or Sb are in divalent states. Of course, we can assume the existence of small concentrations of defective or impurity centers of divalent Bi^{2+} and Sb^{2+} ions, especially since, as can be seen from table 1, the corresponding transitions can be selected for this. However, the goal of these studies was only to detect the cooperative effect of PEAT in Bi_{1-x} Sb_x. Oddly enough, in scientific publications information on the luminescence associated with electronic transitions in the ultraviolet and visible spectral ranges of $Bi_{1-x}Sb_x$ alloys is practically absent. Table 1 shows all the electronic transitions experimentally detected in the luminescence spectra.

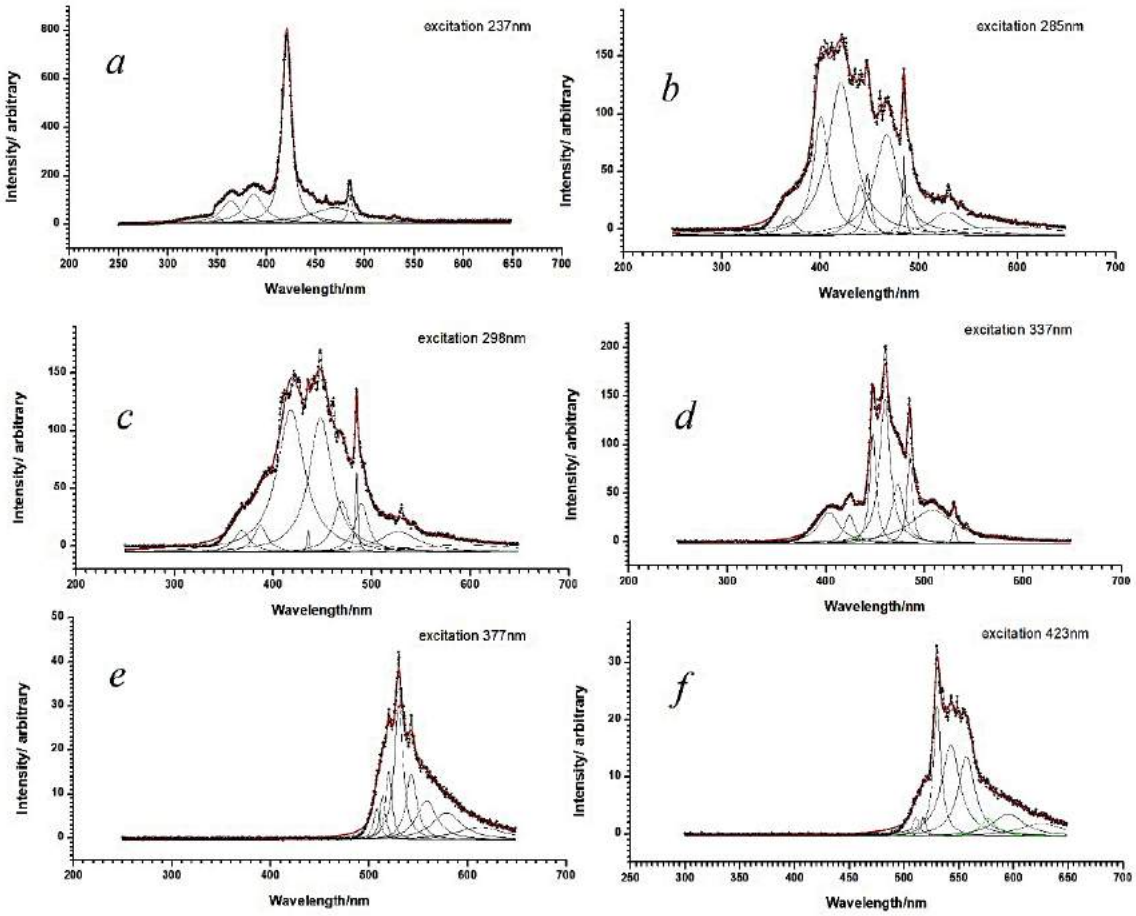

Fig. 4. Decomposition of the luminescence spectra of $Bi_{0.85}Sb_{0.15}$ into Lorentz-Gaussian components.

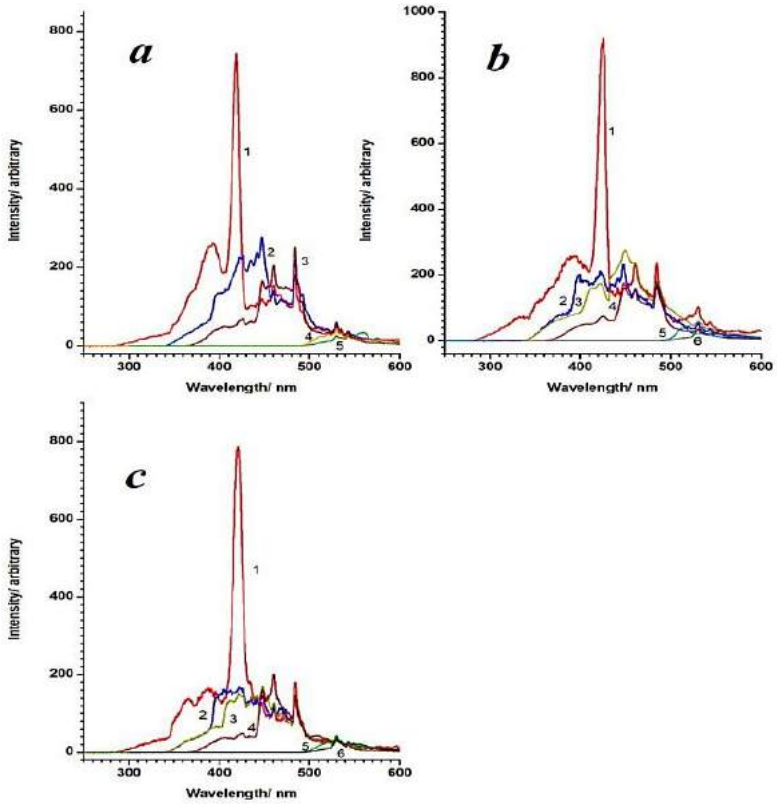

Fig. 5. Luminescence spectra:

a. $Bi_{0.97}Sb_{0.03}$ at excitation from: 1- 237nm, 2- 285nm, 3 - 337nm, 4 - 377nm, 5 - 423nm;[3]

b. $Bi_{0.88}Sb_{0.12}$ and c. $Bi_{0.85}Sb_{0.15}$ at excitation from: 1 -237nm, 2 -285nm, 3 -298nm, 4 337nm, 5 -377nm, 6 - 423nm.

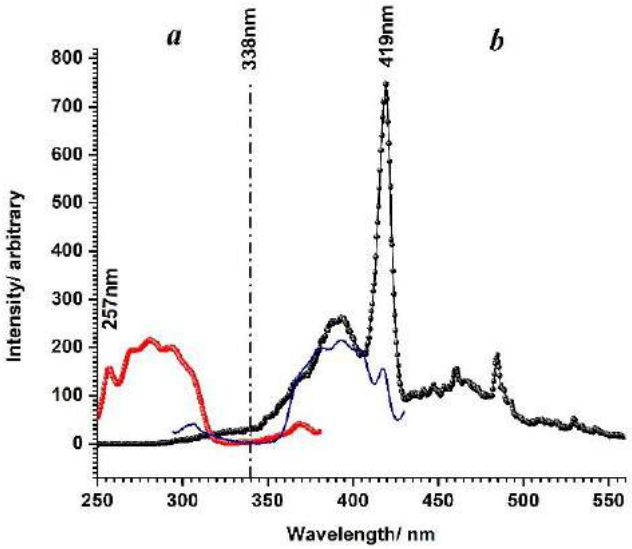

Fig. 6. Excitation spectra of (a) and luminescence (b) of $Bi_{0.97}Sb_{0.03}$ (semi-metallic state).

Table

Comparison of electronic transitions detected in the luminescence spectra of $Bi_{0.97}Sb_{0.03}$, $Bi_{0.88}Sb_{0.12}$ and $Bi_{0.85}Sb_{0.15}$ alloys at a temperature of 300 K in the range from 250 nm to 650 nm with theoretical calculations by the pseudopotential method [3].

Accounting		**$Bi_{0.85}Sb_{0.15}$**	**$Bi_{0.88}Sb_{0.12}$**	**$Bi_{0.97}Sb_{0.03}$**
[2]	**[3]**	624,6		
		603,7	606,2	
		587,7	597,2	
		571,9	571,7	573,2
		565,4		568,2
		553,7		558,2
		549		549,0
		543,3	543,9	542,7
		534,8		534,6
		530,2	530,8	530
		519,6	519,8	520,3
		512,6	513,5	513,6
498,6	496,6	503	502,3	
492,7		491,6	491,9	491,9
		484,7	485,3	485,4
		469,1	466,8	467,6
		460,9	460,9	460,9
		446,6	448,4	447,8
		439,4	442,2	435,8
		428,9	425,5	426
420,6		421,4	423,3	419,3
	417,8	410,6	408,5	409,3
		397,2	395,5	396
387,7	371,4	382,2	377,5	384,9
362,7	362,7	364,4	366,4	372,7
343,5	346,4	349,6	353,5	350,0
			334,5	332,6

[1] *I.A. Bufetov and E.M. Dianov.* Biopedoped fiber Lasers, Laser Physics Letters, vol. 6, issue 7, p.487-504, 2009.

[2] *B. Lenoir, M. Cassart, J. P. Michenaud, H.Scherrer* and *S. Scherrer.* J. Phys. Chem. Solids, 1996, 57, 89.

[3] *S. Gölin.* Band structure of bismuth: Pseudopotential approach, Phys. Rev.,166, 643, 1968.

[4] *G. Blasse.* Luminescence of Calcium Halophosphate -Sb^{3+}, Mn^{2+} at Low Temperatures. 1983, Chemical Physics Letters, vol. 104, pp.160-162.

[5] *D.L. Dexter, C.C. Klick* and *G.A. Russell.* Criterion for the Occurrence of Luminescence. 1955, Physical Reviews, vol. 100, pp. 603-605

[6] *P.Y. Wang, A.L. Jain.* Modulated piezo reflectance in bismuth, Phys. Rev., B2, 2978, 1970.

[7] *A. West.* Chemistry of solids. Theory and applications. Moscow, "Mir", 1988.

[8] *L.T. Butenko., S.M. Ryabikh, A.K. Bugayenko.* Vestnik MSU, Chemistry series, vol. 49, №6, 2008 (in Russian).

[9] *P. Pelikán* and *M. Breza*. Classification of the possible symmetries of the Jahn-Teller systems, Chem. Papers 39 (2) 255-270,1985.

[10] *I. Bersuker.* Yahn- Teller effect and vibronic interactions in modern chemistry, Moscow: Science, 1987.

[11] *U. Opik.* Studies of the Jahn-Teller Effect. I. A Survey of the Static Problem, Proceedings of the Royal Society A: Mathematical, Physical and Engineering Sciences, 1957, vol. 238, № 1215, p. 425–447.

[12] *I. Bersuker.* The Jahn–Teller Effect, Cambridge University Press, 2006, p. 632.

[13] *A.B. Shick, J.B. Ketterson, D.L. Novikov, A.J. Freeman.* Phys. Rev. B, vol.60, №23, 1999, p. 15 484-15 487.

Received: 03.10.2019

EPR INVESTIGATIONS OF γ-IRRADIATED POLYTETRAFLUOROETHYLENE/CdS NANOCOMPOSITES

E.G. HAJIEVA
Institute of Radiation Problems of ANAS
9, B. Vahabzadeh str., Baku
email: egana@yandex.ru

It is shown that g-factor values for PTFE/CdS nanocomposites at dose 5kQr corresponds to free electrons. The nonlinear dependence of signal intensity on craze number is observed with increase of craze cycle in EPR spectra.

Keywords: γ – irradiation, nanocomposites, polytetrafluoroethylene, magnetic field, EPR-spectra, dielectric properties, dielectric loss, dielectric constant, crazing, g-factor.
PACS: 71.20 Nr; 72.20 Fr

INTRODUCTION

Nowadays the significant number of works dedicated to modification of surface and structure of polytetrafluotoethylene (PTFE) are carried out. PTFE films are some of the best dielectrics, its dielectric properties weakly depend on field frequency at wide temperature intervals [1,2]. Moreover, the value of dielectric loss tangent of angle (tg δ) and dielectric constant (ε') significantly increase at influence by *γ*-irradiations and/or by accelerated electrons [3]. It is shown that the increase of tg *δ* at *γ*-irradiation is connected with formation of peroxide macro-radicals of tail and medial types as a result of destruction and oxidation processes [3,5].

The study of regularity of formation and stabilization of primary paramagnetic centers (free radicals, electrons) induced by electric and /or magnetic fields promotes to development of new approach at study of primary processes in *γ* -irradiated nanocomposites. With the aim of their oriented modification, EPR method is the unique one for the study of the change of radical g-factor, local fields, their surrounding (note that *g* -factor is the ratio of mechanical moment to magnetic one which is equal to 2,0023) and for the evaluation the spin density, their anisotropy and structural changes in polymers [14 - 16].

The technological questions of modification of PTFE are the one of important ones for improvement of polymer exploitation characteristics. Moreover, the radiation technology plays the important role. The radiation resistance (in 100 – 200 times) and the physic-mechanical properties of PTFE are improved [17 – 19]. In work [20] it is shown that at electron irradiation the films from matched PTFE with thermostability 450 -500^{0}C are obtained with beam density by 10^2-10^3 μA/cm^2.

The investigation of influence of γ-irradiations and uniaxial orientation of crystallized polymers, in particular, PTFE, polyethylene terephthalate (PETF) and etc. are important for development of new "track" membranes with pores on the surface with diameter by 20-500nm order. The formation of nano compositions on the base of craze PTFE, PETF and luminescent fillers CdS, ZnS is the one of actual tasks at obtaining of flexible luminescent compositions. It is important to note that detail study of polymer craze processes allows us to vary the porosity and significantly increase the quantity of introduced additives in the polymer.

EXPERIMENTAL PART

The oriented nanocomposites PTFE/CdSZnS are obtained by "craze" method, i.e. by the way of uniaxial orientation of PTFE films in the adsorption-active medium from 30% isopropanol solution in water [7,13]. The binary mixture CdS/ZnS at ratio 90:10 vol.% (the value of forbidden band width E_g=2,42eV for CdS, and E_g=4,27 eV for ZnS [12]) is used with the aim of extension of luminescence composition sensitive region. Note that the crazing is the polymer modification universal method, their structure and properties at introduction of low-molecular additives in polymers, in particular, in cases where additives aren't compatible with polymers.

EPR investigations are carried out on spectrometer EMX Plus (Bruker). The magnetic field intensity 600mmT and modulation frequency 10^5Hz, interval of amplitude modulation interval is 0÷2mT.

The samples are put into glass tube with diameter 3mm and measurements are carried out at T=300K. The resonance frequency is 9,75 GHz.

g-factor is defined from equation $E=h\nu=g\mu_B \cdot B_0$.

$g=\frac{h\nu}{\mu_B \cdot B0}$, where μ_B is Bore magnetron, is the natural value of electron magnetic moment.

The technique of uniaxial polymer orientation in adsorption-active medium and the technique of dielectric parameters (tg δ, ε, ρ_v) are described in [21].

The introduction of fillers in oriented PTFE in the stage of polymer color change is carried out in four cycles.

The sample is carefully washed in distillate water after each cycle of nanoparticle formation in polymer pores [22].

The nanocomposite samples are irradiated by γ-quantums ^{60}Co in source MPX- γ-20M. The dosimetry is carried out by ferrosulfate method.

The study of peculiarities of radical- formation role at *γ*-irradiation of nanocomposites polytetrafluoroethylene/CdS is the aim of the given work.

131, H. Javid ave., AZ-1143, Baku
ANAS, G.M.Abdullayev Institute of Physics
E-mail: jophphysics@gmail.com

EXPERIMENTAL RESULTS AND THEIR DISCUSSION

The irradiation of solid state, in particular polymer composites, should be accompanied but not only by its ionization and by formation of new electron traps-radicals, and by release of already captured electrons from the traps. Note that the blanching process and role of O_2 molecules dissolute in polymers in radical-formation takes the important place [23]. Besides, the influence of constant magnetic field on electron transitions between Zeeman levels [4,14] are the essential tasks in radiation physical chemistry of nanostructured materials.

EPR spectra of PTFE samples/after 3 cycles of CdS introduction under condition ΔH=7,64G and g=2,0028 are shown in fig. 1. *g*-factor values allow us to propose that it connects with electron centers in matrix. From the given spectrum it is seen that at H=3480-3500G the narrow singlet the appearance of which can be connected with free electrons in composite. At the increase of *γ*-irradiation dose up to 5kQr the EPR spectrum narrowing is observed and values of g-factor achieves the maximum, further it decreases with increasing irradiation dose.

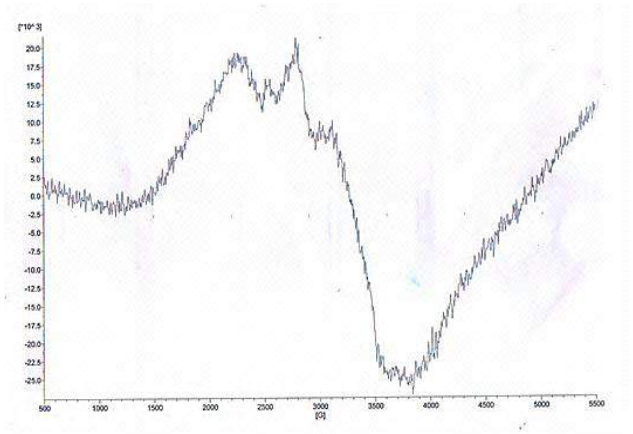

Fig.1. EPR spectrum of PETF/CdS nanocomposite samples crystallized at 3 treatment cycles and *γ*-irradiated up to 3 kQr doses.

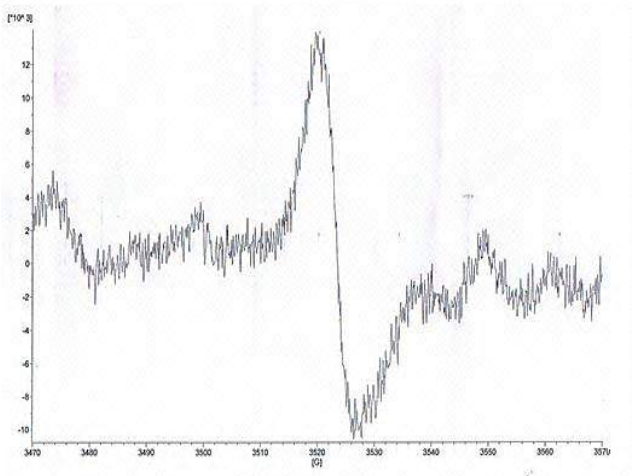

Fig.2. EPR spectrum of PETF/CdS nanocomposite samples crystallized at 3 treatment cycles and *γ*-irradiated up to 5 kQr doses.

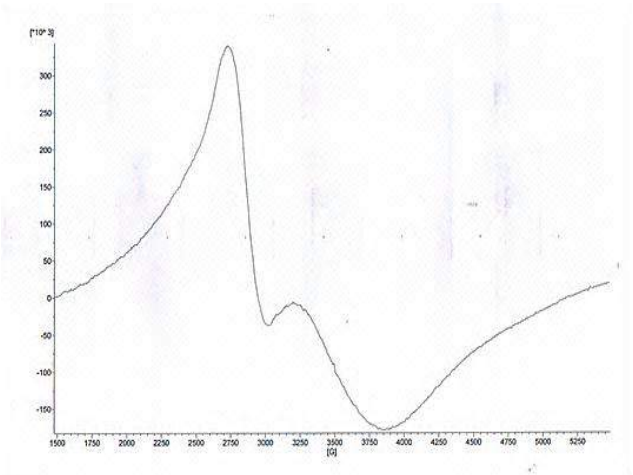

Fig.3. EPR spectrum of PETF/CdS nanocomposite samples *γ*-irradiated up to 5 kQr doses after 3 cycles of CdS implantation.

Table

Oriented samples	Initial ones			After γ-irradiation, 3kQr			After γ-irradiation, 5kQr		
	ΔH, G	g	I,rel. un.	ΔH, G	g	I, rel. un.	ΔH, G	g	I, rel.un.
PTFE	1110	2,160	45,75	103,8	2,149	40,5	-	-	-
PTFE/CdS 3 cycles	1192	2,060	41,25	971,5	2,168	290	669,2	2,0203	169
PTFE/CdS 16 cycles	-	-	-	987,8	2,16	135	958	2,244	129

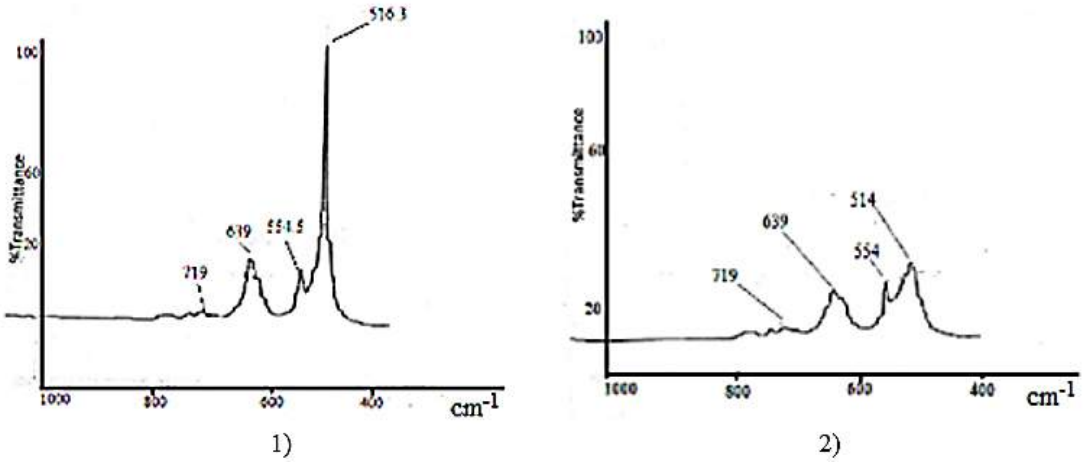

Fig.4. IR-absorption spectra in region 400 – 1000cm^{-1} of PTFE/CdS samples after 6th cycle of nano-CdS implantation.

The another important peculiarity of EPR spectra of PTFE/CdS nanocomposites is that the significant change is observed at increase of craze cycle in EPR spectra, narrow band signal disappears, the wide band signal appears after *γ*-irradiation (fig. 2 and fig. 3). EPR spectrum of PTFE/CdS composite samples irradiated up to doses 5kQr after 3 cycles of CdS implantation is shown in fig. 3.

It is revealed that values of *g*-factor firstly increase, passes through maximum at dose 5kQr and further decrease tendency is observed in the dependence on irradiation dose of PTFE/CdS samples with increasing *γ*-irradiation time. The changes of g-factor values and intensities of EPR signals in the dependence on implantation cycle of CdS nanoparticles and irradiation dose are given in the table.

From the table it is followed that the values of g-factor decrease after *γ*-irradiation by 3-5kQr dose. The ratio of wurtzite and sphalerite components of CdS which are reflected in the changes of g-factor values in the dependence on quantity of "craze" nanoparticles of CdS in PTFE matrix.

IR-spectra of the samples in the dependence on craze cycles are obtained for the study of structural changes in PTFE and nanocomposites on the base of oriented PTFE/CdS in the dependence on adsorbed nanoparticles in polymer. IR-spectra of absorption for the oriented samples PTFE (curve 1) and samples after CdS implantation craze (curve 2) are shown in fig. 4.

From the comparative analysis of these spectra it is seen that the absorption intensity at 516cm^{-1} decreases with increasing cycle number of nano-CdS implantation in oriented PTFE samples and CdS quantity. After three cycles the given peak intensity decreases in 4,5 times. Besides, 639cm^{-1} and 516cm^{-1} peaks widen with increasing implanted CdS nanoparticle number.

[1] *A.D. Pomogailo, A.S. Rozenberg, I.E. Ufland.* The metal nano-particles in polymers. M., Chemistry, 2000.

[2] *A.L. Buchachenko.* Nano-chemistry is the direct way to high technologies. Uspehi himii I 2003, vol.53, № 5, pp.419 – 421

[3] *Z.P. Hedwig.* Radiation chemistry of molecules (E.E.Finkel): Polymer radiation electric conduction, M., Atomizdat, 1978, pp.121-134.

[4] *P. Keyzer, K. Tzui, F. Willams.* The investigation of stabilized elecrons in low-molecular organic glasses and polymers by methods of optical spectroscopy and EPR (E.E. Finkel,), M., Atomizdat, 1978, pp.135-175.

[5] *A.V. Vannikov, V.K. Matveyev, V.P. Sichkar, A.P. Tutnev.* Electric properties: Radiation effects in polymers, M., Science, 1982, p.272.

[6] *A.M. Magerramov, M.K. Dashdamirov.* Chemistry of high energies. 2005, vol.39, №3, pp.176-182.

[7] *A.L. Volinskii, A.E. Mikushev, L.M. Yarisheva, N.F. Bakeyeva.* Russian Chemical Journal (Journal of Russian Chemical Community named after D.M. Mendeleyev), 2005, vol. XLIX, №6, pp.118-128.

[8] *A.M. Magerramov, M.A. Nuriyev.* The influence of *γ*-radiation on charge state of polytetrafluoroethylene/CdS nano-composites, Journal of Radiation Research. ANAS, 2015, v. 2, № 1, p.18-25.

[9] *A.P. Tutnev, V.S. Sayenko, E.D. Pojidayev,*

N.S. Kostyukov. Polymer dielectric properties in the ionizing radiation fields, M., Science, 2005, p.453.

[10] *M.U. Yablokov, V.G. Shevchenko, A.B. Gilman, A.A. Kuznecova,* Chemistry of high energies. 2014, vol. 48, № 4, pp. 326-330.

[11] *M.A. Nuriyev, A.M. Magerramov, A.A. Shukurova.* Influence of gamma irradiation on charge state of nanocomposites PTFE/CdS. VII Euroasian Conf. "Nuclear Sci. and ITS Appl." Baku, 2014, pp.244-245.

[12] *M.K. Kerimov, A.M. Magerramov, E.G. Hajieva.* Electrothermo-luminescence of polymer compositions. 8th International Symposium "Polymer for Advanced Technology", 2005, Budapest, p.50.

[13] *A.M. Magerramov, M.A. Nuriyev, E.G. Gadjiyeva.* Electron treatment of materials: The influence of γ-radiation on polypropylene/CdS composite photothermoluminescence, 2017, 53(5), pp. 21-25.

[14] *A.L. Buchachenko.* Spectroscopic methods of polymer investigations: The polymer investigation by the method of electron paramagnetic resonance, M., "Znanye", 1975, p.82.

[15] *V.K. Mlinchuk, E.R. Klinshont, S.Y. Pshejeckii.* Macroradicals, M., Chemistry, 1980, p.264.

[16] *V.Y. Kabanov, V.I. Feldman.* Chemistry of high polymers. 2009, vol. 43, № 1, pp. 5-21.

[17] *M.A. Bruk.* Chemistry of high energies. 2006, vol.40, № 6, p.403.

[18] *V.S. Sayenko, V.I. Feldman, A.P. Tutnev*. Chemistry of high energies. 2011, vol.45, № 1, pp.51-54.

[19] *A. Oshima, S. Ikeda, E. Katoh, Y. Tabata.* Radiation physics and chemistry, 2001, v. 62, № 1, pp.39-45.

[20] *M.A. Bruk, A.V. Spirin et.al.* II International Conf. "Micro- and nanoelectronics-2005", Moscow-Zvenigorod, abstracts, 2005, p.1.

[21] *A.M. Magerramov, M.A. Nuriyev, A.A. Shukurova, E.A. Allahyarov.* Nanocomposites on the base of nonoaxial oriented polymers, Materials of Ist International Scientific Conference "Nano-technologies and its applications in technique", Baku, APU, 2010, pp. 98-101.

[22] *E.I. Kapinus.* Journal of "Physical Chemistry", 2011, vol. 85, № 4, pp. 748-752.

[23] *I.V. Kuleshov.* Polymer radiothermoluminescence, M., Chemistry, 1991, p. 128.

Received: 17.10.2019

OBTAINING WHITE LIGHT BY THE COMBINATION OF $Gd_3Al_5O_{12}:Ce^{3+}$ AND $Y_3Al_5O_{12}:Ce^{3+}$ PHOSPHORS IN LIGHT EMITTING DIODES

T.Y. ORUJOV[1,2]
[1]*G.M. Abdullayev Institute of Physics,*
131, H. Javid ave., NAS, Baku, Azerbaijan
[2]*Research and Development Center for High Technologies,*
Ministry of Communications and İnformation Technologies

This paper reports on the use of $Gd_3Al_5O_{12}:Ce^{3+}$ phosphor mixed with $Y_3Al_5O_{12}:Ce^{3+}$ phosphor for the manufacturing of white light emitting diodes as a way of increasing their optical performance as opposed to purely $Y_3Al_5O_{12}:Ce^{3+}$ based LEDs. Such optical parameters as luminous flux, correlated color temperature, color rendering index and purity of white light of WLEDs with the addition of $Gd_3Al_5O_{12}:Ce^{3+}$ phosphor are being studied.

Keywords: light emitting diodes, luminescence, LED phosphors.
PACS: 42.50.Ct, 78.55.−m

1. INTRODUCTION

Currently, most commercially available white LEDs are generated by combining a blue LED with a yellow phosphor $Y_3Al_5O_{12}:Ce^{3+}$ [1,2] (phosphor converted white LEDs), but these LEDs produce "cool" white light with a high color temperature >6000K and color rendering index (R_a) within the 70-80 range. The YAG:Ce phosphor achieves only cold white light due to the fact that the red component is not intense enough for warmer emission tones. And increasing the thickness of the layer makes the radiation excessively yellow. By adding a phosphor with a higher intensity in the red region, it is possible to improve such optical parameters as the correlated color temperature, color rendering index, and luminous flux of the LED emission [3]. Usually the red emitting centers in phosphors are introduced by the $Eu^{2+,}$ Eu^{3+}, Sm^{3+}, Pr^{3+} ions and some traditional metal ions, such as Cr^{3+}, Mn^{4+}, which are suitable for improving the color rendering index and color temperatures. In other cases, by replacing yttrium Y ions in the $Y_3Al_5O_{12}:Ce^{3+}$ structure with smaller or larger ions, the emission spectrum can be adjusted. In particular, the replacement of Y^{3+} in its dodecahedrally coordinated region by a large Gd^{3+} ion leads to a red shift [4]. In this paper we are using the $Gd_3Al_5O_{12}:Ce^{3+}$ phosphor for the manufacture of white light emitting diodes.

2. EXPERIMENTAL SECTION

For this experiment, we used blue GaN LED chips manufactured by Fullsun, 1x1 mm in size with a dominant wavelength of 450 nm and a power of 1W. The phosphors used were $Y_3Al_5O_{12}:Ce^{3+}$ and $Gd_3Al_5O_{12}:Ce^{3+}$ (fig.1) with different peak wavelengths (~ 550 nm and 580 nm respectively) and full widths at half amplitude, the emission spectra of which are shown in fig. 2. LEDs were made as follows: 1) the chips were deposited on a substrate with conductive glue; 2) then heated to 150°C in a furnace; 3) transparent silicone and phosphors were mixed in the ratio of 1 gram of powder to 10 grams of silicone; 4) the $Y_3Al_5O_{12}:Ce^{3+}$ phosphor was mixed with $Gd_3Al_5O_{12}:Ce^{3+}$ in two concentrations - 10% and 20% (the total amount of powder and encapsulant remains unchanged), and one of the samples remained free of $Gd_3Al_5O_{12}:Ce^{3+}$ for comparison; 5) phosphor composites were dispensed and completely cured. Dispensed materials in each package were carefully weighed at each distribution to ensure that: a) the same amount of encapsulating material was used in each package; b) the encapsulation height was the same in each LED within a small error.

3. RESULTS AND DISCUSSION

The emission spectra of samples with all three concentrations of $Gd_3Al_5O_{12}:Ce^{3+}$ are shown in Figure 3. The converted spectrum of these three LEDs is wide, covering the wavelength range from 400 to 650 nm, including a significant presence of red in the spectrum in case of $Gd_3Al_5O_{12}:Ce^{3+}$ presence. All three spectra consist of a peak at 450 nm with a full width at half amplitude of 75 nm and each of the three phosphor compositions has its own spectrum band, which have different peak intensities and full widths at half amplitude. For pure $Y_3Al_5O_{12}$: Ce^{3+} phosphor, the peak value is at 530 nm, and the full width at half amplitude -91 nm; with the addition of 10% $Gd_3Al_5O_{12}:Ce^{3+}$ the peak value is 562 nm, and the full width at half amplitude is 100 nm; and with the addition of 20% $Gd_3Al_5O_{12}:Ce^{3+}$, these values are 570 nm and 83 nm.

Table 1 shows the results of the LEDs' optical measurements. Although the red phosphor should have less conversion efficiency than yellow, due to greater Stokes shift, the amount of yellow emission in this case is reduced, but the red emission compensates for the decline by its contribution in the total light flux. As a result, the luminous flux shows ever so slightly higher value with an increase in the concentration of red $Gd_3Al_5O_{12}:Ce^{3+}$ to 20%. In contrast, the color temperature decreases with increasing concentration of $Gd_3Al_5O_{12}:Ce^{3+}$, since the red component is added to the radiation spectrum, as can be seen from fig. 3. The color rendering index is maximal at the concentration

131, H. Javid ave., AZ-1143, Baku
ANAS, G.M. Abdullayev Institute of Physics
E-mail: jophphysics@gmail.com

of $Gd_3Al_5O_{12}:Ce^{3+}$ equal to 10%, and this ratio is optimal for obtaining white light, since it is obvious that with a further increase in the percentage of $Gd_3Al_5O_{12}:Ce^{3+}$, the coordinates of the resulting emission will have shifted far into the red region.

Packaging of white LEDs with a phosphor composition deposited on a blue emitting LED chip can be interpreted from the point of view of their color coordinates in the CIE 1931 color chart. The main goal is to estimate the required amount of phosphor needed for the coordinates to be located at the certain parts of the color diagram. To solve this problem, the method described below is used. It is based on calculating the distance d separating the color coordinate of the white LED and the position of the blue LED on the CIE color diagram:

$$d = \sqrt{(x_{white} - x_{blue})^2 + (y_{white} - y_{blue})^2} \quad (1)$$

where *x* and *y* are the coordinates corresponding to the points of the blue chip and the yellow phosphor, which can be used to calculate the position of the resulting color coordinate.

Fig. 4 shows the CIE 1931 coordinates of the blue chip and both of the phosphors, which are connected by black dashed lines, and it is obvious that these line segments do not intersect the parts of the Planck curve with a color temperature close to 6500K. The blue LED determines one position on the color chart, the coordinates of the phosphors set the other two point. The color of the LED created by the combination of the phosphor and the chip, has to be located on a line connecting their coordinates on the CIE diagram [5,6]. The resulting coordinate of the composition of the two phosphors is situated between the two coordinates of the phosphors, and the line connecting it with the coordinate corresponding to the blue chip will intersect the resulting coordinates inherent to this LED. The coordinate of the resulting white emission of the blue emitting chip and phosphors will be located somewhere in this segment, depending on the amount of applied phosphor. With an increase in the concentration of either of the two phosphors, the resulting line will shift to the side corresponding to the coordinate of this phosphor, which, in this case, is the side of wavelength decrease (blue shift), in accordance with the equation (1).

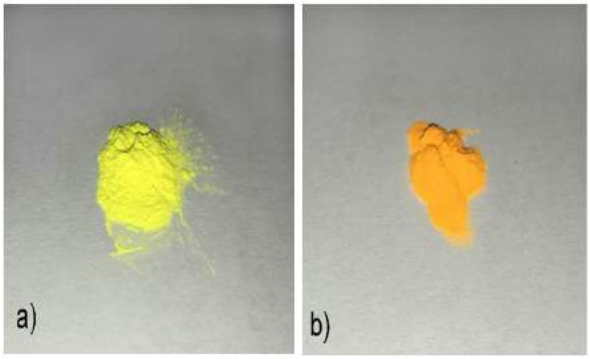

Fig. 1. a) $Y_3Al_5O_{12}:Ce^{3+}$ b) $Gd_3Al_5O_{12}:Ce^{3+}$ phosphors.

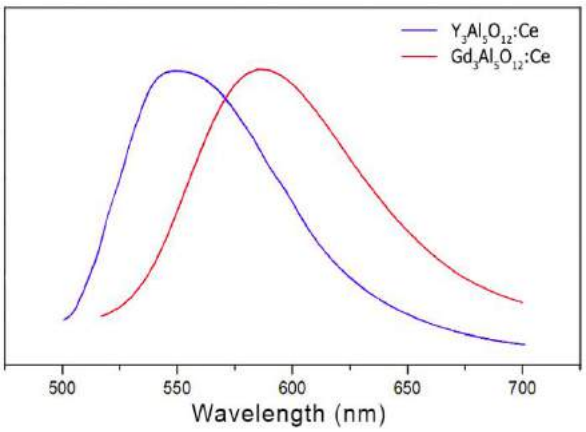

Fig. 2. a) $Y_3Al_5O_{12}:Ce^{3+}$ b) $Gd_3Al_5O_{12}:Ce^{3+}$ emission spectra.

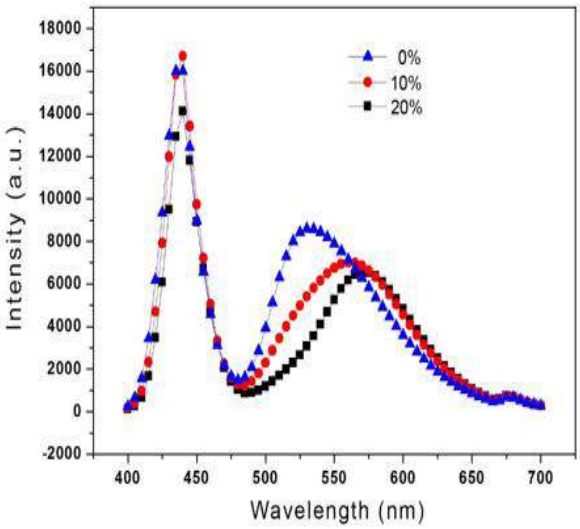

Fig. 3. Emission spectra of LEDs with different concentrations of $Gd_3Al_5O_{12}:Ce^{3+}$.

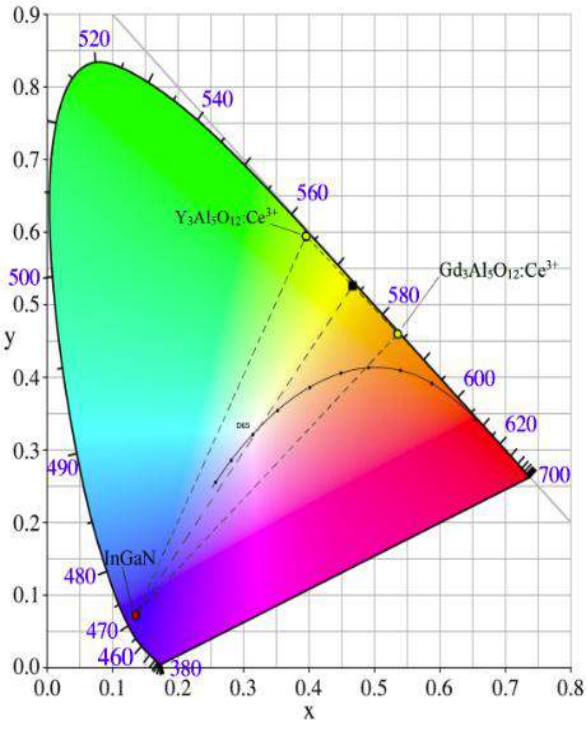

Fig. 4. CIE 1931 diagram depicting LEDs' chromaticity.

Table 1

Light parameters at various concentrations of $Gd_3Al_5O_{12}:Ce^{3+}$

Concentration $Gd_3Al_5O_{12}:Ce^{3+}$	CCT, K	R_a	Flux, Lm	CIE X	CIE Y
0%	7134	70	73,1	0.334	0.256
10%	6433	75	75,3	0.315	0.307
20%	5204	71	79,2	0.328	0.332

4. CONCLUSION

The conducted study shows, as seen from the chromaticity coordinates, that addition of a $Gd_3Al_5O_{12}:Ce^{3+}$ phosphor with enhanced red emission improves the color characteristics of the phosphor converted LED, bringing the coordinates closer to pure white light. The concentration of 10% $Gd_3Al_5O_{12}:Ce^{3+}$ phosphor shows the best results at obtaining white light in phosphor converted WLED improving its CCT, R_a and luminous efficiency. The use of several phosphors with different chemical compositions is a good alternative to multiple chip LEDs of different wavelengths, allowing to obtain white light.

[1] *Z. Liu, S. Liu, K. Wang, X. Luo*. Measurement and numerical studies of optical properties of YAG:Ce phosphor for white light-emitting diode packaging. Applied Optics, 2010, v. 49, №. 2, pp. 247-257.

[2] *A. Lakshmanan, S. Kumar.* Synthesis, photoluminescense and thermal quenching of YAG:Ce phosphor for white light emitting diodes. Indian Journal of Pure & Applied physics, 2011, v. 19, pp. 303-307.

[3] *D. Malacara*. Color vision and colorimetry: theory and applications, SPIE, 2011, p. 188.

[4] *S. Tong*. Effects of doping Pr^{3+} and Gd^{3+} into YAG:Ce phosphors on the luminescence properties. Chemical Journal of Chinese Universities, 2019, v. 29, № 4.

[5] *P. Edwards, E. Taylor* and *R.W. Martin.* Colorimetry and efficiency of white LEDs: Spectral width dependence. Physics Status Solidi (a), 2012, v. 209, №. 3, pp. 461–464

[6] *H.S. Jang, Y.H. Won, D.Y. Jeon*. Improvement of electroluminescent property of blue LED coated with highly luminescent yellow-emitting phosphors. 2009, Applied Physics (b), v.95, №4, pp. 715–720.

Received: 18.10.2019

TWO- AND THREE-PARTICLE DECAY CHANNELS OF SUPERSYMMETRIC HIGGS BOSONS

S.K. ABDULLAYEV, E.Sh. OMAROVA
23, Z. Khalilova str., Baku State University,
Baku, Azerbaijan, AZ 1148
[a]*sabdullayev@bsu.edu.az,* [b]*emiliya.abdullayeva@inbox.ru*

In the framework of the Minimal Supersymmetric Standard Model we investigated the two and three- particle decay channels of Higgs bosons: $H \to W^- W^+$, $H \to Z^0 Z^0$, $A \to hZ^0$, $H^+ \to hW^\pm$, $H \to hh$, $H \to hh$, $H \to hb\bar{b}$, $H \to Z^0 Ah$, $A \to Z^0 hh$, $H^\pm \to W^\pm hh$, $H(A) \to t\bar{b}W^-$. Analytical expressions for the amplitudes and probabilities of the corresponding decays are obtained and the dependence of the widths of the decays on the mass of the Higgs bosons are studied. The calculation results are illustrated by graphs, which the widths of the decays to the Higgs boson mass are very sensitive. In some processes, the width of the decay increases with the increasing mass of the Higgs boson, while in others, on the contrary, it decreases.

Keywords: Standard Model, Minimal Supersymmetric Standard Model, Higgs boson, decay width, coupling constant.
PACS: 12.15-y, 12.15 Mm, 14.70 Hp, 14.80 Bn

INTRODUCTION

The Standard Model (SM) based on local gauge symmetry $SU_C(3) \times SU_L(2) \times U_Y(1)$ and well describes the strong and electroweak interactions of the physics of quarks, leptons and gauge bosons [1-4]. In this case, quarks are triplets and leptons are singlets of the color group $SU_C(3)$, the left components of quarks and leptons are doublets of the group $SU_L(2)$, and the right components are singlets, and they all have a hypercharge according to the group $U_Y(1)$. The discovery of the Higgs boson in 2012 by the ATLAS and CMS collaborations [5, 6] (see also reviews [7–10]) has begun a new stage in the study of the properties of fundamental interactions.The mechanism of fundamental particles of mass generation – the mechanism of spontaneous breaking of the local gauge symmetry of Brout - Englert - Higgs [11, 12] was experimentally confirmed. Thus, the SM received a logical conclusion and acquired the status of a standard theory.

A doublet of scalar complex fields $\varphi = \begin{pmatrix} \varphi^+ \\ \varphi^0 \end{pmatrix}$ is introduced in the SM, the neutral component has a nonzero vacuum value. As a result, the electroweak group $SU_L(2) \times U_Y(1)$ is spontaneously broken up to the electromagnetic group $U_Q(1)$. In this case, three of the four components of the scalar field φ are absorbed by the $W^\pm$- and Z^0-vector bosons, and the remaining fourth neutral component of the scalar field is the Higgs boson H_{SM}. In the first experiments conducted at the Large Hadron Collider (LHC), the main properties of this particle were established. The Higgs boson is a scalar particle with spin zero, possessing positive parity, mass about 125 GeV, interacting with $W^\pm$- and Z^0-bosons, and also quarks and leptons with a constant proportional to their masses. With the discovery of the Higgs boson, interest in various channels of production and decay has greatly increased. The various properties of the Higgs boson have been studied in a number of papers [4,13-19].

Note that along with the SM, other alternative models are widely discussed in the literature. One of the extensions of the SM is the two-doublet Higgs model 2 HDM [20, 21]. Another alternative model is the Minimal Supersymmetric Standard Model (MSSM) [22-26]. In this model, two doublets of the scalar field are introduced with opposite hypercharges –1 and +1:

$$\varphi_1 = \begin{pmatrix} H_1^0 \\ H_1^- \end{pmatrix}, \quad \varphi_2 = \begin{pmatrix} H_2^+ \\ H_2^0 \end{pmatrix}$$

To obtain the Higgs boson physical fields, φ_1 and φ_2 are written as

$$\varphi_1 = \frac{1}{\sqrt{2}} \begin{pmatrix} \upsilon_1 + H_1^0 + iP_1^0 \\ H_1^- \end{pmatrix},$$

$$\varphi_2 = \frac{1}{\sqrt{2}} \begin{pmatrix} H_2^+ \\ \upsilon_2 + H_2^0 + iP_2^0 \end{pmatrix}$$

Here H_1^0, P_1^0, H_2^0 and P_2^0 are the fields describing the system excitations with respect to the vacuum states $\langle \varphi_1 \rangle = \frac{1}{\sqrt{2}} \upsilon_1$ and $\langle \varphi_2 \rangle = \frac{1}{\sqrt{2}} \upsilon_2$. The CP-even Higgs bosons of the H - and h - bosons are obtained by mixing the fields H_1^0 and H_2^0 (mixing angle α):

$$\begin{pmatrix} H \\ h \end{pmatrix} = \begin{pmatrix} \cos\alpha & \sin\alpha \\ -\sin\alpha & \cos\alpha \end{pmatrix} \begin{pmatrix} H_1^0 \\ H_2^0 \end{pmatrix}$$

131, H. Javid ave., AZ-1143, Baku
ANAS, G.M. Abdullayev Institute of Physics
E-mail: jophphysics@gmail.com

Similarly, the fields P_1^0 and P_2^0 are mixed, and also $H_1^{\pm}$ and $H_2^{\pm}$, get a CP-odd Higgs boson A and charged Higgs bosons H^+ and H^- (mixing angle β):

$$\begin{pmatrix} G^0 \\ A \end{pmatrix} = \begin{pmatrix} \cos\beta & \sin\beta \\ -\sin\beta & \cos\beta \end{pmatrix} \begin{pmatrix} P_1^0 \\ P_2^0 \end{pmatrix},$$

$$\begin{pmatrix} G^{\pm} \\ H^{\pm} \end{pmatrix} = \begin{pmatrix} \cos\beta & \sin\beta \\ -\sin\beta & \cos\beta \end{pmatrix} \begin{pmatrix} H_1^{\pm} \\ H_2^{\pm} \end{pmatrix}$$

where G^0 and $G^{\pm}$ are neutral and charged massless bosons. Therefore, after spontaneous symmetry breaking, five Higgs particles appear in the MSSM: CP-even h- and H-bosons, CP-odd A-boson, and charged $H^{\pm}$-bosons.

In the MSSM, the Higgs sector is characterized by six parameters $M_h, M_H, M_A, M_{H^{\pm}}, \alpha$ and β. Of these, only two parameters are free, and $tg\beta$ and M_A are usually chosen as such parameters. The parameter $tg\beta$ is equal to the ratio $\frac{\upsilon_2}{\upsilon_1}$ and varies within

$$1 \le \tan\beta \le \frac{m_t}{m_b} = 35{,}5,$$

where $m_t = 173{,}2$ GeV and $m_b = 4{,}88$ GeV are the masses of t- and b-quarks.

The masses of neutral h- and H-(charged $H^{\pm}$-) bosons are expressed in masses M_A and M_Z (M_A and M_W):

$$M^2_{H(h)} = \frac{1}{2}\left[M_A^2 + M_Z^2 \pm \sqrt{(M_A^2 + M_Z^2)^2 - 4M_A^2 M_Z^2 \cos^2 2\beta} \right],$$

$$M^2_{H^{\pm}} = M_A^2 + M_W^2.$$

It follows that between the masses of supersymmetric Higgs bosons there is a relationship

$$M_h < M_A < M_H < M_{H^{\pm}}$$

The mixing angles of fields α and β are related by:

$$\tan 2\alpha = \tan 2\beta \frac{M_A^2 + M_Z^2}{M_A^2 - M_Z^2}, \quad \left(-\frac{\pi}{2} \le \alpha < 0 \right).$$

The Higgs bosons of the MSSM can decay through various channels (see [25,27-29] and there are references to primary sources). In previous works [30–32], we considered the Higgs boson decay channels of the MSSM into an arbitrarily polarized fermion pair $H(h,A) \to f + \bar{f}$, $H^+ \to f + \bar{f}'$ and also three-particle $H(A) \to t + \bar{b} + W^-$, $H^{\pm} \to b + \bar{b} + W^{\pm}$, $H \to Z^0 + f + \bar{f}$, $H \to W^{\pm} + f + \bar{f}'$ decays.

In this paper, we study some two and three-particle decay channels for supersymmetric Higgs bosons:

$$H \to W^- + W^+,\ H \to Z^0 + Z^0 \quad (1)$$

$$A \to Z^0 + h,\ H^{\pm} \to W^{\pm} + h \quad (2)$$

$$H \to h + h,\ H \to h + b + \bar{b} \quad (3)$$

$$A \to Z^0 + h + h,\ H^{\pm} \to W^{\pm} + h + h \quad (4)$$

$$H(A) \to H^{+*} + W^- \to t + \bar{b} + W^-,\quad H \to W^{+*} + W^- \to t + \bar{b} + W^- \quad (5)$$

Analytical expressions are obtained for the amplitudes and probabilities of the corresponding decays, and the dependence of the decay width on the Higgs boson mass is studied.

2. The decays of $H \to W^-W^+$ and $H \to Z^0Z^0$

First, consider the decay of the heavy Higgs H boson into gauge bosons W^-W^+ (Z^0Z^0). This process is described by the Feynman diagram shown in fig. 1 a (4-particle momenta are written in brackets). To this diagram corresponds the amplitude:

$$M(H \to VV) = ig_{HVV} H(p) \cdot U_\mu^*(p_1) \cdot U_\mu^*(p_2) \quad (6)$$

where g_{HVV} is the Higgs boson coupling constant H with gauge VV bosons (expressions of various coupling constants are given in [25]), $H(p)$ is the H-boson wave function normalized to unity, $U_\mu^*(p_1)$ and $U_\mu^*(p_2)$ are 4 polarization vectors of gauge W^-W^+ (Z^0Z^0)-bosons.

For the decay width $H \to V + V$, summed over the polarization states of the vector bosons, the expression is obtained:

$$\Gamma(H \to VV) = \frac{G_F M_H^3}{8\sqrt{2}\pi} \cdot \cos^2(\beta - \alpha)(1 - 4r_V + 12r_V^2)\sqrt{1 - 4r_V} \cdot \delta_V. \quad (7)$$

The $r_V = \left(\frac{M_V}{M_H} \right)^2$ designation is entered here and it is taken into account

$$g^2_{HVV} = 4\sqrt{2} G_F M_V^4 \cos^2(\beta - \alpha),$$

G_F is the Fermi constant of weak interactions a

$\delta_W = 1$ in the case of the production of charged W^-W^+ bosons, $\delta_Z = \frac{1}{2}$ at the production of neutral Z^0-bosons.

Figure 2 shows the dependence of the decay widths $H \to W^-W^+$ and $H \to Z^0Z^0$ on the Higgs mass of the M_H boson at $tg\beta = 3$ and $M_W = 80{,}425$

GeV, and $M_Z = 91{,}1875$ GeV. As can be seen, with increasing Higgs boson mass, the decay width monotonously increases, the decay width $\Gamma(H \to W^- W^+)$ prevails over the decay width $\Gamma(H \to Z^0 Z^0)$.

As is known, a massive vector particle is characterized by three independent polarization vectors: two transverse (with respect to the k 3-momentum of the particle) and one longitudinal:

$$U_\mu^{(1)} = (0,1,0,0) \ , \ U_\mu^{(2)} = (0,0,1,0) \ , \ U_\mu^{(L)} = \left(\frac{|\vec{k}|}{M_W}, 0, 0, \frac{E}{M_W} \right) \ ,$$

$$U_\mu^{(i)} \cdot k_\mu = 0 \ , \ k_\mu = (E,0,0,|\vec{k}|) \ , \ (U_\mu^{(i)})^2 = -1 \ , \tag{8}$$

where E and $\vec{k}$ are the energy and the 3-momentum of the vector boson, the Z axis is chosen along the momentum $\vec{k}$. It can be seen from (8) that the components of the 4 -vector of longitudinal polarization $U_\mu^{(L)}$ turn out to grow with an increase in the energy of the vector boson. Therefore, the decay width of the formation of longitudinally polarized $W^- W^+$ ($Z^0 Z^0$) -bosons will increase with increasing mass M_H.

The width of the Higgs boson decay into a pair of longitudinally polarized vector bosons is given by the formula:

$$\Gamma(H \to V_L V_L) = \frac{G_F M_H^3}{8\sqrt{2}\pi} \cos^2(\beta - \alpha)(1 - 4r_V + 4r_V^2)\sqrt{1 - 4r_V}\,\delta_V \tag{9}$$

This means that for large Higgs masses of the M_H boson, vector bosons are predominantly polarized longitudinally. Consider the decay width ratio

$$\frac{\Gamma(H \to V_L V_L)}{\Gamma(H \to VV)} = \frac{1 - 4r_V + 4r_V^2}{1 - 4r_V + 12r_V^2} . \tag{10}$$

Figure 3 illustrates the dependence of the $\Gamma(H \to V_L V_L)/\Gamma(H \to VV)$ ratio on the mass of M_H. As can be seen, with increasing M_H mass, this ratio increases and at large M_H approaches 1.

3. The decays of $A \to Z^0 h$ and $H^\pm \to W^\pm h$

The Feynman diagram of the decay of the pseudoscalar A -boson into the vector Z^0 -boson and the scalar h -boson is shown in fig. 1 b) and to this diagram corresponds the amplitude

$$M(A \to Z^0 h) = i g_{AZh} A(p) \cdot h^*(p_1) \cdot U_\mu^*(p_2) R_\mu \tag{11}$$

where g_{AZh} is the coupling constant, $A(p)$ and $h^*(p_1)$ are the wave functions of A and h -bosons normalized to unity, $U_\mu^*(p_2)$ is the 4-polarization vector of the Z^0 boson, $R_\mu = (p + p_1)_\mu$ is the sum of 4-impulses of A and h -bosons. Based on the matrix element (11), the expression for the decay width $A \to Z^0 h$ is obtained:

$$\Gamma(A \to Z^0 h) = \frac{G_F}{8\sqrt{2}\pi M_A^3} \cos^2(\beta - \alpha)[(M_A^2 - M_Z^2 - M_h^2)^2 - 4M_Z^2 M_h^2]^{3/2} \tag{12}$$

The Feynman decay diagram of the $H^\pm \to W^\pm h$ is similar to the diagram in fig. 1 (c) and we write the corresponding matrix element as follows:

$$M(H^\pm \to W^\pm h) = \pm i g_{H^\pm W^\pm h} H^\pm(p) \cdot h^*(p_1) \cdot U_\mu^*(p_2) R_\mu \tag{13}$$

Having performed the calculations according to the usual MSSM rules, for the decay width $H^\pm \to W^\pm h$ we have the following expression

$$\Gamma(H^\pm \to W^\pm h) = \frac{G_F}{8\sqrt{2}\pi M_{H^\pm}^3} \cos^2(\beta - \alpha)[(M_{H^+}^2 - M_h^2 - M_W^2)^2 - 4M_W^2 M_h^2]^{3/2} \ . \tag{14}$$

Figure 4 shows the dependence of the decay width $A \to Z^0 h$ and $H^\pm \to W^\pm h$ on the mass M_A and $M_{H^\pm}$ at $tg\beta = 3$, $M_Z = 91{,}1875$ GeV and $M_W = 80{,}425$ GeV. As the mass of the Higgs boson $M_A (M_{H^\pm})$ increases, the width of the decay $\Gamma(A \to Z^0 h)(\Gamma(H^\pm \to W^\pm h))$ increases.

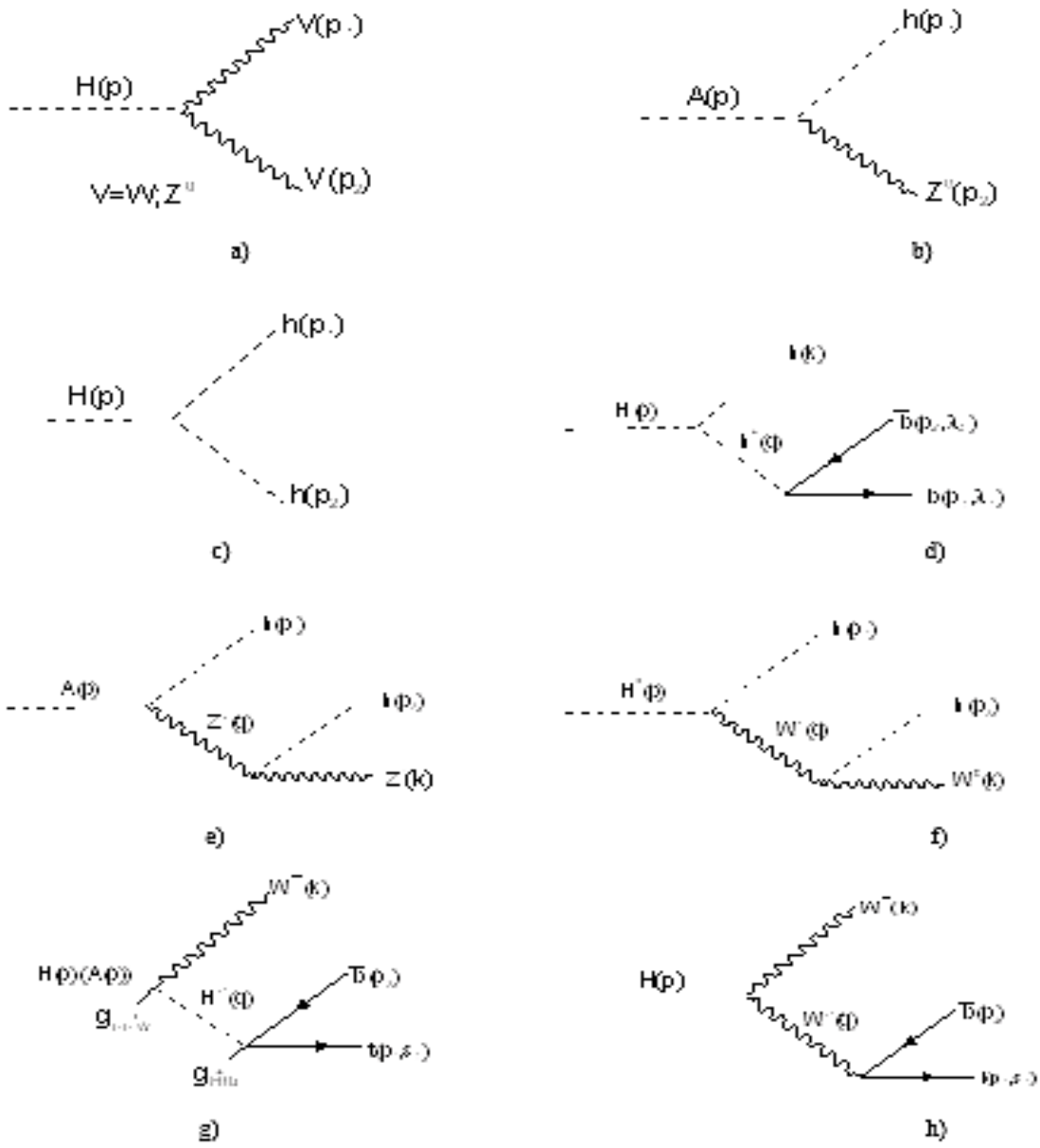

Fig. 1. Feynman diagrams for various Higgs boson decay channels

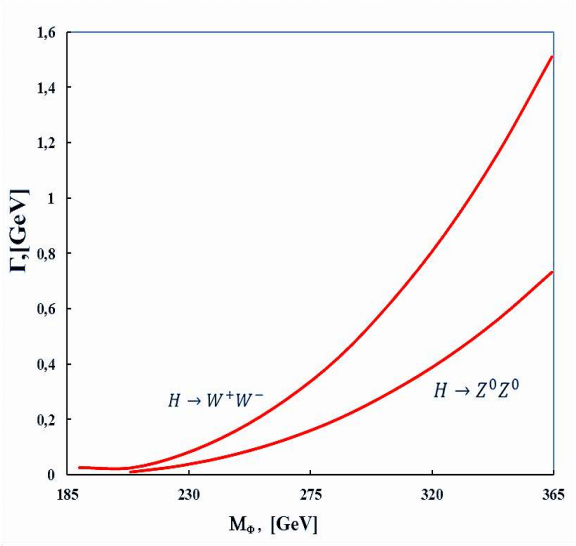

Fig. 2. Dependence of the decay width $\Gamma(H \to W^-W^+)$ and $\Gamma(H \to Z^0Z^0)$ on the mass M_H at $tg\beta = 3$

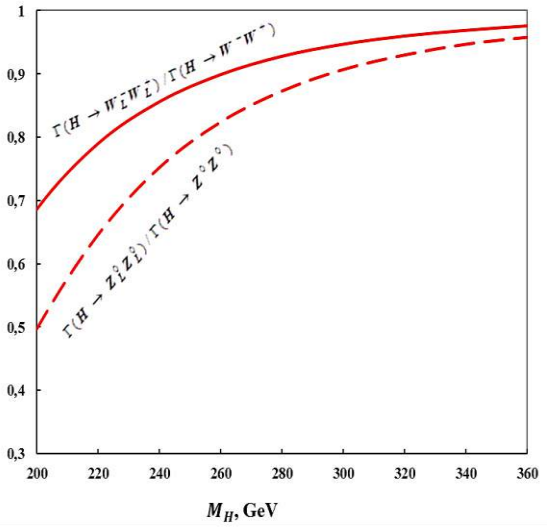

Fig.3. Dependence of $\Gamma(H \to W_L^-W_L^+)/\Gamma(H \to W^-W^+)$ and $\Gamma(H \to Z_L^0Z_L^0)/\Gamma(H \to Z^0Z^0)$ ratios on M_H

4. The decays of $H \to hh$ and $H \to hb\bar{b}$

One of the possible channels for the decay of a heavy Higgs boson is its decay into two light h - bosons: $H \to h + h$. The diagram of this decay is shown in fig. 1 (c). The amplitude of this decay can be written as:

$$M(H \to hh) = ig_{Hhh} H(p) \cdot h^*(p_1) \cdot h^*(p_2) \qquad (15)$$

The decay width of this process is:

$$\Gamma(H \to hh) = \frac{G_F}{16\sqrt{2}\pi} \frac{M_Z^4}{M_H} \sqrt{1-4r_h} \cdot g_{Hhh}^2 \qquad (16)$$

where $r_h = \left(\frac{M_h}{M_H}\right)^2$. Figure 5 shows the dependence of the decay width $H \to h + h$ on the mass M_h for two values of the parameter $tg\beta$. In both cases, the decay width monotonically decreases with increasing mass of the Higgs boson M_H.

When $M_h < M_H \le 2M_h$, the Higgs boson H decays through the $H \to h + h^* \to h + b + \bar{b}$ channel, the Feynman diagram of which is shown in fig. 1 d) (h^* -virtual Higgs boson). The amplitude of this decay is

$$M(H \to hb\bar{b}) = ig_{Hhh} \cdot g_{hbb} \frac{H(p) \cdot h^*(k)}{(p_1 + p_2)^2 - M_h^2 + iM_h\Gamma_h} \bar{u}(p_1, \lambda_1) \cdot \upsilon(p_2, \lambda_2) \qquad (17)$$

here g_{Hhh} and g_{hbb} are the corresponding coupling constants, λ_1 and λ_2 are the helicities of the b -quark and $\bar{b}$ -antiquark, M_h and Γ_h are the mass and width of the decay of the h -boson.

We introduce the scaling energies of the b -quark $x_1 = \frac{2E_1}{M_H}$, $\bar{b}$ - antiquark $x_2 = \frac{2E_2}{M_H}$ and h - boson $x_h = \frac{2E_h}{M_H} = 2 - x_1 - x_2$, as well as the notation $r_b = \left(\frac{m_b}{M_H}\right)^2$, $r_h = \left(\frac{m_h}{M_H}\right)^2$, $\gamma_h = \left(\frac{\Gamma_h}{M_H}\right)^2$. Then for the decay width $H \to h + b + \bar{b}$ we have the expression:

$$\frac{d\Gamma(H \to hb\bar{b})}{dx_1 dx_2} = \frac{N_C G_F^2 M_Z^4 m_b^2}{64\pi^3 M_H} \cdot \frac{\sin^2\alpha}{\cos^2\beta} \cdot \lambda_{Hhh}^2 \cdot (1 + \lambda_1\lambda_2) \frac{1 - x_h + r_h - 2r_b}{(1 - x_h)^2 + r_h\gamma_h} \qquad (18)$$

Here it is taken into account

$$g_{Hhh}^2 = 4\sqrt{2} G_F M_Z^4 \lambda_{Hhh}^2, \quad \lambda_{Hhh} = 2\sin 2\alpha \sin(\beta + \alpha) - \cos 2\alpha \cos(\beta + \alpha), \quad g_{hbb}^2 = \sqrt{2} G_F m_b^2 \cdot \frac{\sin^2\alpha}{\cos^2\beta}$$

From the decay width (18) it follows that b -quark and $\bar{b}$ -antiquark must have the same helicity: $\lambda_1 = \lambda_2 = \pm 1$, or they are polarized right ($b_R\bar{b}_R$), or left ($b_L\bar{b}_L$). This is due to the law of conservation of the total moment in the transition $h^* \to b + \bar{b}$ .The decay width $H \to h + b + \bar{b}$, summed over the spin states of quarks, has the form (Dalitz distribution):

$$\frac{d\Gamma(H \to hb\bar{b})}{dx_1 dx_2} = \frac{N_C G_F^2 M_Z^4 m_b^2}{16\pi^3 M_H} \cdot \frac{\sin^2\alpha}{\cos^2\beta} \cdot \lambda_{Hhh}^2 \cdot \frac{x_1 + x_2 - 1 + r_h - 2r_b}{(1 - x_1 - x_2)^2 + r_h\gamma_h} \qquad (19)$$

The quark scaling energies vary within $1 - x_2 - r_h < x_1 < 1 - \frac{r_h}{1 - x_2}$, $0 < x_2 < 1 - r_h$, then the integration of the Dalitz distribution density (19) over these variables can be performed analytically. As a result, the expression for the decay width $H \to h + h^* \to h + b + \bar{b}$ is obtained (with $r_b = \gamma_b = 0$):

$$\Gamma(H \to hb\bar{b}) = \frac{3G_F^2}{16\pi^3} \cdot \frac{M_Z^4}{M_H} m_b^2 \lambda_{Hhh}^2 \frac{\sin^2\alpha}{\cos^2\beta} \times \left[(1 - r_h)\left(2 - \frac{1}{2}\ln r_h\right) - \frac{1 - 5r_h}{\sqrt{1 - 4r_h}} \left(arctg \frac{2r_h - 1}{\sqrt{1 - 4r_h}} - arctg \frac{1}{\sqrt{1 - 4r_h}} \right) \right]. \qquad (20)$$

Figure 6 illustrates the dependence of the width of the decay $\Gamma(H \to hb\bar{b})$ on the mass of the Higgs boson M_H at $tg\beta = 3$. As can be seen, with an increase in the Higgs boson mass, the width of the decay $H \to h + b + \bar{b}$ first increases and reaches a maximum at $M_H = 144{,}62$ GeV, and then the width of this decay slowly decreases.

5. The decays of $A \to Z^0 hh$ and $H^\pm \to W^\pm hh$

We note that not only with the two-particle Higgs boson decays $A \to Z^0 + h$ and $H^\pm \to W^\pm + h$, but also three-particle $A \to Z^0 + h + h$ and $H^\pm \to W^\pm + h + h$ decays are possible. In this case, the additional h-boson is emitted by the vector $Z^0(W^\pm)$-boson (see fig. 1 (e) and f)), where the Feynman diagrams of these decays are presented.).

According to the MSSM rules, the decay of $A \to Z^0 + h + h$ corresponds to the amplitude

$$M(A \to Zhh) = ig_{AZh} \cdot g_{ZZh} \cdot R_\mu \left(-g_{\mu\nu} + \frac{q_\mu q_\nu}{M_Z^2} \right) \cdot \frac{U_\nu^*(k)}{q^2 - M_Z^2 + iM_Z\Gamma_Z} \tag{21}$$

where g_{AZh} and g_{ZZh} are the corresponding coupling constants, $U_\nu^*(k)$ is the 4-vector of the Z^0-boson polarization.

On the basis of (21) for the square of the matrix element of the decay $A \to Z^0 + h + h$ we get the expression:

$$\left|M(A \to Zhh)\right|^2 = \frac{g_{AZh}^2 \cdot g_{ZZh}^2}{(q^2 - M_Z^2)^2 + M_Z^2\Gamma_Z^2} \cdot R_\mu R_\alpha \left(-g_{\mu\nu} + \frac{q_\mu q_\nu}{M_Z^2} \right) \cdot \left(-g_{\alpha\beta} + \frac{q_\alpha q_\beta}{M_Z^2} \right) \cdot \left(-g_{\beta\nu} + \frac{k_\beta k_\nu}{M_Z^2} \right) =$$

$$= 2G_F^2 M_Z^4 \sin^2(\beta - \alpha) \cos^2(\beta - \alpha) \cdot \frac{f_Z}{(1 - x_1 + r_h - r_Z)^2 + r_Z\gamma_Z} \tag{22}$$

Here is the function

$$f_Z = -4r_Z(1 + x_1 + r_h)^2 + 4(1 - r_h)^2 \left[2 - \frac{1}{r_Z}(1 - x_1 + r_h) + \frac{1}{4r_Z^2}(1 - x_1 + r_Z)^2 \right] +$$

$$+ (1 + x_Z - x_2 - r_Z)^2 - \frac{2}{r_Z}(1 - r_h)(1 + x_Z - x_2 - r_Z)(1 - x_1 - r_Z) \tag{23}$$

$x_1 = \frac{2E_1}{M_A}$, $x_2 = \frac{2E_2}{M_A}$ and $x_Z = \frac{2E_Z}{M_A} = 2 - x_1 - x_2$ are the scaling energies of the h-bosons and the Z^0-boson, $r_h = \left(\frac{M_h}{M_A}\right)^2$, $r_Z = \left(\frac{M_Z}{M_A}\right)^2$, $\gamma_Z = \left(\frac{\Gamma_Z}{M_A}\right)^2$ and it is taken into account that according to the MSSM $g_{AZh}^2 \cdot g_{ZZh}^2 = 2G_F^2 M_Z^4 \sin^2(\beta - \alpha)\cos^2(\beta - \alpha)$.

The width of the decay $A \to Z^0 + h + h$ is directly proportional to the square of the amplitude (22)

$$\frac{d\Gamma(A \to Z^0 hh)}{dx_1 dx_2} = \frac{\left|M(A \to Z^0 hh)\right|^2}{2^8 \pi^3} M_A = \frac{G_F^2 M_Z^4 M_A}{2^7 \pi^3} \cdot \sin^2(\beta - \alpha)\cos^2(\beta - \alpha) \cdot \frac{f_Z}{(1 - x_1 + r_h - r_Z)^2 + r_Z\gamma_Z}. \tag{24}$$

Consider the width of the decay $A \to Z^0 + h + h$, normalized to the width of the usual decay $A \to Z^0 + h$:

$$\frac{1}{\Gamma(A \to Z^0 h)} \cdot \frac{d\Gamma(A \to Z^0 hh)}{dx_1 dx_2} = \frac{G_F M_Z^4}{8\sqrt{2}\pi^2 M_A^2} \sin^2(\beta - \alpha) \cdot \frac{f_Z}{(1 - x_1 + r_h - r_Z)^2 + r_Z\gamma_Z} \cdot [(1 - r_Z - r_h)^2 - 4r_Z r_h]^{-3/2} \tag{25}$$

Figure 7 shows the dependence of the normalized decay width (25) on the scaling energy x_1 at a fixed $x_2 = 0{,}5$, $M_A = 220$ GeV, $tg\beta = 3$, $M_Z = 91{,}1875$ GeV. As can be seen, with an increase in the scaling energy x_1, the normalized decay width $\frac{1}{\Gamma(A \to Z^0 h)} \cdot \frac{d\Gamma(A \to Z^0 hh)}{dx_1 dx_2}$ decreases.

The decay of $H^\pm \to W^\pm + h + h$ corresponds to the diagram shown in fig. 1 (f) and the amplitude of this decay can be written as:

$$M(H^\pm \to W^\pm hh) = ig_{H^\pm W^\pm h} \cdot g_{WWh} \cdot R_\mu \left(-g_{\mu\nu} + \frac{q_\mu q_\nu}{M_W^2} \right) \cdot \frac{U_\nu^*(k)}{q^2 - M_W^2 + iM_W\Gamma_W} \tag{26}$$

where $g_{H^\pm W^\pm h}$ and g_{WWh} are the corresponding coupling constants, $U_\nu^*(k)$ is the 4-polarization vector of the W-boson.

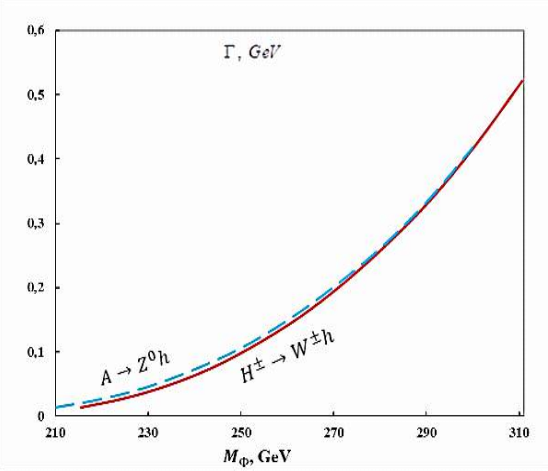

Fig.4. The dependence of the width of the decay $A \to Z^0 h$ $(H^{\pm} \to W^{\pm} h)$ on the mass $M_A (M_{H^{\pm}})$

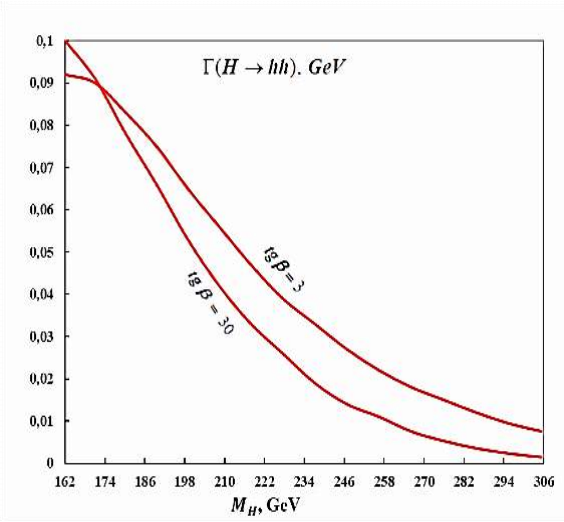

Fig. 5. Dependence of the decay width $H \to hh$ on the mass M_H

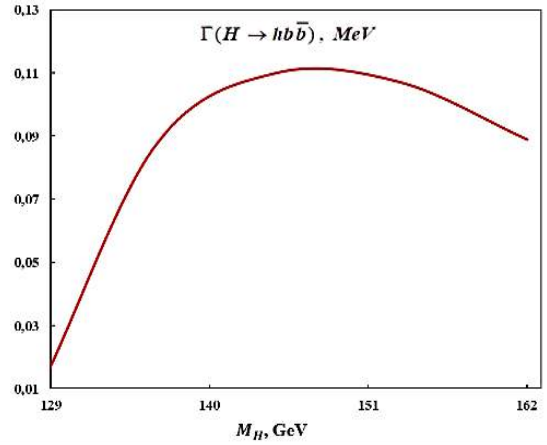

Fig. 6. Dependence of the decay width $H \to hb\bar{b}$ on the mass M_H

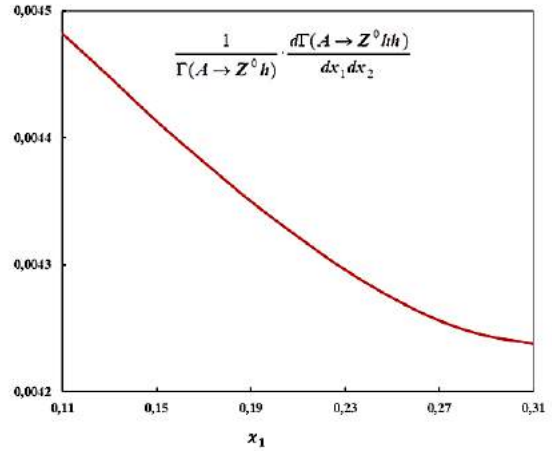

Fig .7. Dependence of the ratio $\frac{1}{\Gamma(A \to Z^0 h)} \cdot \frac{d\Gamma(A \to Z^0 hh)}{dx_1 dx_2}$ on x1

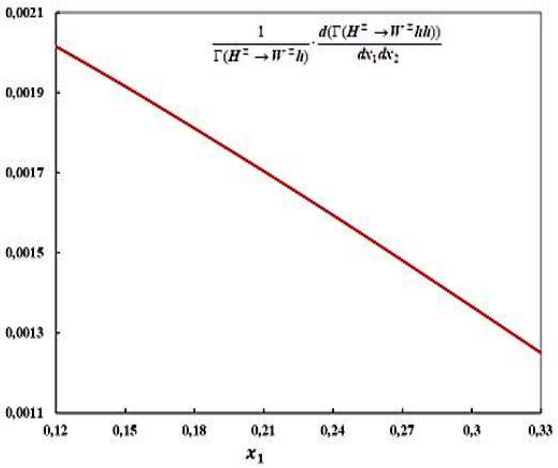

Fig.8. Dependence of the ratio $\frac{1}{\Gamma(H^{\pm} \to W^{\pm} + h)} \cdot \frac{d\Gamma(H^{\pm} \to W^{\pm} hh)}{dx_1 dx_2}$ on x_1.

The distribution density of Dalits in the decay of $H^{\pm} \to W^{\pm} + h + h$ is expressed by the formula

$$\frac{d\Gamma(H^{\pm} \to W^{\pm} hh)}{dx_1 dx_2} = \frac{G_F^2 M_W^4 M_{H^{\pm}}}{2^7 \pi^3} \cdot \sin^2(\beta - \alpha) \cdot \frac{f_W}{(1 - x_1 + r_h - r_W)^2 + r_W \gamma_W}, \quad (27)$$

where the function f_W is obtained from the function f_Z by replacing $r_Z \Rightarrow r_W$.

The width of the decay $H^{\pm} \to W^{\pm} + h + h$ is normalized to the width of the usual decay $H^{\pm} \to W^{\pm} + h$:

$$\frac{1}{\Gamma(H^{\pm} \to W^{\pm} + h)} \cdot \frac{d\Gamma(H^{\pm} \to W^{\pm} hh)}{dx_1 dx_2} = \frac{G_F M_W^4}{8\sqrt{2}\pi^2 M_{H^{\pm}}^2} \sin^2(\beta - \alpha) \times \frac{f_W}{(1 - x_1 + r_h - r_W)^2 + r_W \gamma_W} \cdot [(1 - r_W - r_h)^2 - 4 r_W r_h]^{-3/2} \quad (28)$$

Figure 8 illustrates the dependence of the normalized decay width (28) on the scaling energy x_1 at a fixed $x_2 = 0{,}5$, $M_{H^\pm} = 200$ GeV, $tg\beta = 3$, $M_W = 80{,}425$ GeV. Here, a monotonous decrease of the normalized decay width is observed with increasing scaling energy x_1 .

6. The decays of $H(A) \to t\bar{b}W^-$

One of the interesting channels for the Higgs boson decay is $H(A) \to t + \bar{b} + W^-$. This decay can occur through various virtual states. The decay channel according to the scheme $H(A) \to t + \bar{t}^* \to t + \bar{b} + W^-$ was investigated by us in [32]. These decays can also occur through the virtual charged Higgs boson $H(A) \to H^{+*} + W^- \to t + \bar{b} + W^-$. In addition, the scalar Higgs boson H can also decay according to the scheme $H(A) \to W^{+*} + W^- \to t + \bar{b} + W^-$. We note that the decay of the pseudoscalar A -boson according to the scheme $A \to W^{+*} + W^-$ is forbidden by the law of conservation of CP parity.

Now let us consider the decay of the $H(A)$-boson via the $H(A) \to H^{+*} + W^- \to t + \bar{b} + W^-$ channel, the Feynman diagram which is shown in fig. 1 (g). The amplitude of this decay is written as follows:

$$M(H \to W^- H^{+*}) = ig_{HH^+W} \cdot U^*_{\mu}(k) \cdot g_{H^+tb} \cdot R_{\mu} \cdot \frac{U^*_{tb}}{q^2 - M^2_{H^+} + iM_{H^+}\Gamma_{H^+}} \times$$
$$\times \bar{u}(p_1, s_t)[m_b tg\beta(1-\gamma_5) + m_t ctg\beta(1+\gamma_5)]\upsilon(p_2) \tag{29}$$

where U_{tb} is an element of the Kobayashi-Maskawa matrix, g_{HH^+W} and g_{H^+tb} are the corresponding coupling constants, s_t is the 4-polarization vector of the t -quark. For the square of the amplitude (29) the expression is obtained

$$\left|M(H \to W^- H^{+*})\right|^2 = 4g^2_{HH^+W} g^2_{H^+tb} \frac{|U_{tb}|^2}{(q^2 - M^2_{H^+})^2 + M^2_{H^+}\Gamma^2_{H^+}} \cdot \left(-R^2 + \frac{(R\cdot k)^2}{M^2_W}\right) \cdot [(p_1 \cdot p_2)(m_b^2 tg^2\beta + m_t^2 ctg^2\beta) -$$
$$- 2m_t^2 m_b^2 - m_t(p_2 \cdot s_t)(m_b^2 tg^2\beta - m_t^2 ctg^2\beta)] \tag{30}$$

We carry the scaling energies of the t -quark $x_t = \frac{2E_t}{M_H}$, $\bar{b}$ -antiquark $x_b = \frac{2E_b}{M_H}$ and W^- -boson $x_W = \frac{2E_W}{M_H} = 2 - x_t - x_b$, the scaling masses $r_b = \left(\frac{m_b}{M_H}\right)^2$, $r_t = \left(\frac{m_t}{M_H}\right)^2$ and $r_{H^+} = \left(\frac{M_{H^+}}{M_H}\right)^2$.

The width of the Higgs boson decay in the $H \to t + \bar{b} + W^-$ channel is expressed by the formula

$$d\Gamma(H \to tbW^-) = \frac{(2\pi)^4}{2M_H} \cdot \left|M(H \to tbW^-)\right|^2 N_C \frac{d\vec{k}}{(2\pi)^3 2E_W} \cdot \frac{d\vec{p}_1}{(2\pi)^3 2E_t} \cdot \frac{d\vec{p}_2}{(2\pi)^3 2E_b} \cdot \delta(p - p_1 - p_2 - k) \tag{31}$$

We define the spectrum of quarks in the case of a longitudinally polarized t -quark (the helicity of the t -quark is denoted by λ_t). For this, we need to take the integral over the phase volume of the W^- -boson. Then the expression for the decay width will be:

$$d\Gamma(H \to tbW^-) = \frac{N_C}{16M_H(2\pi)^5} \cdot \int \frac{\overline{\left|M(H \to tbW^-)\right|^2}}{E_W E_t E_b} d\vec{p}_1 \, d\vec{p}_2 \cdot \delta(M_H - E_t - E_b - E_W) \tag{32}$$

where the bar above the square of the matrix element means that, by the polarizations of the antiquark $\bar{b}$ is summed. Now, by integrating the angles of departure of the t and $\bar{b}$ quarks, for the decay width $H \to t + \bar{b} + W^-$ we obtain the expression

$$\frac{d\Gamma(H \to t\bar{b}W^-)}{dx_t dx_b} = \frac{N_C G_F^2 M_H^5}{128\pi^3} \cdot \frac{|U_{tb}|^2 (x_W^2 - 4r_W)}{(1 - x_W + r_W - r_{H^+})^2 + r_{H^+}\gamma_{H^+}} \cdot \sin^2(\beta - \alpha) \cdot (f_1 + \lambda_t f_2), \tag{33}$$

Here $\gamma_{H^+} = \left(\frac{M_{H^+}}{M_H}\right)^2$ and functions are entered

$$f_1 = (r_t ctg^2\beta + r_b tg^2\beta)(1 - x_W + r_W - r_t - r_b) - 4r_t r_b,$$
$$f_2 = \frac{1}{4}(r_t ctg^2\beta - r_b tg^2\beta)\left[x_b\sqrt{x_t^2 - 4r_t} - \frac{x_t}{\sqrt{x_t^2 - 4r_t}}(2(1 - x_t - x_b - r_W + r_t + r_b) + x_t x_b)\right]$$

If we neglect the antiquark mass m_b, then the decay width $H \to t + \bar{b} + W^-$ is greatly simplified ($\gamma_{H^+} = 0$):

$$\frac{d\Gamma(H \to t\bar{b}W^-)}{dx_t dx_b} = \frac{1}{2}\frac{d\Gamma_0(H \to t\bar{b}W^-)}{dx_t dx_b} \cdot (1 + \lambda_t P_t). \tag{34}$$

Here

$$\frac{d\Gamma_0(H \to t\bar{b}W^-)}{dx_t dx_b} = \frac{N_C G_F^2 m_t^2 M_H^3}{64\pi^3} \sin^2(\beta - \alpha) ctg^2\beta \cdot \frac{|U_{tb}|^2 (x_W^2 - 4r_W)}{(1 - x_W + r_W - r_{H^+})^2} [1 - x_W + r_W - r_t] \tag{35}$$

is the decay width of $H \to t + \bar{b} + W^-$ at the production of non-polarized quarks, and P_t is the degree of longitudinal polarization of the t -quark

$$P_t = \frac{x_b\sqrt{x_t^2 - 4r_t} - \frac{x_t}{\sqrt{x_t^2 - 4r_t}}(2(1 - x_t - x_b - r_W + r_t) + x_t x_b)}{4(1 - x_W + r_W - r_t)}. \tag{36}$$

For the decay width of the pseudoscalar boson in the $A \to H^{+*} + W^- \to t + \bar{b} + W^-$ channel, a similar expression is obtained

$$\frac{d\Gamma(A \to t\bar{b}W^-)}{dx_t dx_b} = \frac{1}{2}\frac{d\Gamma_0(A \to t\bar{b}W^-)}{dx_t dx_b} \cdot (1 + \lambda_t P_t), \tag{37}$$

where

$$\frac{d\Gamma_0(A \to t\bar{b}W^-)}{dx_t dx_b} = \frac{N_C G_F^2 m_t^2 M_A^3}{64\pi^3} ctg^2\beta \cdot \frac{|U_{tb}|^2 (x_W^2 - 4r_W)}{(1 - x_W + r_W - r_{H^+})^2} (1 - x_W + r_W - r_t), \tag{38}$$

and the degree of longitudinal polarization of P_t is expressed by the same formula (36) as in the decay of $H \to t + \bar{b} + W^-$.

Figure 9 shows the dependence of the degree of longitudinal polarization of the t -quark on the scaling energy x_t at $M_H(M_A) = 300$ GeV, $x_b = 0{,}3$, $m_t = 173{,}2$ GeV, $M_W = 80{,}425$ GeV. As follows from the figure, with an increase in the scaling energy of t -quark, the degree of its longitudinal polarization first decreases sharply and then slightly increases.

One of the possible Higgs boson decays is the $H \to W^{+*} + W^- \to t + \bar{b} + W^-$ decay, Feynman diagram, which is shown in fig. 1 (h). The matrix element of this decay is written as

$$M(H \to W^- W^{+*}) = ig_{WWH} \cdot \frac{g_W}{2\sqrt{2}} U_\mu^*(k) \cdot \left(-g_{\mu\nu} + \frac{q_\mu q_\nu}{M_W^2}\right) \cdot \frac{U_{tb}^*}{q^2 - M_W^2 + iM_W\Gamma_W} \cdot [\bar{u}(p_1, s_t)\gamma_\nu(1 + \gamma_5)\upsilon(p_2)] \tag{39}$$

The square of the matrix element (39) is expressed by the formula (with $r_b = 0$)

$$\left|M(H \to W^- W^{+*})\right|^2 = 8G_F^2 M_W^4 \frac{|U_{tb}|^2 \cos^2(\beta - \alpha)}{(1 - x_t - x_b)^2 + r_W\gamma_W} \cdot [F_1 + \lambda_t F_2] \tag{40}$$

Here, it is taken into account that $g_{WWH}^2 = 8G_F^2 M_W^4 \cos^2(\beta - \alpha)$ and functions are introduced

$$F_1 = (1 - x_W + r_W - r_t)\left[r_W + r_t\left(2 - \frac{1}{r_W} + \frac{x_W^2}{4r_W^2}\right)\right] + (1 - x_t + r_t - r_W)\left(1 - x_b + r_t - r_W - \frac{r_t}{r_W}x_W\right),$$

$$F_2=\frac{1}{2}\left[-r_W+r_t\left(2-\frac{1}{r_W}+\frac{x_W^2}{4r_W^2}\right)+\left(1-\frac{x_W}{2r_W}\right)(1-x_b-r_t-r_W)\right]f_3-$$
$$-\frac{1}{2}\left[1-x_t+r_t-r_W-\left(1-\frac{x_W}{2r_W}\right)(1-x_W+r_W-r_t)\right]f_4 \quad (41)$$
$$f_3=x_b\sqrt{x_t^2-4r_t}-\frac{x_t}{\sqrt{x_t^2-4r_t}}[2(1-x_t-x_b-r_W+r_t)+x_tx_b],$$
$$f_4=x_W\sqrt{x_t^2-4r_t}-\frac{x_t}{\sqrt{x_t^2-4r_t}}[2(1-x_t-x_W-r_W+r_t)+x_tx_W].$$

The decay width of the $H\to W^{+*}+W^-\to t+\bar{b}+W^-$ can be written as

$$\frac{d\Gamma(H\to t\bar{b}W^-)}{dx_t\,dx_b}=\frac{1}{2}\frac{d\Gamma_0(H\to t\bar{b}W^-)}{dx_t\,dx_b}\cdot(1+\lambda_tP_t), \quad (42)$$

in here

$$\frac{d\Gamma_0(H\to t\bar{b}W^-)}{dx_t\,dx_b}=\frac{N_CG_F^2M_W^4M_H}{64\pi^3}\cos^2(\beta-\alpha)\cdot\frac{|U_{tb}|^2}{(1-x_t+x_b)^2+r_W\gamma_W}\cdot F_1 \quad (43)$$

is the width of this decay with unpolarized particles, and

$$P_t=\frac{F_2}{F_1} \quad (44)$$

is the degree of longitudinal polarization of the t-quark.

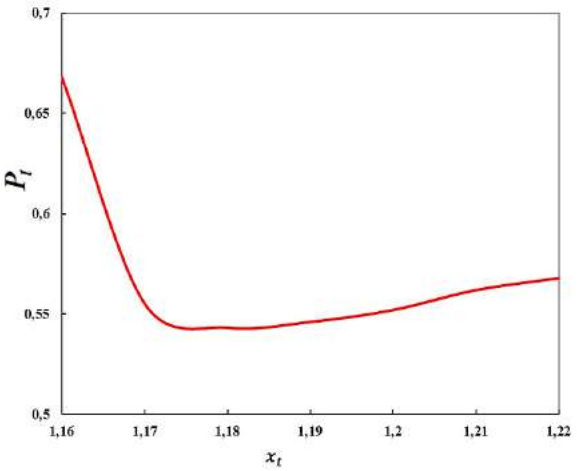

Fig.9. Dependence of the degree of longitudinal polarization of the t-quark on the scaling energy x_t.

CONCLUSION

In the framework of the MSSM, we discussed the decay channels of the supersymmetric Higgs bosons $H\to W^-+W^+$, $H\to Z^0+Z^0$, $A\to h+Z^0$, $H\to h+h$, $H\to h+b+\bar{b}$, $H\to Z^0+A+h$, $H^+\to h+W^\pm$, $A\to Z^0+h+h$, $H^\pm\to W^\pm+h+h$, $H(A)\to t+\bar{b}+W^-$. Analytical expressions for the amplitudes and decay widths are obtained, the dependence of the decay widths on the Higgs boson mass is studied. It was established that the width of all decays is highly sensitive to the Higgs boson mass. With an increase in the Higgs boson mass, the decay width in some processes increases, while in others it decreases.

[1] *S.Q. Abdullayev.* Standard Model, lepton and quark properties, "Zaka print", Baku, 2017, p.284.
[2] *S.Q. Abdullayev*. The general properties of fundamental interactions, "Zaka print", 2018, p. 332.
[3] *V.M. Yemelyanov*. Standard model and its extension, Mocsow, "Fizmatlit", 2007, p. 584.
[4] *A. Djouadi.* The Anatomy of Electro-Weak Symmetry Breaking. Tome I: The Higgs bosons in the Standard Model. arXiv: hep-ph/0503172v. 2, 3 May, 2005.

[5] ATLAS Collaboration. Phys. Letters, 2012, B 716, p. 1-29.
[6] CMS Collaboration. Phys. Letters, 2012, B 716, p. 30-60.
[7] *V.A. Rubakov*. The discovery of new particle with Higgs boson properties on Big Hadron Collider. UFN, 2012, vol.182, №10, pp.1017-1025.
[8] *A.V. Lanev*. CMS collaboration results. UFN, 2014, vol. 184, № 9, pp. 996-1004.
[9] *D.I. Kazakov*. Higgs boson is discovered. What's next? UFN, 2014, v. 184, № 9, pp.1004-1017.
[10] *E.E. Boos.* Standard Model and predictions for Higgs boson, UFN, 2014, vol. 184, № 9, pp.986-996.
[11] *P.W. Higgs.* Broken Symmetries and the Masses of gauge Bosons. Phys. Rev. Letters, 1964, v. 13, № 16, p. 508.
[12] *F. Englert, R. Brout*. Broken Symmetry and the mass of gauge vector Mesons. Phys. Rev. Letters, 1964, v. 13, № 9, p. 321.
[13] *S.K Abdullayev., M.Sh. Gojayev., F.A. Saddigh*. Moscow University Physics Bulletin, 2017, v.72, № 4. P. 329-339; published in Vestnik Moscovskoqo Universiteta, seriya 3: Physics, Astronomy, 2017, № 4, s.3-11.
[14] *S.K. Abdullayev, L.A. Agamaliyeva, M.Sh. Gocayev, F. Saddigh.* The investigation of Higgs boson creation in lepton-antilepton collisions. GESJ: Physics, 2015, № 1(13), pp.36-55.
[15] *S.K. Abdullayev, L.A. Agamaliyeva, M.Sh.Gocayev*. The investigation of Higgs boson creation in deep inelastic scattering. GESJ: Physics, 2015, №2(14), pp. 28-40.
[16] *R. Akbar, I. Ahmed, M.J. Aslam.* Lepton polarization asymmetries of $H \to \gamma\tau^+\tau^-$ decay in the Standard Model. Prog. Theor. Exp. Phys., 2014, p. 093B03.
[17] *F.T. Khalil-zade.* AJP Fizika, 2018, v. XXIV, № 1, p. 8-17.
[18] *S.K.Abdullayev, M.Sh.Gojayev, N.A. Nasibova, G.A. Soltanova*. AJP Fizika, 2018, v. XXIV, № 1, p. 32-39.
[19] *S.K.Abdullayev, M.Sh.Gojayev, N.A.Nasibova*. Russian Physics Journal, 2018, v. 61, № 1, p. 94-101.
[20] *J.F. Gunion, H.E. Haber.* The CP-conserving two-Higgs-doublet model: the approach to the decoupling limit. Phys. Rev. D, 2003, v. 67, p.075019.
[21] *G.C. Branco* et al. Phys. Rep., 2012, v.516, p.1.
[22] *H.E. Haber, G.L. Kane.* The search for supersymmetry: Probing physics beyond the standard model. Phys. Rep., 1985, v. 117, p.75.
[23] *D.I. Kazakov.* Beyond the Standard Model (in search of supersymmetry) hep-ph / 0012288.
[24] *D.I. Kazakov.* Supersymmetry on the Run: LHC and Dark Matter. Nucl. Phys. B Proc. Suppl.,2010,v.203-204,p.118;arXiv:1010.5419.
[25] *A. Djouadi.* The Anatomy of Electro-Weak Symmetry Breaking. Tome II: The Higgs in Minimal Supersymmetric Standard Model. arXiv: hep-ph/0503173v2, 2003.
[26] *K. Peters.* Prospects for beyond Standart Model Higgs Boson searches at future LHC runs and other machines. arXiv: 1701.05124v2 [hep-ex] 21, Feb. 20.
[27] *A. Djouadi. J. Kalinovski, P.M. Zerwas*. Two- and Three-Body Decay Modes of SUSY Higgs Particles. arXiv: hep-ph / 9511342V1, 16 Nov., 1995.
[28] *E. Barradas, J.L. Diaz-Cruz, A. Gutierrez, A. Rosado*. Three-body decays of Higgs bosons in the MSSM.
[29] *R.K. Barman* et. al. Current status of MSSM Higgs sector with LHC 13 TeV data. arXiv: 1608.02573v3 [hep-ph] 23 May, 2017.
[30] *S.K. Abdullayev, E.Sh. Omarova.* The decay of Higgs boson on fermion-anti-fermion couple. İzv. Vısşix Uçebnıx Zavedeniy, Fizika, 2018.
[31] *S.K. Abdullayev, E.Sh. Omarova.* The decay of Higgs boson on calibrating boson and fermion-anti-fermion couple. İzv. VUZ, Fizika, 2018.
[32] *S.K. Abdullayev, E.Sh. Omarova.* Decays of Supersymmetric Higgs bosons into fermions. AJP Fizika, 2018 (in press).

Received: 21.10.2019

HIGGS BOSON RADIATION IN ARBITRARILY POLARIZED ELECTRON-POSITRON COLLISIONS

M.Sh. GOJAYEV
23, acad. Z. Khalilov, Baku State University,
Baku, Azerbaijan, AZ1148
m_qocayev@mail.ru

Recently, the ATLAS and CMS collaborations at LHC announced Higgs boson like particle with mass around 125 GeV. To explore its physical properties, different observables are needed to be measured precisely at the various processes with the Higgs boson. In this paper in the framework of the Standard Model the Higgs boson and a heavy fermion pair production process in electron-positron collisions in considered: $e^-e^+ \to H f\bar{f}$, here $f\bar{f}$ – is the lepton pair ($\tau^-\tau^+$) or quark pair ($b\bar{b}$, $t\bar{t}$). The mechanism of Higgs boson radiation by a heavy fermion pair is investigated in detail. Taking into account the arbitrarily (longitudinal and transverse) polarizations of the electron-positron pair and the longitudinal polarizations of the fermion pair, analytical expressions for the differential and integral cross sections are obtained. The left-right and transverse spin asymmetries, as well as the degree of longitudinal polarizations of the fermion are determined. At the energy of the electron-positron pair $\sqrt{s}$ =1 TeV, the dependence of the effective cross section and asymmetries on the energies and angles of departure was studied. The possibility of measuring the coupling constant of the Higgs boson with a $t\bar{t}$-quark pair is discussed.

Keywords: Standard Model, Minimal Supersymmetric Standard Model, electron-positron pair, Higgs boson, decay width, coupling constant.
PACS: 12.15-y, 12.15 Mm, 14.70 Hp, 14.80 Bn.

1. INTRODUCTION

The Standard model (SM), based on the local gauge theory with a symmetry group $SU_C(3)\times SU_L(2)\times U_Y(1)$, satisfactorily describes the physics of strong, electromagnetic and weak interactions between quarks, leptons, and gauge bosons [1-5]. In elementary particle physics, not a single experiment has yet been observed, the results of which are not consistent with the SM. Recently opened the missing bricks in the building SM. These is the scalar Higgs boson, discoveries by the ATLAS and CMS collaborations [6, 7] (see also reviews [8-10]) at the Large Hadron Collider (LHC) at CERN. The discovery of the Higgs boson experimentally confirmed the theoretically predicted mechanism for the generation of masses of fundamental particles – the mechanism of spontaneous breaking of the Brout-Englert-Higgs symmetry [11–14].

In experiments conducted in the LHC, the main properties of this particle were established. The Higgs boson is a scalar particle with spin zero, positive parity, nonzero vacuum value, mass about 125 GeV, interacting with $W^{\pm}$- and Z^0-bosons with a coupling constant proportional to their masses. With the discovery of the Higgs boson H, the SM has entered a new stage in the study of the properties of the fundamental interactions of elementary particles. An accurate measurement of all the coupling constants of this particle with fundamental fermions can be an argument in favor of or a counterbalance to the fact that it is in fact a Higgs boson of the SM. In this connection, interest in various channels of the Higgs boson production and decay has greatly increased [1, 15–29].

Determining the physical characteristics of the Higgs boson H is the main task of the LHC, as well as future high-energy electron-positron colliders. Note that the collision of electrons and positrons at high energies is an effective method for studying the mechanisms of interaction of elementary particles. This is mainly due to the following two circumstances. First, the interaction of electrons and positrons is described by the electroweak Weinberg-Salam theory; therefore, the results obtained are well interpretable. Secondly, since electrons and positrons do not participate in strong interactions, the background conditions of the experiments are significantly improved compared with the studies conducted with hadron beams. The latter circumstance is especially significant when studying processes with small cross sections. We only note that experiments carried out with electron-positron beams at LEP and SLC acceleration centers up to energies of $\sqrt{s} = 209$ GeV in the center-of-mass system played an essential role for precision testing of the SM [1, 2].

At present, the construction of a new generation of electron-positron colliders ILC (International Linear Collider), CLIC (Compact Linear Collider), FCC-ee (Future Circular Collider), CEPC (Circular Electron Positron Collider) [23, 30] has been designed. In the future, these colliders will allow us to study the physical properties of the standard Higgs boson.

In recent works [16, 27], we have investigated the processes of production of the Higgs boson and light fermion pair in arbitrarily polarized electron-positron collisions. The associated production of the Higgs boson and the heavy fermion pair was first considered in [31]. Here authors consider the electromagnetic mechanism of the production of a heavy fermion pair and the Higgs boson radiation from the fermion line $e^- + e^+ \to (\gamma^*) \to f + \bar{f} + H$. In [32] (see also [33]), in the framework of the SM, the production of the Higgs

131, H. Javid ave., AZ-1143, Baku
ANAS, G.M. Abdullayev Institute of Physics
E-mail: jophphysics@gmail.com

boson H and a heavy $t\bar{t}$-quark pair was considered $e^- + e^+ \to (\gamma^*; Z^*) \to H + t + \bar{t}$. Here, a cross section is obtained, integrated over the angles of emission of particles and characterizing the distribution of the $t\bar{t}$-quark pair by energy. In a recent paper [34, 35], we investigated the electromagnetic mechanism of the process $e^- + e^+ \to (\gamma^*) \to H + f + \bar{f}$ with allowance for arbitrary polarizations of the electron-positron pair and the helicities of heavy fermions.

In the present work, we studied the associated production of the standard Higgs boson H and a heavy fermion pair in arbitrarily polarized electron-positron collisions in the framework of the SM:

$$e^- + e^+ \to (\gamma^*;\, Z^*) \to H + f + \bar{f} \qquad (1)$$

where $f\bar{f}$ –may be a lepton ($\tau^-\tau^+$) or quark ($b\bar{b}$, $t\bar{t}$) pair. The differential and integral cross sections of the process are calculated taking into account the polarizations of the particles. The possibility of measuring the fundamental constant of the SM, the Higgs boson coupling constant of with a heavy fermion pair, is discussed, which is very important for verifying the Higgs sector of the SM.

2. DIFFERENTIAL CROSS SECTION OF REACTION $e^-e^+ \to Hf\bar{f}$

In the SM process (1) is described by two types of Feynman diagrams, shown in fig. 1, where 4-momenta of the particles are written in parentheses. Diagrams a) and b) correspond to the Higgs boson radiation by a heavy fermion pair, and c) describes the Higgs boson radiation by the intermediate vector Z^0-boson.

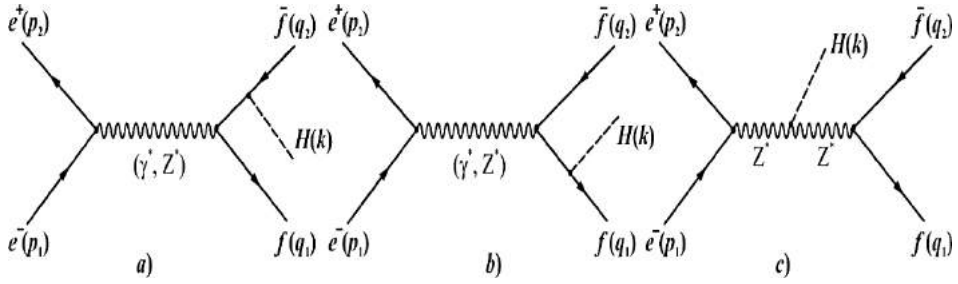

Fig. 1. Feynman diagrams for the associated production of Higgs boson with a fermion pair.

Within the framework of the SM, the matrix element corresponding to diagrams a) and b) can be written as (note that diagram c) was studied in detail in a recent paper [16], which is why it is not considered here)

$$M_{i\to f} = M^{(\gamma)}_{i\to f} + M^{(Z)}_{i\to f}, \qquad (2)$$

$$M^{(\gamma)}_{i\to f} = \frac{ie^2 Q_e Q_f}{s} g_{Hff} \cdot \ell^{(\gamma)}_{\mu} \cdot J^{(\gamma)}_{\mu}, \qquad (3)$$

$$M^{(Z)}_{i\to f} = \frac{ie^2}{s - M_Z^2} g_{Hff} \cdot \ell^{(Z)}_{\mu} \cdot J^{(Z)}_{\mu}. \qquad (4)$$

Here $Q_e = -1$ – is the electric charge of an electron in units e;

$$\ell^{(\gamma)}_{\mu} = \bar{\upsilon}_e(p_2)\gamma_\mu u_e(p_1),$$

$$J^{(\gamma)}_{\mu} = \bar{u}_f(q_1)\left[\frac{\hat{q}_1 + \hat{k} + m_f}{(q_1+k)^2 - m_f^2}\gamma_\mu - \gamma_\mu \frac{\hat{q}_2 + \hat{k} - m_f}{(q_2+k)^2 - m_f^2}\right]\upsilon_f(q_2), \qquad (5)$$

$$\left.\begin{aligned} \ell^{(Z)}_{\mu} &= \bar{\upsilon}_e(p_2)\gamma_\mu[g_V(e) + \gamma_5 g_A(e)]u_e(p_1), \\ J^{(Z)}_{\mu} &= \bar{u}_f(q_1)\left\{\frac{\hat{q}_1 + \hat{k} + m_f}{(q_1+k)^2 - m_f^2}\gamma_\mu[g_V(f) + \gamma_5 g_A(f)] - \gamma_\mu[g_V(f) + \right. \\ &\left. + \gamma_5 g_A(f)]\frac{\hat{q}_2 + \hat{k} - m_f}{(q_2+k)^2 - m_f^2}\right\}\upsilon_f(q_2), \end{aligned}\right\} \qquad (6)$$

– electromagnetic (weak) currents of the electron-

positron and heavy fermion pair; $s = p^2 = (p_1 + p_2)^2$ – the square of the total energy e^-e^+-pairs in the center of mass system, m_f and Q_f – the mass and electric charge of the fermion f, g_{Hff} – the Higgs boson coupling constant with a heavy fermion pair, M_Z – the mass of a Z^0-boson, $g_V(e)$ and $g_A(e)$ ($g_V(f)$ and $g_A(f)$) – the vector and axial-vector coupling constants of the electron (fermion) with Z^0-boson. In SM, these coupling constants are defined by the expressions

$$\left.\begin{aligned} g_V(e) &= \frac{-\frac{1}{2} + 2x_W}{2\sqrt{x_W(1-x_W)}}, \qquad g_A(e) = \frac{-\frac{1}{2}}{2\sqrt{x_W(1-x_W)}}, \\ g_V(f) &= \frac{I_3(f) - 2Q_f x_W}{2\sqrt{x_W(1-x_W)}}, \quad g_A(f) = \frac{I_3(f)}{2\sqrt{x_W(1-x_W)}}, \end{aligned}\right\} \tag{7}$$

where $x_W = \sin^2\theta_W$ – is the Weinberg parameter, $I_3(f) = \pm 1/2$ – is the third projection of the weak isospin of the fermion f.

The square of the matrix element (2) is expressed by the formula

$$\left|M_{i\to f}\right|^2 = \frac{e^4}{s^2} g_{Hff}^2 [Q_e^2 Q_f^2 L_{\mu\nu}^{(\gamma)} \cdot H_{\mu\nu}^{(\gamma)} + 2Q_e Q_f X_Z L_{\mu\nu}^{(i)} \cdot H_{\mu\nu}^{(i)} + X_Z^2 L_{\mu\nu}^{(Z)} \cdot H_{\mu\nu}^{(Z)}] \cdot \tag{8}$$

Here $X_Z = \left(1 - \frac{M_Z^2}{s}\right)^{-1}$, $L_{\mu\nu}^{(\gamma)}$ ($H_{\mu\nu}^{(\gamma)}$), $L_{\mu\nu}^{(Z)}$ ($H_{\mu\nu}^{(Z)}$) and $L_{\mu\nu}^{(i)}$ ($H_{\mu\nu}^{(i)}$) are the electromagnetic, weak, and interference tensors of the electron-positron (heavy fermion) pair. Due to the conservation of electron-positron currents $\ell_\mu^{(\gamma)}$ and $\ell_\mu^{(Z)}$, the contribution to the cross section is made only by the spatial components of the tensors

$$L_{\mu\nu}^{(a)} \cdot H_{\mu\nu}^{(a)} = L_{mr}^{(a)} \cdot H_{mr}^{(a)} \qquad (m, r = 1,2,3;\ a = \gamma, i, Z).$$

Electron-positron tensors $L_{mr}^{(a)}$ are easily calculated on the basis of currents $\ell_\mu^{(\gamma)}$ and $\ell_\mu^{(Z)}$, in the case of arbitrarily polarized e^-e^+-pairs, they have the following structure [36, 37]:

$$\begin{aligned} L_{mr}^{(\gamma)} &= \ell_m^{(\gamma)} \ell_r^{*(\gamma)} = \frac{s}{2}[(1-\lambda_1\lambda_2)(\delta_{mr} - N_m N_r) + (\lambda_2 - \lambda_1) i\varepsilon_{mrs} N_s + \\ &+ (\vec{\eta}_1\vec{\eta}_2)(\delta_{mr} - N_m N_r) - \eta_{1m}\eta_{2r} - \eta_{1r}\eta_{2m}], \\ L_{mr}^{(i)} &= \ell_m^{(\gamma)} \ell_r^{*(Z)} = g_V(e) L_{mr}^{(\gamma)} + \frac{s}{2} \cdot g_A(e)[(\lambda_2 - \lambda_1)(\delta_{mr} - N_m N_r) + (1 - \lambda_1\lambda_2) i\varepsilon_{mrs} N_s], \\ L_{mr}^{(Z)} &= \ell_m^{(Z)} \ell_r^{*(Z)} = [g_V^2(e) + g_A^2(e)] L_{mr}^{(\gamma)} + \frac{s}{2} \cdot 2 g_V(e) g_A(e)[(\lambda_2 - \lambda_1)(\delta_{mr} - N_m N_r) + \\ &+ (1 - \lambda_1\lambda_2) i\varepsilon_{mrs} N_s] - s \cdot g_A^2(e)[(\vec{\eta}_1\vec{\eta}_2)(\delta_{mr} - N_m N_r) - \eta_{1m}\eta_{2r} - \eta_{1r}\eta_{2m}], \end{aligned} \tag{9}$$

where λ_1 and λ_2 ($\vec{\eta}_1$ and $\vec{\eta}_2$) are the helicities (the transverse components of the spin vectors) of the electron and positron, $\vec{N}$ –is a unit vector directed along the electron momentum.

From the expressions of tensors (9), it follows that the longitudinally polarized electron and positron must have opposite helicities $\lambda_1 = -\lambda_2 = \pm 1$ (the left electron, and the right positron – $e_L^- e_R^+$ or the right electron, and the left positron – $e_R^- e_L^+$). This is due to the preservation of the total momentum in the transitions $e^- + e^+ \to \gamma^*$ and $e^- + e^+ \to Z^*$.

As for the fermionic tensors of a heavy fermion pair $H_{mr}^{(a)}$, we note that in the general case they have a cumbersome expressions, therefore they are not given here. However, at high energies of colliding particles ($\sqrt{s} \geq 1$ TeV), the rations m_f^2/s and M_H^2/s can be neglected (for example, when $\sqrt{s} = 1$ TeV for a heavy t-quark this ratio is $\left(\frac{173.2}{1000}\right)^2 = 0.03 << 1$). Then for the tensors $H_{mr}^{(a)}$ we have the following expressions (we assume that the heavy fermion pair is polarized longitudinally):

$$
\left.
\begin{aligned}
H_{mr}^{(\gamma)} &= J_m^{(\gamma)} J_r^{*(\gamma)} = \frac{x_H^2}{2(1-x_1)(1-x_2)}[(1+h_1h_2)(\delta_{mr}-n_m n_r)+(h_1+h_2)i\varepsilon_{mrq}n_q], \\
H_{mr}^{(i)} &= J_m^{(\gamma)} J_r^{*(Z)} = \\
&= g_V(f)H_{mr}^{(\gamma)} + \frac{1}{4}g_A(f)(1+h_1h_2)\cdot x_H \cdot i\varepsilon_{mrq}\left[\frac{x_2}{1-x_2}(n_{2q}-n_q)-\frac{x_1}{1-x_1}(n_{1q}-n_q)\right]+ \\
&+\frac{1}{4}g_A(f)(h_1+h_2)\left\{\frac{1}{1-x_2}\left[x_H x_2(n_m n_{2r}+n_r n_{2m})+2(1-x_1)\delta_{mr}\right]-\right. \\
&\left.-\frac{1}{1-x_1}\left[x_H x_1(n_m n_{1r}+n_r n_{1m})+2(1-x_2)\delta_{mr}\right]\right\}. \\
H_{mr}^{(Z)} &= J_m^{(Z)} J_r^{*(Z)} = [g_V^2(f)+g_A^2(f)]H_{mr}^{(\gamma)} - g_A^2(f)(1+h_1h_2)(1+x_H)(\delta_{mr}-n_m n_r)- \\
&-\frac{1}{2}\cdot g_A^2(f)(h_1+h_2)x_H i\varepsilon_{mrq}\left[\frac{x_2}{1-x_1}(n_{2q}-n_q)-\frac{x_1}{1-x_2}(n_{1q}-n_q)\right]+ \\
&+\frac{1}{2}g_V(f)g_A(f)(1+h_1h_2)x_H i\varepsilon_{mrq}\left[\frac{x_2}{1-x_2}(n_{2q}-n_q)-\frac{x_1}{1-x_1}(n_{1q}-n_q)\right]+ \\
&+\frac{1}{2}g_V(f)g_A(f)(h_1+h_2)\left\{\frac{1}{1-x_2}[x_H x_2(n_m n_{2r}+n_r n_{2m})+2(1-x_1)\delta_{mr}]-\right. \\
&\left.-\frac{1}{1-x_1}[x_H x_1(n_m n_{1r}+n_r n_{1m})+2(1-x_2)\delta_{mr}]\right\}.
\end{aligned}
\right\} \qquad (10)
$$

Here h_1 and h_2 – are the helicities of the fermion and antifermion, $x_1 = 2E_1/\sqrt{s}$, $x_2 = 2E_2/\sqrt{s}$ and $x_H = 2E_H/\sqrt{s} = 2 - x_1 - x_2$ – are the scaling energies of the fermion, antifermion and Higgs boson, respectively, $\vec{n}$, $\vec{n}_1$ and $\vec{n}_2$ – are the unit vectors along the Higgs boson, fermion and antifermion momentums.

As follows from the tensors $H_{mr}^{(a)}$, the helicity of the fermion and the antifermion, in contrast to the helicity of the electron-positron pair, must be the same $h_1 = h_2 = \pm 1$ ($f_R\bar{f}_R$ or $f_L\bar{f}_L$).

This is due to the conservation of the total momentum at the Higgs boson emission by the fermion or antifermion ($f \to f + H$, $\bar{f} \to \bar{f} + H$). We note that when the Higgs boson is emitted by the vector Z-boson, due to the conservation of the total momentum in the transition $Z^* \to f + \bar{f}$, the fermion and the antifermion must have opposite helicities ($h_1 = -h_2 = \pm 1$, $f_L\bar{f}_R$ and $f_R\bar{f}_L$). Consequently, it is possible to separate the contributions of the diagrams a) and b) from the contribution of the diagram c) along the helicities of the fermion and the antifermion.

We use a coordinate system in which the OXZ plane coincides with the particle production plane $\vec{q}_1 + \vec{q}_2 + \vec{k} = 0$, and we introduce angles θ, χ and φ, where θ – is the polar angle between the Z axis and the direction of the electron beam, χ – is the azimuth angle between the production plane and the plane defined by the Z axis and the electron beam, φ – the azimuth angle between the planes of production and transverse polarization of the electron. In this coordinate system, the angular distribution of particles over the angles φ, θ and χ in the case of arbitrarily polarized electron-positron and longitudinally polarized fermion-antifermion pairs is given by:

$$
\frac{d^5\sigma}{d\varphi d\chi d(\cos\theta)dx_1dx_2} = \frac{\alpha_{\mathrm{QED}}^2 N_C}{256\pi^3 s^2} g_{Hff}^2 [Q_e^2 Q_f^2 L_{mr}^{(\gamma)} \cdot H_{mr}^{(\gamma)} + 2Q_e Q_f X_Z L_{mr}^{(i)} \cdot H_{mr}^{(i)} + X_Z^2 L_{mr}^{(Z)} \cdot H_{mr}^{(Z)}], \qquad (11)
$$

where N_C – is the color factor (in the case of the production of a lepton pair $\tau^-\tau^+$ $N_C = 1$, and in the case of the production of a quark pair $b\bar{b}$ or $t\bar{t}$ $N_C = 3$).

3. ANGULAR CORRELATIONS IN THE PROCESS $e^-e^+ \to Hf\bar{f}$

We introduce the so-called correlation functions $\sigma_n\,(n = 1 \div 9)$, by means of the relations

$$\left.\begin{aligned}
&\sigma_1 = H_{11} + H_{22}, \qquad \sigma_2 = \frac{1}{2}(H_{22} - H_{11}), \quad \sigma_3 = H_{33},\\
&\sigma_4 = \frac{1}{2}(H_{13} + H_{31}), \quad \sigma_5 = \frac{1}{2}(H_{23} + H_{32}), \quad \sigma_6 = \frac{1}{2}(H_{12} + H_{21}),\\
&\sigma_7 = i(H_{12} - H_{21}), \qquad \sigma_8 = \frac{i}{2}(H_{23} - H_{32}), \quad \sigma_9 = \frac{i}{2}(H_{31} - H_{13}).
\end{aligned}\right\} \tag{12}$$

Then the product of the electron-positron and fermionic tensors can be represented as:

$$L_{mr} \cdot H_{mr} = \frac{1}{2}(L_{11} + L_{22}) \cdot \sigma_1 + (L_{22} - L_{11}) \cdot \sigma_2 + L_{33} \cdot \sigma_3 + (L_{13} + L_{31}) \cdot \sigma_4 + (L_{23} +$$

$$+ L_{32}) \cdot \sigma_5 + (L_{12} + L_{21}) \cdot \sigma_6 - \frac{i}{2}(L_{12} - L_{21}) \cdot \sigma_7 - i(L_{23} - L_{32}) \cdot \sigma_8 - i(L_{31} - L_{31}) \cdot \sigma_9. \tag{13}$$

For the distribution of particles over the angles θ and χ in the reaction (1) the expression is obtained

$$\frac{d^4\sigma}{d\chi d(\cos\theta) dx_1 dx_2} = \frac{\alpha_{\text{QED}}^2 N_C}{128\pi^2 s} g_{Hff}^2 [G_A \cdot \sigma_A + G_B \cdot \sigma_B + G_C \cdot \sigma_C]. \tag{14}$$

The notation is entered here

$$\left.\begin{aligned}
&G_A = Q_e^2 Q_f^2 + 2Q_e Q_f g_V(e) g_V(f) X_Z + [g_V^2(e) + g_A^2(e)][g_V^2(f) + g_A^2(f)] X_Z^2,\\
&G_B = 2g_A(e) g_A(f)[Q_e Q_f + 2g_V(e) g_V(f) X_Z] X_Z,\\
&G_C = [g_V^2(e) + g_A^2(e)] g_A^2(f) X_Z^2
\end{aligned}\right\} \tag{15}$$

and functions

$$\left.\begin{aligned}
&\sigma_A = \frac{1}{2}(1 + \cos^2\theta) \cdot \sigma_1 + \sin^2\theta(\cos 2\chi \cdot \sigma_2 + \sigma_3 + \sin 2\chi \cdot \sigma_4) + \sin 2\theta(\sin\chi \cdot \sigma_5 + \cos\chi \cdot \sigma_6),\\
&\sigma_B = \cos\theta \cdot \sigma_7 + 2\sin\theta(\cos\chi \cdot \sigma_8 + \sin\chi \cdot \sigma_9),\\
&\sigma_C = \frac{1}{2}(1 + \cos^2\theta) \cdot \sigma_1' + \sin^2\theta(\cos 2\chi \cdot \sigma_2' + \sigma_3' + \sin 2\chi \cdot \sigma_4') + + \sin 2\theta(\sin\chi \cdot \sigma_5' + \cos\chi \cdot \sigma_6').
\end{aligned}\right\} \tag{16}$$

Correlation functions σ_n and σ_n', entering in (16), depend on scaling energies x_1 and x_2 ($x_H = 2 - x_1 - x_2$) and they are easily determined on the basis of fermionic tensors (10):

$$\left.\begin{aligned}
&\sigma_1 = \frac{2x_H^2}{(1-x_1)(1-x_2)}(2 - n_x^2), && \sigma_2 = \frac{x_H^2}{(1-x_1)(1-x_2)} n_x^2,\\
&\sigma_3 = \frac{2x_H^2}{(1-x_1)(1-x_2)}(1 - n_z^2), && \sigma_4 = -\frac{2x_H^2}{(1-x_1)(1-x_2)} \cdot n_x n_z,\\
&\sigma_7 = 2x_H\left[\frac{x_2}{1-x_2}(n_z - n_{2z}) - \frac{x_1}{1-x_1}(n_z - n_{1z})\right], && \sigma_8 = x_H\left[\frac{x_2}{1-x_2}(n_x - n_{2x}) - \frac{x_1}{1-x_1}(n_x - n_{1x})\right],\\
&\sigma_5 = \sigma_6 = \sigma_9 = 0, && \sigma_1' = -4(1 + x_H)(2 - n_x^2), \quad \sigma_2' = -2(1 + x_H) n_x^2,\\
&\sigma_5' = \sigma_6' = 0. && \sigma_3' = -4(1 + x_H)(1 - n_z^2), \quad \sigma_4' = 4(1 + x_H) n_x n_z.
\end{aligned}\right\} \tag{17}$$

As can be seen, due to the orthogonality of the Y axis to the particle production plane, the correlation functions σ_5, σ_6, σ_9, σ_5' and σ_6' vanish.

In the case of massless fermions and Higgs boson, the distribution of particles in the Dalitz diagram is determined by the laws of conservation of energy and momentum:

$$x_1 + x_2 + x_H = 2, \qquad x_1\vec{n}_1 + x_2\vec{n}_2 + x_H\vec{n} = 0.$$

The boundaries of the allowed region are given by the equations

$$x_k = \left| x_i \pm x_j \right| \quad (i \neq j \neq k).$$

The lines $x_1 = x_2$, $x_1 = x_H$ and $x_2 = x_H$ divide the Dalitz diagram into six different areas. In the region of $(i;\ j)$ the scaling energies of the particles x_i and x_j satisfy the conditions

$$x_i \geq x_j \geq x_k \quad (i \neq j \neq k).$$

We can direct the axis Z along the most energetic particle and choose an axis X so that the x projection of the momentum of the second more energetic particle becomes positive. Then the following areas of the Dalitz diagram are obtained.

Ia (3; 1). The axis Z is directed along the momentum of the more energetic Higgs boson, and the momentum of the second energetic fermion has a positive x-projection (see fig. 2a)

$$\vec{n} = (0,\ 0,\ 1), \quad \vec{n}_1 = (s_{31},\ 0,\ c_{31}), \quad \vec{n}_2 = (-s_{32},\ 0,\ c_{32}).$$

Similarly, we have the following areas:

Ib(3; 2): $\vec{n}=(0,\,0,\,1),\ \vec{n}_1=(-s_{31},\,0,\,c_{31}),\ \vec{n}_2=(s_{32},\,0,\,c_{32});$
IIa(1; 2): $\vec{n}_1=(0,\,0,\,1),\ \vec{n}_2=(s_{12},\,0,\,c_{12}),\ \vec{n}=(-s_{13},\,0,\,c_{13});$
IIb(1; 3): $\vec{n}_1=(0,\,0,\,1),\ \vec{n}_2=(-s_{12},\,0,\,c_{12}),\ \vec{n}=(s_{13},\,0,\,c_{13});$
IIIa(2; 1): $\vec{n}_2=(0,\,0,\,1),\ \vec{n}_1=(s_{21},\,0,\,c_{21}),\ \vec{n}=(-s_{23},\,0,\,c_{23});$
IIIb(2; 3): $\vec{n}_2=(0,\,0,\,1),\ \vec{n}_1=(-s_{21},\,0,\,c_{21}),\ \vec{n}=(s_{23},\,0,\,c_{23}).$

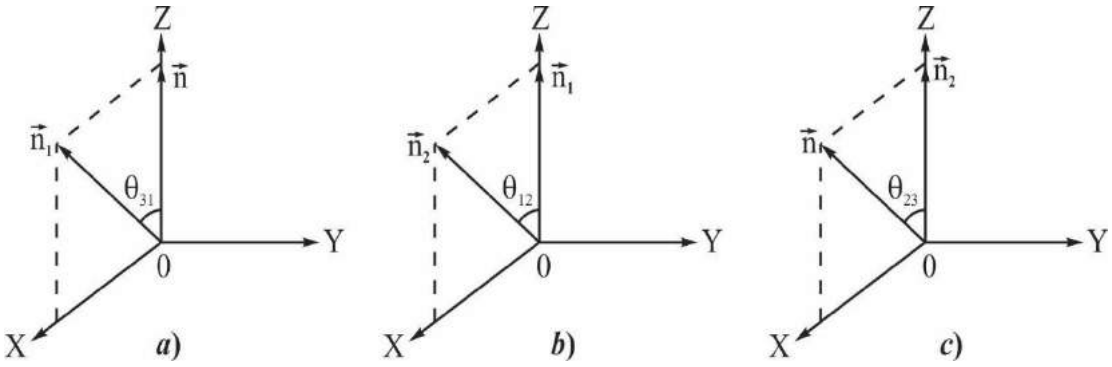

Fig. 2. The coordinate systems Ia, IIa and IIIb.

Here we have used the notation $s_{ij}=\sin\theta_{ij}$ and $c_{ij}=\cos\theta_{ij}$, where θ_{ij} – the angle between the directions of the momenta of the particles i and j. These angles depend on the scaling energies of the particles

$$\left.\begin{aligned}\sin\theta_{ij}&=\frac{2\sqrt{(1-x_1)(1-x_2)(1-x_H)}}{x_i x_j},\\ \cos\theta_{ij}&=1-\frac{2(x_i+x_j-1)}{x_i x_j}.\end{aligned}\right\}\qquad(18)$$

Using these expressions, we can easily determine the correlation functions in each area of the Dalitz diagram. Here we present the correlation functions in the coordinate system Ia (Ib), where the momentum of the more energetic Higgs boson is directed along the axis Z, and the second energetic fermion (antifermion) in the production plane has a positive momentum projection $q_{1x}>0$ ($q_{2x}>0$):

$$\left.\begin{aligned}&\sigma_1=\frac{4x_H^2}{(1-x_1)(1-x_2)}=4\left(2+\frac{1-x_1}{1-x_2}+\frac{1-x_2}{1-x_1}\right),\\ &\sigma_7=2x_H\left[\frac{x_2}{1-x_2}(1-c_{32})-\frac{x_1}{1-x_1}(1-c_{31})\right],\\ &\sigma_1'=-8(1+x_H),\ \sigma_2=\sigma_3=\sigma_4=\sigma_8=\sigma_2'=\sigma_3'=\sigma_4'=0.\end{aligned}\right\}\qquad(19)$$

The expressions for the correlation functions in the coordinate systems IIa, b and IIIa, b are given in the Appendix.

The distribution of particles over the angles θ and χ present in the form:

$$\frac{d^4\sigma}{d\chi d(\cos\theta)dx_1dx_2}=\frac{\alpha_{\rm QED}^2N_C}{128\pi^2 s}g_{Hff}^2G_A(\sigma_1+2\sigma_3)(1+\alpha_0)[1+\alpha_1\cos^2\theta+$$
$$+\alpha_2\sin^2\theta\cos2\chi+\alpha_4\sin^2\theta\sin2\chi+\alpha_7\cos\theta+\alpha_8\sin\theta\cos\chi],\qquad(20)$$

where the coefficients of the angular distributions of particles are determined by the expressions

$$\left.\begin{aligned}&\alpha_0=\frac{G_C}{G_A}\cdot\frac{\sigma_1'+2\sigma_3'}{\sigma_1+2\sigma_3},\qquad \alpha_1=\frac{1}{1+\alpha_0}\cdot\left[\frac{\sigma_1-2\sigma_3}{\sigma_1+2\sigma_3}+\frac{G_C}{G_A}\cdot\frac{\sigma_1'-2\sigma_3'}{\sigma_1+2\sigma_3}\right],\\ &\alpha_2=\frac{1}{1+\alpha_0}\cdot\left[\frac{2\sigma_2}{\sigma_1+2\sigma_3}+\frac{G_C}{G_A}\cdot\frac{2\sigma_2'}{\sigma_1+2\sigma_3}\right],\quad \alpha_4=\frac{1}{1+\alpha_0}\cdot\left[\frac{2\sigma_4}{\sigma_1+2\sigma_3}+\frac{G_C}{G_A}\cdot\frac{2\sigma_4'}{\sigma_1+2\sigma_3}\right],\\ &\alpha_7=\frac{1}{1+\alpha_0}\cdot\frac{G_B}{G_A}\cdot\frac{2\sigma_7}{\sigma_1+2\sigma_3},\qquad \alpha_8=\frac{1}{1+\alpha_0}\cdot\frac{G_B}{G_A}\cdot\frac{4\sigma_8}{\sigma_1+2\sigma_3}.\end{aligned}\right\}\qquad(21)$$

Let us estimate the coefficients of the angular distributions α_k $(k = 1, 2, 4, 7, 8)$ in the coordinate system IIIb, where the momentum of the more energetic antifermion is directed along the axis Z, and the momentum of the second energetic Higgs boson in the production plane has a positive x-projection $k_x > 0$ (see fig. 2c). Using the expressions of the correlation functions given in the Appendix, for these coefficients we have the expressions:

$$\alpha_0 = -\frac{G_C}{G_A}\cdot\frac{2}{x_H^2}(1+x_H)(1-x_1)(1-x_2), \quad \alpha_1 = \frac{3c_{23}^2-1}{3-c_{23}^2}\cdot\frac{1-\alpha_0}{1+\alpha_0},$$

$$\alpha_2 = \frac{s_{23}^2}{3-c_{23}^2}\cdot\frac{1-\alpha_0}{1+\alpha_0}, \qquad \alpha_4 = -\frac{2s_{23}c_{23}}{3-c_{23}^2}\cdot\frac{1-\alpha_0}{1+\alpha_0},$$

$$\alpha_7 = \frac{G_B}{G_A}\frac{1}{1+\alpha_0}\frac{2[x_2(1-x_1)(c_{23}-1)-x_1(1-x_2)(c_{23}-c_{21})]}{x_H(3-c_{23}^2)}, \tag{22}$$

$$\alpha_8 = \frac{G_B}{G_A}\frac{1}{1+\alpha_0}\frac{2[x_2(1-x_1)s_{23}-x_1(1-x_2)(s_{23}+s_{21})]}{x_H(3-c_{23}^2)}.$$

In fig. 3 shows the dependence of the coefficients on a variable x_2 with a fixed scaling energy $x_1 = 0.9$ in the process $e^- + e^+ \to H + t + \bar{t}$. Here and in further calculations, the energy of electron-positron beams is assumed $\sqrt{s}$ = 1 TeV, mass of Z^0-boson M_Z = 91.1875 GeV, mass of t-quark m_t = 173.2 GeV, Weinberg parameter x_W = 0.232. As you can see, the coefficient α_1 (α_7, α_8) is negative and decreases (increases) with increasing energy x_2. The coefficient of the angular distribution α_2 is positive and slowly increase with increasing variable x_2. The angular distribution coefficient α_4 at the beginning of the energy spectrum is negative, it increases with increasing x_2 and at the end of the energy spectrum becomes positive.

4. LEFT-RIGHT AND TRANSVERSE SPIN ASYMMETRIES AND THE DEGREE OF LONGITUDINAL POLARIZATION OF THE FERMION

When electron-positron pair a longitudinally polarized the differential cross section of reaction (1), integrated over the angles θ and χ, can be represented as:

$$\frac{d^2\sigma(\lambda_1,\lambda_2)}{dx_1dx_2} = \frac{d^2\sigma_0}{dx_1dx_2}[1-\lambda_1\lambda_2-(\lambda_1-\lambda_2)A_{LR}]. \tag{23}$$

Here

$$\frac{d^2\sigma_0}{dx_1dx_2} = \frac{\alpha_{\text{QED}}^2 N_C}{12\pi s}g_{Hff}^2\left\{G_A\frac{x_H^2}{(1-x_1)(1-x_2)} - 2[g_V^2(e)+g_A^2(e)]g_A^2(f)(1+x_H)X_Z^2\right\} \tag{24}$$

– the differential cross section of this process in the case of unpolarized particles, and

$$A_{LR} = \frac{G_D x_H^2 - 4g_V(e)g_A(e)\,g_A^2(f)(1+x_H)(1-x_1)(1-x_2)X_Z^2}{G_D x_H^2 - 2[g_V^2(e)+g_A^2(e)]\,g_A^2(f)(1+x_H)(1-x_1)(1-x_2)X_Z^2} \tag{25}$$

– left-right spin asymmetry due to the longitudinal polarization of the electron and the designation introduced

$$G_D = 2Q_eQ_f\,g_A(e)g_V(f)X_Z + 2g_V(e)g_A(e)[g_V^2(f)+g_A^2(f)]X_Z^2 \ .$$

The left-right spin asymmetry A_{LR} in the process $e^- + e^+ \to H + t + \bar{t}$ at $x_2 = 0.95$ approximately 17.6% and slightly increases with growth x_1, remaining almost constant. The same character is the left-right spin asymmetry in the process $e^- + e^+ \to H + \tau^- + \tau^+$. However, in this process, the left-right spin asymmetry is almost three times less than in the process $e^- + e^+ \to H + t + \bar{t}$.

Due to the weak interaction in the process under consideration, fermion and antifermion can be produced longitudinally polarized. Taking into account the longitudinal polarizations of the heavy fermion pair, the differential cross section integrated over the angles is:

$$\frac{d^2\sigma(h_1,h_2)}{dx_1dx_2}=\frac{1}{4}\cdot\frac{d^2\sigma_0}{dx_1dx_2}[1+h_1h_2+(h_1+h_2)P_f]. \quad (26)$$

Here

$$P_f=\{Q_eQ_fg_V(e)g_A(e)X_Z+[g_V^2(e)+g_A^2(e)]\,g_V(f)g_A(f)X_Z^2\}\times$$

$$\times\{(1-x_1)[x_Hx_2c_{23}+3(1-x_1)]-(1-x_2)[x_Hx_1(c_{23}c_{21}-s_{23}s_{21})+3(1-x_2)]\}\times. \quad (27)$$

$$\times\{G_Ax_H^2-2(1-x_1)(1-x_2)[g_V^2(e)+g_A^2(e)]\,g_A^2(f)(1+x_H)X_Z^2\}^{-1}$$

– degree of longitudinal polarization of the fermion or antifermion in the coordinate system IIIb.

In fig. 4 shows the dependence of the degree of longitudinal polarization t-quark in the process $e^-+e^+\to H+t+\bar{t}$ on the variable x_1 at a fixed scaling energy $x_2=0.9$ and $x_2=0.95$. From the graphs it follows, that with increasing scaling energy x_1 the degree of longitudinal polarization decreases monotically. However, at a fixed quark energy x_1 with an increase in the antiquark energy x_2, the magnitude of the degree of longitudinal polarization increases.

Interestingly, the degree of longitudinal polarization of the fermion $P_f(x_1,x_2)$ changes its sign when replacing $x_1\leftrightarrow x_2$: $P_f(x_1,x_2)=-P_f(x_2,x_1)$.

Note that the degree of longitudinal polarization t-quark has already been measured by the ATLAS detector in the process of hadron production of a pair $t\bar{t}$ at the Large Hadron Collider [38].

Now consider the particle distribution over the angles θ and φ. In this case, the annihilation cross section of a transversely polarized electron-positron pair, integrated over the azimuth angle χ, has the form

$$\frac{d^4\sigma(\eta_1,\eta_2)}{d\varphi d(\cos\theta)dx_1dx_2}=\frac{d^4\sigma_0}{d\varphi d(\cos\theta)dx_1dx_2}[1+A_\perp\eta_1\eta_2\cos 2\varphi], \quad (28)$$

where

$$\frac{d^4\sigma_0}{d\varphi d(\cos\theta)dx_1dx_2}=\frac{\alpha_{\mathrm{QED}}^2N_C}{128\pi^2s}g_{Hff}^2G_A(\sigma_1+2\sigma_3)(1+\alpha_0)(1+\alpha_1\cos^2\theta) \quad (29)$$

– differential cross section of this process in the case of unpolarized particles,

$$A_\perp=\frac{\beta_1\sin^2\theta}{1+\beta_1\cos^2\theta}\cdot\frac{F_B}{F_A} \quad (30)$$

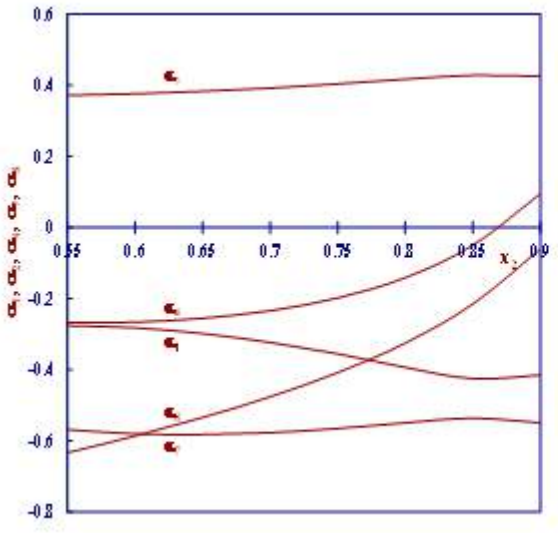

Fig. 3. Dependence of the angular distribution coefficients on the energy x_2 in the reaction $e^-e^+\to Ht\bar{t}$ for $x_1=0.9$, $\sqrt{s}$ = 1 TeV, M_Z = 91.1875 GeV, m_t = 173.2 GeV.

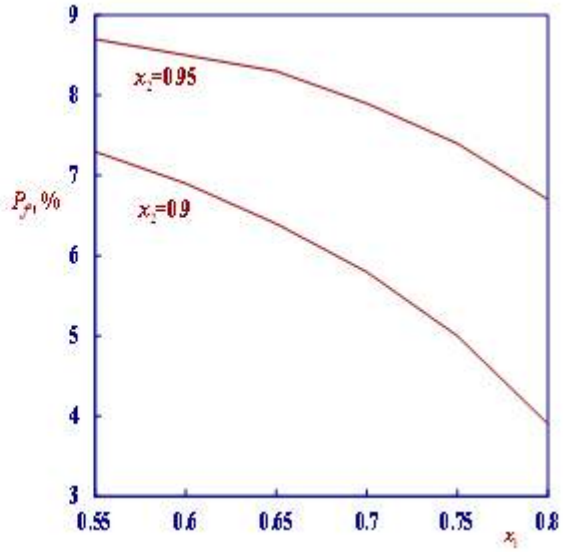

Fig. 4. The degree of longitudinal polarization in the process $e^-e^+\to Ht\bar{t}$ as a function of the energy x_1 for different x_2.

– transverse spin asymmetry due to transverse polarizations of the electron-positron pair. The notation is entered here

$$\beta_1 = \frac{\sigma_1 - 2\sigma_3}{\sigma_1 + 2\sigma_3},$$

$$F_A = G_A \frac{x_H^2}{2(1-x_1)(1-x_2)} - [g_V^2(e) + g_A^2(e)] g_A^2(f)(1+x_H) X_Z^2, \tag{31}$$

$$F_B = \frac{x_H^2}{2(1-x_1)(1-x_2)} \{Q_e^2 Q_f^2 + 2Q_e Q_f X_Z g_V(e) g_V(f) + X_Z^2 [g_V^2(e) - g_A^2(e)] \times$$
$$\times [g_V^2(f) + g_A^2(f)]\} - X_Z^2 [g_V^2(e) - g_A^2(e)] g_A^2(f)(1+x_H),$$

In fig. 5 shows the angular dependence of the transverse spin asymmetry (30) in the process $e^- + e^+ \to H + t + \bar{t}$ at $x_1 = 0.95$ and in the three values of the variable $x_2 = 0.55$, 0.6, and 0.65. As the angle θ increases, the transverse spin asymmetry increases and reaches a maximum at an angle of $\theta = 90°$, and then the asymmetry decreases and vanishes at the end of the angular spectrum. The growth of the variable x_2 leads to a decrease in the transverse spin asymmetry.

5. THE DISTRIBUTION OF PARTICLES IN A VARIABLE T

Dalitz distribution density on variable x_1 and x_2 has a simple and compact form, which coincides with the result of [32]

$$\frac{d^2\sigma_0}{dx_1 dx_2} = \frac{\alpha_{\text{QED}}^2 N_C}{12\pi s} g_{Hff}^2 \left\{ G_A \left[2 + \frac{1-x_1}{1-x_2} + \frac{1-x_2}{1-x_1} \right] - 2[g_V^2(e) + g_A^2(e)] g_A^2(f)(1+x_H) X_Z^2 \right\} \tag{32}$$

In fig. 6 shows the dependence of the cross section (32) in the process $e^- + e^+ \to H + t + \bar{t}$ on the variable x_2 with fixed $x_1 = 0.9$ and $x_1 = 0.95$ .With increasing scaling energy x_2, the cross section monotonously decreases, and a decrease in the variable x_1 also leads to a decrease in the cross section.

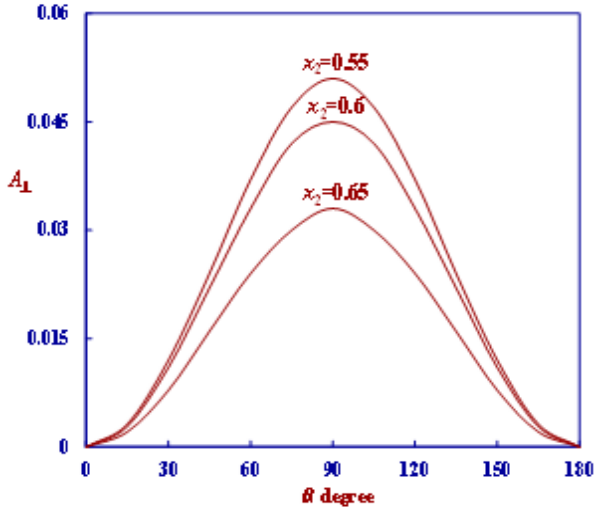

Fig. 5. The transverse spin asymmetry in the process $e^- e^+ \to Ht\bar{t}$ as a function of the angle θ at $x_1 = 0.95$ for different x_2.

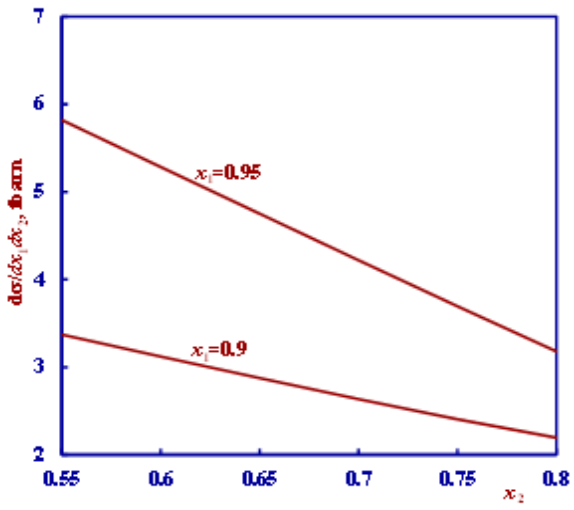

Fig. 6. Dependence of the cross section of the process $e^- e^+ \to Ht\bar{t}$ on the energy x_2 for different x_1 and $\sqrt{s}$ = 1 TeV, M_Z = 91.1875 GeV, m_t = 173.2 GeV.

We introduce new variables $T = T_1 = \max(x_1, x_2, x_H)$, T_2 and T_3 so that inequalities $T = T_1 \geq T_2 \geq T_3 = 2 - T - T_2$ are satisfied. We direct the axis Z along the momentum of the most energetic particle and integrate the section in a variable T_2 with a fixed T one. Then we get the following results:

1) at $x_H = T$ and $x_1 = T_2$ (or $x_2 = T_2$)

$$\frac{d\sigma}{dT} = \frac{\alpha_{\text{QED}}^2 N_C}{12\pi s} g_{Hff}^2 \times \left\{ G_A T \ln\left(\frac{1-T}{T}\right) - \frac{1}{4}[g_V^2(e) + g_A^2(e)] g_A^2(f)(1+x_H) X_Z^2 (12 - 5T)(3T - 2) \right\} \quad ; \tag{33}$$

2) at $x_1 = T$ and $x_2 = T_2$ (or at $x_2 = T$ and $x_1 = T_2$):

$$\frac{d\sigma}{dT} = \frac{\alpha_{\text{QED}}^2 N_C}{12\pi s} g_{Hff}^2 \left\{ G_A \left[\frac{(3T-2)(6-5T)}{2(1-T)} - (1-T)\ln\left(\frac{2T-1}{1-T}\right) \right] - \right.$$
$$\left. - \frac{1}{4}[g_V^2(e) + g_A^2(e)] g_A^2(f) X_Z^2 (12-5T)(3T-2) \right\}; \quad (34)$$

3) at $x_1 = T$ and $x_H = T_2$ (or at $x_2 = T$ and $x_H = T_2$)

$$\frac{d\sigma}{dT} = \frac{\alpha_{\text{QED}}^2 N_C}{12\pi s} g_{Hff}^2 \left\{ G_A \left[\frac{(3T-2)(2-T)}{2(1-T)} + (1-T)\ln\left(\frac{2T-1}{1-T}\right) \right] - \right.$$
$$\left. - \frac{1}{4}[g_V^2(e) + g_A^2(e)] g_A^2(f) X_Z^2 (12-5T)(3T-2) \right\}. \quad (35)$$

By adding the contributions to the cross section of individual regions of the Dalitz diagram, we obtain the cross section characterizing the distribution of the most energetic particle in a variable T:

$$\frac{d\sigma}{dT} = \frac{\alpha_{\text{QED}}^2 N_C}{12\pi s} g_{Hff}^2 \left\{ G_A \left[\frac{(3T-2)(4-3T)}{(1-T)} + T\ln\left(\frac{1-T}{T}\right) \right] - \right.$$
$$\left. - \frac{3}{4}[g_V^2(e) + g_A^2(e)] g_A^2(f) X_Z^2 (12-5T)(3T-2) \right\}. \quad (36)$$

In fig. 7 illustrates the dependence of the cross section of the reaction $e^- + e^+ \to H + t + \bar{t}$ on the variable T for $\sqrt{s} = 1$ TeV and $m_t = 173.2$ GeV. Growth of the variable T from 0.725 to 0.9 leads to a monotonic increase in the cross section from 0.252 fbarn to 4.529 fbarn.

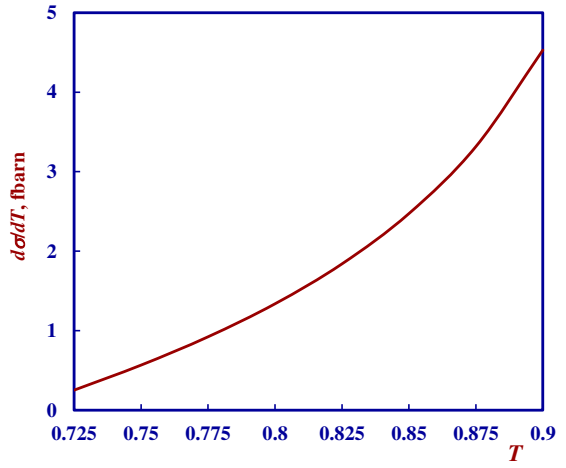

Fig. 7. Dependence of the cross section of the process $e^- e^+ \to Ht\bar{t}$ on the variable T for the $\sqrt{s}$ = 1 TeV, M_Z = 91.1875 GeV, m_t = 173.2 GeV.

Note that an experimental study of the reaction $e^- + e^+ \to H + t + \bar{t}$ is of great interest, since it allows you to accurately measure the coupling constant g_{Htt}. Although the Higgs boson coupling constants with gauge bosons g_{HWW}, g_{HZZ} are measurable in the LHC, the direct measurement of the constant g_{Htt} is difficult. Consequently, the study of the Higgs boson radiation process by top quarks in high-energy electron-positron collisions represents a certain interest.

CONCLUSION

Thus, we discussed the process of the associated production of the Higgs boson H and a longitudinally polarized heavy fermion pair in the annihilation of an arbitrarily polarized electron-positron pair $e^- + e^+ \to (\gamma^*; Z^*) \to H + f + \bar{f}$. An analytical expression of the differential cross section of the process is obtained, the features of the cross section behavior, angular correlations of particles, left-right spin asymmetry A_{LR}, the degree of longitudinal polarization of the fermion P_f, and transverse spin asymmetry $A_\perp$ are investigated. The results of the calculations are illustrated with graphs. The possibility of experimental measurement of the coupling constant g_{Htt} is discussed.

APPENDIX

Here we give the expressions for the correlation functions in the coordinate systems IIa, IIb, IIIa and IIIb.

1) In systems IIa and IIb:

$$\sigma_1 = \frac{2x_H^2}{(1-x_1)(1-x_2)}(2-s_{13}^2),$$

$$\sigma_2 = \frac{x_H^2}{(1-x_1)(1-x_2)} \cdot s_{13}^2,$$

$$\sigma_3 = \frac{2x_H^2}{(1-x_1)(1-x_2)}(1-c_{13}^2),$$

$$\sigma_4 = \mp \frac{2x_H^2}{(1-x_1)(1-x_2)} \cdot s_{13}c_{13}$$

$$\sigma_7 = 2x_H \left[\frac{x_2}{1-x_2}(c_{13}-c_{12}) + \frac{x_1}{1-x_1}(1-c_{13}) \right]$$

$$\sigma_8 = \mp x_H\left[-\frac{x_2}{1-x_2}(s_{13}+s_{12})+\frac{x_1}{1-x_1}s_{13}\right]$$

$$\sigma_1' = -4(1+x_H)\,(2-s_{13}^2), \qquad \sigma_2' = -2(1+x_H)\,s_{13}^2,$$

$$\sigma_3' = -4(1+x_H)\,(1-c_{13}^2), \quad \sigma_4' = \pm 4(1+x_H)\cdot s_{13}c_{13};$$

2) In systems IIIa and IIIb:

$$\sigma_1 = \frac{2x_H^2}{(1-x_1)(1-x_2)}\cdot(2-s_{23}^2),$$

$$\sigma_2 = \frac{x_H^2}{(1-x_1)(1-x_2)}\cdot s_{23}^2,$$

$$\sigma_3 = \frac{2x_H^2}{(1-x_1)(1-x_2)}\cdot(1-c_{23}^2),$$

$$\sigma_4 = \mp\frac{2x_H^2}{(1-x_1)(1-x_2)}\cdot s_{23}c_{23}$$

$$\sigma_7 = 2x_H\left[\frac{x_2}{1-x_2}(c_{23}-1)-\frac{x_1}{1-x_1}(c_{23}-c_{21})\right],$$

$$\sigma_8 = \mp x_H\left[\frac{x_2}{1-x_2}s_{23}-\frac{x_1}{1-x_1}(s_{23}+s_{21})\right],$$

$$\sigma_1' = -4(1+x_H)\,(2-s_{23}^2), \qquad \sigma_2' = -2(1+x_H)\,s_{23}^2,$$

$$\sigma_3' = -4(1+x_H)\,(1-c_{23}^2), \quad \sigma_4' = \pm 4(1+x_H)\cdot s_{23}c_{23}.$$

The upper sign corresponds to systems IIa and IIIa, and the lower IIb and IIIb.

---

[1] *A. Djouadi.* The Anatomy of Electro-Weak Symmetry Breaking. Tome I: The Higgs boson in the Standard Model. arXiv: hep-ph/0503172v2, 2005; DOI: 10.1016 /j.physrep. 2007.10.004.

[2] *S.K. Abdullayev*. Standard model, properties of leptons and quarks. Baku, 2017, 276p. (in Azerbaijan).

[3] *V.M. Emelyanov*. Standard Model and its extensions, Moscow, FIZMATLIT, 2007, 584p. (in Russian).

[4] *P. Langacker.* The Standard Model and Beyond. CRS Press, 2010, 635p. DOI: http://dx.doi.org/10.1063/1.36182.

[5] *C. Partignani et al.* (Particle Data Group) Chin. Phys., 2016, C 40, p. 100001.

[6] *G. Aad* et al. ATLAS Collaboration Phys. Lett., 2012, B 716, p.1.

[7] *S. Chatrchyan et al.* CMS Collaboration Phys. Letters, 2012, B 716, p. 30.

[8] *V.A.Rubakov*. To the creation of new particle with Higgs boson properties on Big Hadron Collider, UFN, 2012, vol.182, №10, pp.1017-1025.

[9] *A.V. Lanev*. CMS collaboration results: Higgs boson and search of new physics UFN, 2014, vol. 184, № 9, pp. 996-1004.

[10] *D.I. Kazakov*. Higgs boson is discovered: what else? UFN, 2014, vol. 184, № 9, pp. 1004-1017.

[11] *F. Englert, R. Brout.* Broken Symmetry and the mass of gauge vector Mesons Phys. Rev. Letters, 1964, V.13, №9, p.321.

[12] *P.W. Higgs.* Broken Symmetries and the Masses of gauge Bosons. Phys. Rev. Letters, 1964, V.13, №16, p.508.

[13] *P.W. Higgs.* Spontaneous Symmetry Breakdown without Massless Bosons Phys. Rev., V. 145, 1966, p. 1156-1163.

[14] *G.S. Guralnik, C.R. Hagen, T.W. Kibble.* Global Conservation Laws and Massless Particles Phys. Rev. Lett., 1964, V. 13, pp. 585-587.

[15] *S.K. Abdullayev, M.Sh. Gojayev, F.A. Saddigh.* Decay Channels of the Standard Higgs boson Moscow University Physics Bulletin, 2017, v.72, №4. P. 329-339; VMU, series 3: Physics, Astronomy, 2017, №4, p.3-11.

[16] *S.K. Abdullayev, M.Sh. Gojayev, N.A. Nasibova.* Production of a scalar boson and fermion pair in arbitrarily polarized e^-e^+-beams. Russian Physics Journal, 2018, v.61, №1, p.94-101.

[17] *S.K. Abdullayev* and *M.Sh. Gojayev.* The Higgs bosons production in arbitrary polarized electron-positron colliding beams UZFF, 2018, No 1, pp. 1810101-1-10.

[18] *P. Nath.* Higgs physics and supersymmetry Int. J. Mod. Phys. A., 2012, V.27, No28, pp.123029.

[19] *R.K. Barman* et. al. Current status of MSSM Higgs sector with LHC 13 TeV data. arXiv: 1608.02573v3 [hep-ph] 23 May 2017.

[20] *Z. Hioki, T. Konishi, K. Ohkuma.* Studying possible CP-violating Higgs couplings through top-quark pair productions at muon colliders Journal of High Energy Physics, 2017, V. 7, No 07. arXiv: 0706.4346v2 [hep-ph], 2017.

[21] M. Greco. On the study of the Higgs properties at a muon collider Mod. Phys. Lett., A30, 2015, No. 39, pp. 1530031 [arXiv:1503.05046].

[22] *S. Jadach, R.A. Kycia.* Lineshape of the Higgs boson in future lepton colliders Phys. Lett. B755, 2016, pp.58-63 [arXiv:1509.02406].

[23] *K. Peters.* Prospects for beyond Standart Model Higgs Boson searches at future LHC runs and other machines. arXiv: 1701.05124v2 [hep-ex] 21 Feb 20.

[24] *S.K. Abdullayev, L.A. Agamaliyeva, M.Sh. Gocayev, F. Saddigh.* Investigation of Higgs boson formation in lepton-antilepton collisions GESJ: Physics, 2015, №1(13), p.36-55.

[25] *S.K. Abdullayev, L.A. Agamaliyeva, M.Sh. Gocayev.* Investigation of Higgs boson formation in deep-inelastic lepton-antilepton dispersion GESJ: Physics,2015, №2(14), p.28-40.

[26] *S.K. Abdullayev, M.Sh. Gojayev* and *F.A. Saddigh.* AJP. Fizika. Baku, V. XXI 2015, №2, pp.17-22.

[27] *S.K. Abdullayev, M.Sh. Gojayev and N.E. Nesibova*. AJP. Fizika, 2017, V. XXII, № 3, p.45-52.

[28] *S.K. Abdullayev, M.Sh. Gojayev*. Production and decay of Higgs bosons in muon collieders / X International conference «Modern trends in Physics», Baku, 2017, 20-22 April.

[29] LHC Higgs Cross Section Working Group Collaboration, de Florian D. et al. «Handbook of LHC Higgs Gross Sections: 4. Deciphering the nature of the Higgs Sector» arXiv: 1610.07922v1[hep-ph], 2016.

[30] *V.D. Shiltsev*. High-energy particle colliders: the past 20 years, the next 20 years, and the distant future UFN, 2012, V. 182, No 10, pp.1033-1046.

[31] *K.J.F. Gaemers, G.J. Gounaris.* Phys. Lett., 1978, B 77, No 4, pp. 379-382.

[32] *A. Djouadi J. Kalinovski, P.M. Zerwas.* Two- and Three-Body Decay Modes of SUSY Higgs Particles. arXiv: hep-ph / 9511342V1, 16 Nov, 1995.

[33] *A. Djouadi.* The Anatomy of Electro-Weak Symmetry Breaking. Tome II: arXiv: hep-ph/0503173v2, 2003;
DOI: 10.1016/j.physrep.2007.10.005

[34] *S.K. Abdullayev, M.Sh. Gojayev*. AJP: Fizika, XXIV (4), 11, 2018.

[35] *S.K. Abdullayev M.Sh. Gojayev*. Associated Production of a Higgs Boson and Heavy Fermion Pair in e^-e^+-collisions Moscow University Physics Bulletin, 2019, V. 74, No 1, pp.24-32.

[36] *S.K. Abdullaev, A.I. Mukhtarov*. Superstring Z'-boson in e^-e^+-annihilation PEPAN, 1995, V. 26, No 5, pp. 527-552.

[37] *S.K. Abdullaev, A.I. Mukhtarov*. Physics of Atomic Nuclei, 1997, V. 60, No 11, pp.1901-1919.

[38] *S.F.Hamilton*. CERN-THESIS-2014-008, 2014, p. 279.

Received: 22.10.2019

MONOPOLAR INJECTION CURRENTS IN THE LAYERS OF $Ge_XAs_YTe_{100-X-Y}$ SYSTEM

H.I. MAMMADOVA
G.M. Abdullayev Institute of Physics, NAS,
131, H. Javid ave., Baku, Azerbaijan
physics.humay@mail.ru

The features of current passage mechanism through sandwich of Te– $Ge_xAs_yTe_{100-x-y}$ Al structure type are investigated. It is established that the currents limited by space charges which are formed by hole monopolar injection, form from tellurium at positive potential on electrode. Using the Lambert's classic theory of injection currents, it is established that the electricity transfer is controlled by small trap centers situated between valence band and Fermi level. The parameters of the given centers are defined: the depth of occurrence and concentration. It is shown that the current in third VAC region increases in the region of trap filling limit not by vertically according to Lambert theory for monoenergetic levels of hole traps, but by power law. The given feature is explained by Pool-Frenkel effect taking under consideration the transition of the distribution function from Boltzmann approximation up to Fermi-Dirac one caused by the change of Fermi level position. The critical values of electric field strength at which the thermo-field decrease of Coulomb barrier up to zero blocking to thermo-field free current carriers are evaluated and the electric strength value at transition from trap quadratic law to non-trap one is defined.

Keywords: volt-ampere characteristic (VAC), Pool-Frenkel effect, Poisson equation.
PACS: 81.05. Gc

1. INTRODUCTION

Last years the interest in chalcogenide glass-like semiconductors (ChGS) on the base of S, Se and Te elements in combination with appropriate elements from Mendeleyev's table (Ge, As and etc.) has increased. This is caused by one hand by their unique properties, in particular, high transparency in IR spectrum, high value of refraction index, high optical nonlinearity and by other hand by technological process similarity necessary for applied tasks and also by possibility of unlimited doping and chemical composition variation causing to material obtaining with optimal parameters that allows us to widen the regions of their applications [1–4]. However, the achievements of applied goals require the material obtaining with predicted properties and optimal parameters necessary for concrete goals.

The many-component ChGS materials containing the elements differing by the valence electron number are the more suitable for the given goals. According to the rule ¸8-*N*' [atom with *N* valence electrons ($N \geq 4$) forms 8- *N* bonds, i.e. has 8-*N* close neighbors], coordination numbers of Ge, As and chalcogene (S, Se and Te) atoms are equal to 4, 3 and 2 correspondingly. Such difference in coordination number values promotes to change of glass matrix structure changing the chemical composition, i.e. allows us to obtain the glass with both one-dimensional and two- and three-dimensional structures. Such change in amorphous matrix should be accompanied by the change of electron properties. The investigation results of physical property peculiarities of ChGS system Ge-As-Se and their correlation with local structure parameters in scales of local and average atomic orders (correlation length, quazi-period in the region of average order, packing coefficient, compactness, average value of atomic volume, average coordination number, quantity of limits and cohesion energy and also the chemical bonds and their percent parts in the investigated materials) are presented in our works [5-6]. ChGS system marks out by parameters required for practical goals. In particular, it has the wide transparency window covering the wavelength interval 3-20 μm and high value of refraction index (n~3,5 at 1,55 μm wavelength) [7-8]. The investigation of crystallization kinetics [9] is predicted by perspective of the given material with low Ge concentration (<10 at%) for the use in optical record with reversible phase change. The investigation of reversible switching of memory [10] show that the given material can be mainly used for the readout of memory applications.

Taking under consideration the above mentioned we can conclude that the complex investigations of both atomic and energy structure and also physical properties of ChGS system Ge-As-Te are the actual ones. The investigation of charge transport mechanism through structures of Te--$Ge_xAs_yTe_{100-x-y}$--Al sandwich type is the aim of the present work.

2. EXPERIMENT TECHNIQUE AND SAMPLE PREPARATION

ChGS synthesis of $Ge_xAs_yTe_{100-x-y}$ system is carried out in following sequence: the purest elementary substances in required atomic percent are filled in quartz ampoules and after air exhaust they are heated up to temperature ~900 ^{0}C during 3 hours up to pressure 10^{-4} millimeter of mercury, further they are endured for about 12 hours at this temperature. The synthesis is carried out in rotating stove and the cooling is carried out in the off mode stove with aim of the promotion of sample homogeneity. The films of the different width used in the investigations are obtained by thermal evaporation with velocity 0,2÷0,4 μm/sec on glass substrates in vacuum at pressure 10^{-4} millimeter of mercury. The following

131, H. Javid ave., AZ-1143, Baku
ANAS, G.M. Abdullayev Institute of Physics
E-mail: jophphysics@gmail.com

ChGS compositions $Ge_{8,33}As_{16,67}Te_{75}$, $Ge_{10}As_{20}Te_{70}$, $Ge_{8,33}As_{16,67}Te_{62,5}$, $Ge_{18,2}As_{18,2}Te_{63,6}$ and $Ge_{18}As_{17}Te_{55}$ are synthesized.

The density of obtained samples ρ is measured by Archimed principle with the use of liquid (water) and it is calculated using the following formula:

$$\rho = \left[\frac{w_0}{(w_0 - w_L)}\right]\rho_L$$

where w_0 and w_L are material height in air and liquid correspondingly. ρ_L is liquid density (water) at room temperature is 1gr/cm^3. The measurement accuracy isn't less than ± 0.02 gr/cm^3.

VAC of Te--$Ge_xAs_yTe_{100-x-y}$--Al structure is investigated on constant current at application of electric strength of both polarities. The plane- parallel electrodes from aluminum and tellurium are also marked by vacuum evaporation. This square is 3,2 m^2. The space charge limited current (SCLC) mode is observed at the application of positive potential to Te, i.e. the holes are the injected charge carriers. The current values are registered by device 64876 Picoammetr voltage source (Keithley).

3. EXPERIMENTAL RESULTS AND THEIR DISCUSSION

VACs for ChGS of compositions $Ge_{8,33}As_{16,67}Te_{75}$, $Ge_{10}As_{20}Te_{70}$ and $Ge_{8,33}As_{16,67}Te_{62,5}$ at room temperature are shown in fig.1. The other compositions have the similar VACs.

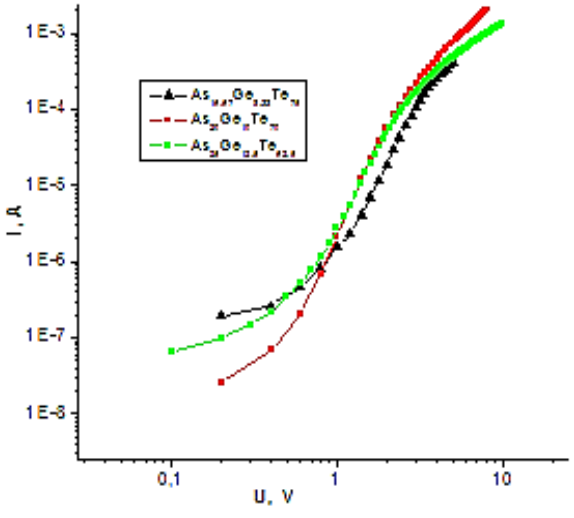

Fig. 1. VACs of ChGS compositions $Ge_{8,33}As_{16,67}Te_{75}$, $Ge_{10}As_{20}Te_{70}$ and $Ge_{8,33}As_{16,67}Te_{62,5}$.

As it is seen from the figure VACs of all compositions beginning from ohmic law with increasing voltage transit to the region corresponding to power law, i.e. $I \sim V^n$, where $n \approx 2$. Further, the section where $n>2$ which transits into the region where $n \approx 2$ with increasing voltage. According to injection current theory [11], such VAC behavior proves the fact that the electric charge transfer in the given materials is carried by the monopolar injection currents controlled by small trap capture centers for the holes situated below Fermi level. Using the classic theory of injection currents [11], some parameters controlling the electric charge transfer in wide interval of applied voltage are defined.

The values of specific resistance are calculated from VAC ohmic section and using them the concentrations of equilibrium free holes (table 1) are estimated according to formula $\rho=(ep_0\mu)^{-1}$, where e is elementary charge and μ is drift mobility of charge carriers. The mobility values are estimated using the component element mobility [12 -14] taking under the consideration their percent part in investigated ChGS compositions. Using these data Fermi level position in forbidden band (F_o–E_v) is defined by following formula:

$$p = N_V \exp(-\frac{F_0 - E_V}{kT}) \qquad (1)$$

where N_v is effective state density in valence band and for many chalcogenide glasses N_v =1020 cm^{-3} [15], κT is thermal energy.

In table 1 p_{01} is charge carrier concentration taking part in current passing in VAC section corresponding to Ohm law, F_{01}-E_v corresponds to Fermi level position; p_{02} are the given concentration values in the beginning region of non-trap quadratic law and F_{02}-E_v corresponds to Fermi quazi-level position.

Using the voltage values at which the current excursion begins (the region of Trap Filling Limit V_{TFL}) the concentration of attachment level which doesn't filled in thermodynamic equilibrium is defined by following formula [11]

$$p_{t,0} = 1{,}1 \cdot 10^6 \frac{\varepsilon V_{TFL}}{L^2}\ \text{cm}^{-3} \qquad (2)$$

where ε is relative dielectric constant which is also estimated using ε of component elements [16] taking into consideration their percent part in investigated ChGS compositions. As in our investigations the quadratic section precedes to almost vertical section of the characteristics (fig.1), so we can accept that $p_{t,0} = N_t$ according to [11]. Energy position of trap centers is estimated by following formula [11].

$$E_t - E_V = \text{kT} \ln\frac{N_V}{\theta g N_t} \qquad (3)$$

where θ is part of charge free carriers (holes) on all injected ones. Its values are defined as relation of current value corresponding to trap quadratic law to extrapolated current value from the section of non-trap quadratic law. The obtained values of concentration and energy position of trap centers are presented in table 1. The treatment of experimental results mentioned above, are carried out within the framework of Lambert theory [11] for injection currents in the solid states. According to theory began by Rous and continued by Lambert [11], the monopolar injection currents in the solid states (when one from the contacts is injecting one) have the following peculiarities: at low voltages of applied

field the charge transfer is carried out by thermal equilibrium carriers and obeys to Ohm law. The injected carrier concentration exceeds their equilibrium values with increasing voltage and Ohm law is exchanged by Mott -Gerni law [18], i.e. VAC obeys to law I~V^2L^{-3}. Here V is applied voltage, L is sample thickness (the distance between plane-parallel electrodes). In the case of the samples the part of injected carriers is captured by traps and don't take part in current passing. That's why the transition from ohmic law into quadratic one takes place at relative high voltages. At further increase of applied voltage the total filling of trap centers should be observed and the vertical increase of current value obeys to Mott-Gerni law without traps. However, in many cases in particular, in our experiments, the current excursion takes place not vertically and by power law (I~V^n). This fact is explained by Lambert and Rouse by the fact that trap centers aren't monoenergetic ones and their densities are exponentially distributed on energies [11,17]. The alternative explanations of such type VAC behavior in TFL region are shown by authors of [18] with accepting of Gaussian distribution of defect states.

However, note that the experiments on investigation of injected currents are carried out in wide interval of applied field, moreover, VAC section at which the current excursion is observed, corresponds to electric field strength $10^3 \div 10^4$ V/cm. At such high values of applied electric field strength, Pool-Frenkel effect (PF) influences on mechanism of current passing [19]. The mechanism of the given effect is in thermo-field release of charge carriers from Coulomb traps existing in material volume amplified by electric field [20]. The author of [20] taking under consideration that only monoenergetic defect states exist in materials and $(E_F - E_V)$>>kT condition carries out , proposes the formulae expressing the dependences of conductivity and current density on applied electric field strength caused by PF effect.

$$\sigma = Cexp\left(-\frac{e\varphi-\beta\sqrt{\varepsilon}}{\zeta kT}\right) \quad (4)$$

$$J = C\varepsilon exp\left(-\frac{e\varphi-\beta\sqrt{\varepsilon}}{\zeta kT}\right) \quad (5)$$

where σ is conductivity, J is current density, ε is electric field strength, β and C numerical parameters depending on material, k is Boltzman constant, ζ is inclination parameter of PF effect which varies between 1 and 2 in the dependence on concentration of acceptor traps. In work [19] this parameter is equal to 2.

The last equation can be written in the form:

$$\ln\frac{j}{\varepsilon} = \frac{\beta}{\zeta kT}\sqrt{\varepsilon} + \left[lnC - \frac{e\varphi}{\zeta kT}\right] \quad (6)$$

The dependence $ln\frac{j}{\varepsilon} \sim \sqrt{\varepsilon}$ in VAC region corresponding to current excursion is presented in fig. 2. Parameter β, the values of which are also presented in table 1, is defined from inclination of the given graph ($\frac{\beta}{\zeta kT}$).

For the first time the authors of works [21, 22] developed the theory of monopolar injection currents using the classic model of PF effect. In classic PF model [23] it is proposed that firstly, the existing of the monoenergetic levels; secondly, $E_F - E_V \gg kT$, i.e. Boltzmann approximation is correct for energetic distribution of charge carriers in allowed bands.

VACs constructed according to model proposed in [21, 22] at low voltages well correspond to Lambert theory but at high electric field strengths the results strongly differ with both SCLC theory and experimental results. This is explained by the fact that Boltzmann approximation is accepted for both free and captured carriers. In modern PF models Boltzmann approximation is applied for free charge carriers and Fermi-Dirac distribution is used for captured carriers. Indeed, the current passing is carried out by thermal-equilibrium holes at low values of applied voltage and obey to Ohm law. Moreover, Fermi levels locate in the middle of forbidden band, i.e. far from trap center level. The use of Boltzmann distribution is reasonable one. The concentration of injected holes with increasing voltage strongly increases and position of Fermi quazi-level approximates to energetic position of trap centers (table 1). That's why it is more real to use Fermi-Dirac distribution. The observable VAC peculiarities at the use of classic and modern model, mainly reveal at high values of applied voltage. In first case the current increases as quadratic one with participation of small traps. And in second case the current strongly increases similar to TFL low as in SCLC. However, the non-trap quadratic law at this isn't observed that it should take place according to Lambert theory. According to [20] such disagreement is connected with inaccuracy at Poisson equation formation which has the following general form:

$$\frac{d\varepsilon}{dx} = \frac{\rho+\rho_t}{\varepsilon} \approx \frac{\rho_t}{\varepsilon} \quad (7)$$

Here $\mathcal{E}$ is applied electric field strength, ρ and ρ_t are densities of free and captured charge carriers (holes), ε is dielectric constant of investigated ChGS compositions. In works [21, 22] at solving of Poisson equation ρ doesn't take under consideration, so $\rho \ll \rho_t$. Such approximation is correct at small voltages, i.e. when VAC region isn't reached, where TFL law is satisfied. That's why VAC in the given region agrees with Lambert theory. Upon reaching voltage V_{TFL} the current density values strongly increase, i.e. the transition in the region of non-trap quadratic law doesn't take place. The author of work [23] giving the refinements in Poisson equation taking under consideration both captured and free charges, obtains VAC consisting in three sections predicted by Lambert theory with the difference that the transition from trap quadratic law in non-trap one takes place not vertically, but by power law. The values of electric field strength, at which the height of Coulomb barrier decreases up to zero (saturation of electric field strength of PF effect is ε_S) and the transition from current excursion with into non-trap quadratic law

(ε_{TFL}) with increasing voltage takes place, are evaluated (table 1) by following formulae proposed by author of work [23]:

$$\varepsilon_S = \left(\frac{e\varphi}{\beta}\right)^2 \quad (8)$$

$$\varepsilon_{TFL} = \frac{eN_tL}{\varepsilon} \quad (9)$$

where $e\varphi$ is height of a Coulomb barrier for the carriers captured by trap centers that is equal to their energy depth of occurrence, N_t is trap center concentration, ε is dielectric constant, L is film thickness. As it is seen from the table, ε_S values are almost an order greater than ε_{TFL}. Indeed, at ε_{TFL} all trap centers are filled by electrons according to classic theory of injected currents. And at ε_S the depletion of the given centers which still aren't fully captured by carriers takes place. That's why its value are less than required values of electric field strength (ε_{TFL}) for carrying out of the transition from the trap quadratic law to non-trap one. It is known that the defect states in chalcogenide glass-like semiconductors is connected with broken chemical bonds, nano-voids, with existence of many structural elements, relative quantities of homeopolar and heteropolar bonds and etc. By other words, they are connected with peculiarities of short-range order in atom disposition. For the establishment of the given position the densities of all investigated compositions are measured and such parameters of short-range order as packing coefficient [24] and R parameter defined by ratio of number of possible chalcogene atom covalent bonds to the number of non-chalcogenide one [25].

$$\delta = \frac{\sum_i (x_i A_i)/\rho_i - \sum_i (x_i A_i)/\rho}{\sum_i (x_i A_i)/\rho} \quad (10)$$

where ρ and ρ_i are densities of chemical compositions and elements including in ChGS composition.

R =1 presents itself the case of stoichiometric composition consisting only from energy profitable heteropolar bonds. R>1 values correspond to chemical compositions rich by tellurium (samples with numbers 1 and 2 in the table) in which homeopolar bonds Te-Te also take place along with existence of heteropolar bonds As-Te and Ge-Te. At R<1 values the chemical compositions differ by deficiency of chalcogene atoms for total satisfaction of valence requirements of non-chalcogene atoms (samples 4 and 5, table). As it is seen from the table the least values of trap center concentrations correspond to ChGS composition $As_{25}Ge_{12.5}Te_{62.5}$ where R=1. According to principles of chemical bond methods (Chemical bond approaches (CBA) model) [7] the probability of heteropolar bond formation exceeds the probability of homeopolar bond one, moreover, firstly the strongest bonds are formed (bonds with high energies).

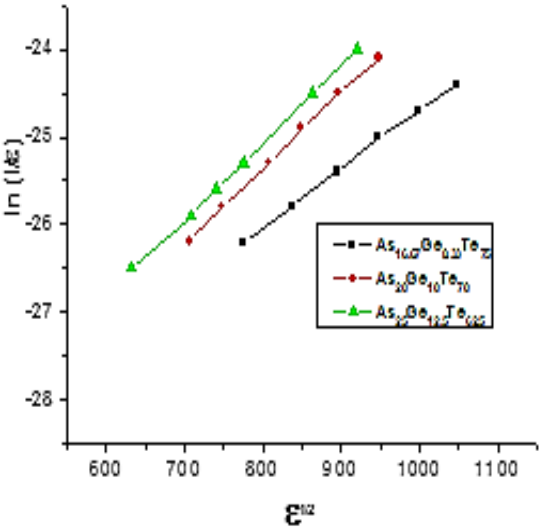

Fig. 2. $\ln \frac{j}{\varepsilon} \sim \sqrt{\varepsilon}$ dependence for ChGS compositions $Ge_{8,33}As_{16,67}Te_{75}$, $Ge_{10}As_{20}Te_{70}$ and $Ge_{8,33}As_{16,67}Te_{62,5}$ in VAC region corresponding to current excursion.

Table 1

The parameters of local states controlling the current passing through Al--$As_xGe_yTe_{100-x-y}$ --Te structure.

	$As_{16.67}Ge_{8.33}Te_{75}$	$As_{20}Ge_{10}Te_{70}$	$As_{25}Ge_{12.5}Te_{62.5}$	$As_{18.2}Ge_{18.2}Te_{63.6}$	$As_{17}Ge_{28}Te_{55}$
R	1.8	1.4	1	0.998	0.675
δ	0.016	-0.152	-0.015	-0.003	-0.002
θ	$9*10^{-3}$	$4*10^{-3}$	$6*10^{-3}$	$8*10^{-3}$	10^{-2}
ε	23.18	22.32	21.03	21.44	20.21
μ, ($cm^2/V\cdot s$)	29.78	32.34	36.18	38.51	46.22
p_{01}, cm^{-3}	$8.07*10^8$	$2.93*10^8$	$4.31*10^8$	$2.14*10^8$	$1.54*10^8$
F_{01}-E_v, eV	0.661	0.687	0.677	0.695	0.704
p_{t0}, cm^{-3}	$2.9*10^{15}$	$2.8*10^{15}$	$2.6*10^{15}$	$3.2*10^{15}$	$3.9*10^{15}$
E_{t1}-E_v, eV	0.374	0.397	0.388	0.375	0.364
p_{02},cm^{-3}	$9*10^{12}$	$13*10^{12}$	$8.5*10^{12}$	$4.72*10^{12}$	$1.44*10^{12}$
F_{02}-E_v, eV	0.420	0.410	0.421	0.436	0.467
β, $C(m/V)^{1/2}$	$6*10^{-23}$	$9*10^{-23}$	$7*10^{-23}$	$8*10^{-23}$	$6.2*10^{-23}$
$\mathcal{E}_S$, V/cm	$9.3*10^3$	$5*10^3$	$7.8*10^3$	$5.6*10^3$	$8.8*10^3$
$\mathcal{E}_{TFL}$, V/cm	$4.52*10^4$	$4.54*10^4$	$4.47*10^4$	$5.39*10^4$	$6.97*10^4$

Thus, amorphous matrix of the given composition is formed mainly from heteropolar bonds. From above mentioned we conclude that the matrix of the given composition is the more perfect.

The main principles of chemical bond method (Chemical bond approaches (CBA) model) [26] are used in this goal. According to CBA the probability of heteropolar bond formation exceeds the homeopolar one, moreover, firstly the strongest bonds form (bonds with high energies). The consistency of given bond formation corresponds to consistency of energy decrease until the achievable atom valence won't be satisfied. Finally, according to CBA the bond energy is additive one. The supposed chemical formulae of the investigated compositions taking under consideration of the given principles are presented in table 1. In third composition the glass structure consists in totally matched tetrahedral and pyramidal structural units which have energy profitable heteropolar bonds. In 1st, 2nd and 4rd compositions along with the given element the homeopolar bonds between chalcogene atoms are also take part, i.e. the excess selenium atoms take part in bounding of given elements and also join between each other in chain and ring formation.

[1] *A. Zakery* and *S. Elliott*. Journal of Non-Crystalline Solids,2003, v.330,Iss.1–3,pp.1–12.

[2] *J.S. Sanghera* and *I.D. Aggarwal.* Journal of Non-Crystalline Solids, 1999, vol. 256–257(0), pp. 6–16.

[3] *J.M. Harbold, F.O. Ilday, F.W. Wise* and *B.G. Aitken.* IEEE Photonics Technology Letters, 2002, v.14(6), p.822–824.

[4] *K.D. Zendin.* Electron phenomena in chalcogenide glass-like semiconductors, Science, 1996, p. 486.

[5] *A.I. Isayev, Si.I.Mehdiyeva, H.I. Mamedova, R.I. Alekberov.* FTP, №11, 2019,pp.1532-1539.

[6] *S.I. Mekhtieva, A.I. Isayev, R.I. Alekberov, H.I. Mamedova.* AJP Fizika, 2018, vol. XXIV № 2, section: En, p.3-9

[7] *Z.Y. Yang* and *P. Lucas.* Tellurium-based far-infrared transmitting glasses. J. Am. Ceram. Soc. 92, 2920–2923, 2009.

[8] *P. Hawlová, F. Verger, V. Nazabal, R. Boidin* and *P. Němec.* Accurate determination of optical functions of Ge–As–Te glasses via spectroscopic ellipsometry. J. Am. Ceram. Soc. 97, 3044–3047 (2014).

[9] *R.M.Mehra, A.Pundir, A.Kapoor, P.C.Mathur.* J. Optics (Paris) 27, 139, 1996.

[10] *S. Prakash, S. Asokan, D.B. Ghare*. J. Phys. D Appl. Phys.29, 2004 (1996).

[11] *M. Lambert, P. Mark,* Injection currents in the solid states, M., Mir, 1973, p. 413.

[12] *Tuan T. Tran* 1*, Jennifer Wong-Leung[1] et all, Non-localized states and high hole mobility in amorphous germanium, Preprint August 2019.

[13] *Katsuro Okuyama* and *Yasuji Kimagai.* Japanese Journal of Applied Physics, vol. 12, №12, December, 1973.

[14] *Bart J. Van Zeghbroeck*. Electrical characterization of GaN/SiC n-pn-p heterojunction diodes. Appl. Phys. Lett. 72, 1371, 1998.

[15] *N.F. Mott, E.A. Devis.* Electron processes in non-crystalline substances, M., Mir, 1982, p.662.

[16] *K.F. Young* and *H.P. R. Frederikse.* Journal of Physical and Chemical Reference Data, v. 2, №2, 1973, pp. 313–409.

[17] *A. Rose.* Space-Charge-Limited Currents in Solids, Phys. Rev. 97, 1538, 1955.

[18] *N.F. Mott* and *R.W. Gurney*. Electronic Processes in Ionic Crystals (Oxford University Press, London, 1940). *H.T. Nicolai, M.M. Mandoc,* and *P.W. M. Blom*. Phys. Rev. B 83, 195204, 2011.

[19] *J. Frenkel. Physical Review*, 54, No.8, pp. 647-648, October 15, 1938.

[20] *W.R. Harrell.* "Poole-Frenkel Conduction in Silicon Dioxide Films, and Implications for Hot-Carrier Degradation in *n*- MOS Devices", Doctoral Dissertation, University of Maryland, 1994.

[21] *P.N. Murgatroyd.* "J. Phys. D: Appl. Phys., vol. 3, pp. 51-56, 1970.

[22] *D.F. Barbe.* J. Phys. D: Appl. Phys., vol. 4, pp. 1812-1815, 1971.

[23] *Satoshi Takeshita*. Modeling of space-charge-limited current injection incorporating an advanced model of the Poole-Frenkel effect. 2008.

[24] *V. Pamukchieva, A. Szekeres, K. Todorova, M. Fabian, E. Svab, Z. Revay, L. Szentmiklosi.* No search results found for Journal of Non-Crystalline Solids, 2009, v. 355, pp.2485-2490.

[25] *L. Tichy, H. Ticha.* On the chemical threshold in chalcogenide glasses. Mater. Lett.,1994, v.21, pp. 313-319.

[26] *A.S. Hassanien, A.A. Akl.* Journal of Non-Crystalline Solids, 2015, vol. 428, pp. 112-120.

Received: 21.10.2019

INVESTIGATION OF PIXEL CAPACITANCE AND SHUNT CAPACITANCE OF SILICON PHOTOMULTIPLIER

A. MAMMADLI[1], N. SULEYMANOVA[1], R. AKBEROV[2], S. NURUYEV[3], N. SADIGOVA[3], A. HUSEYNOVA[3], A. GERAYEVA[3], F. AGAYEVA[4]

[1]Center of Strategic Research of ANAS
[2] National Nuclear Research Center
[3]Institute of Radiation Problems of ANAS
[4] Azerbaijan State Oil and Industrial University
30, Istiglaliyyat str., Baku, AZ1001
Email: arzu_memmedli_92@mail.ru

The investigation results of the modern silicon avalanche photomultiplier capacitance are presented. A photodiode of the well-known manufacturer Hamamatsu by the S13360-1325CS series was chosen as the test sample. Experimental and theoretical methods were used to determine the capacitance of pixels and the shunt capacitance of the photodiode.

Keywords: silicon photomultiplier, capacitance, parasitic capacitance, multi pixel photon counter.
PACS: 85.30.−z; 85.60. Dw

INTRODUCTION

The development of high-energy physics, nuclear medicine, and cosmology required the development of high sensitive detectors that could replace traditional vacuum photomultiplier tubes (PMTs). One of the first silicon photodiodes with performance characteristics comparable to modern PMTs is described in [1]. These structures have launched a new generation of semiconductor photodetectors. More than 20 commercial organizations and numerous research institutes around the world are improving silicon photodetectors and use them in detector systems in areas such as medicine, LIDAR, high-energy physics, and optoelectronics [2-3]. Insensitivity to magnetic fields and high photo detection efficiency made it possible to use silicon photomultipliers (SiPMs) in such international research centers as CERN, JINR and others. There are a lot of works regarding on performance of photodiodes [4-6], however, insufficient attention was paid to the determination and identification of photodetector's parasitic capacitance. One of the main problems of SiPMs today is the small active area and the lack of speed, which limits their use in time of flight experiments and large scale detectors of high-energy physics. The fact is that an increase in the size of photodiodes leads to an increase in capacitances, both of the photodiode itself and parasitic capacitances which play a key role in the detector's recovery time, avalanche gain, and photo response.

EXPERIMENTAL SETUP AND RESULTS

At the first stage of checking the circuit and measurement method, a HAMAMATSU photodiode S13360-1325CS [7] series was measured (60pF photodiode capacitance according to the manufacturer). It is known that the temporal characteristics of a photodiode are determined by the product of its two factors - resistance and capacitance (R*C). To determine the photodiode resistance, we used the method of measuring the volt-ampere characteristics. The technique is to connect the photodiode in the direction of forward bias. The voltage from the Keithley 6487 picoammeter was applied until (+ 1.3V) revealing the full linearity of the function (fig. 1), where the applied voltage completely drops to the quenching resistance R_q of the photodiode.

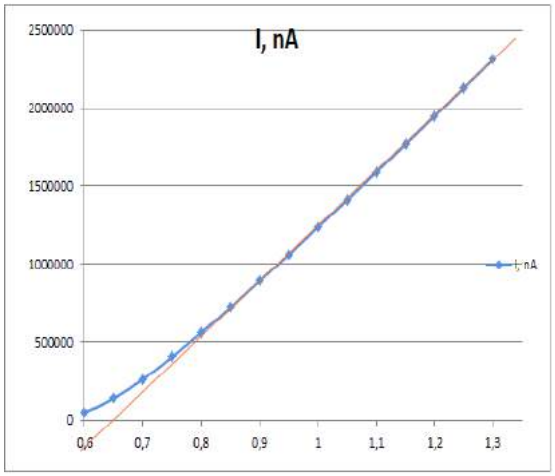

Fig. 1. Volt-ampere characteristic of the forward bias of the photodiode.

From the obtained volt-ampere characteristics the resistance R_q is calculated as follows:

$$R_q = \frac{\Delta U}{\Delta I} \approx 280\ [Ohm]$$

A standard circuit (fig. 2, left) for measuring and comparing capacities of photodiodes has been assembled. The AFG3202 generator supplied a pulsed signal U_g is 300 mV. A signal was taken from the Hantek oscilloscope (fig. 2, right).

131, H. Javid ave., AZ-1143, Baku
ANAS, G.M. Abdullayev Institute of Physics
E-mail: jophphysics@gmail.com

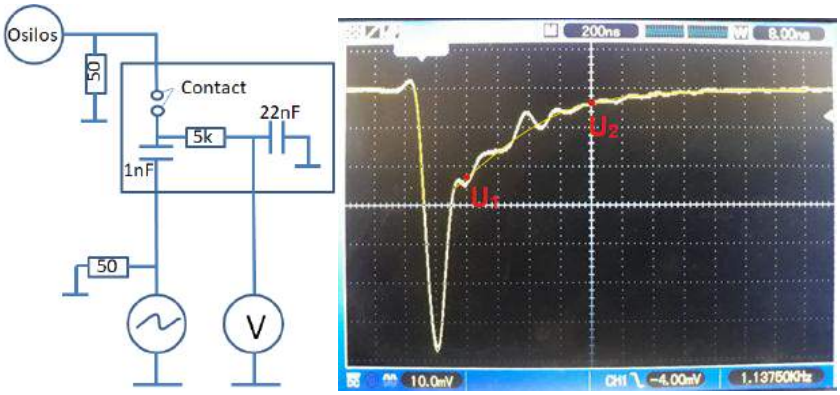

Fig. 2. Experimental design (left), signal from HAMAMATSU S13360-1325CS photodiode (right).

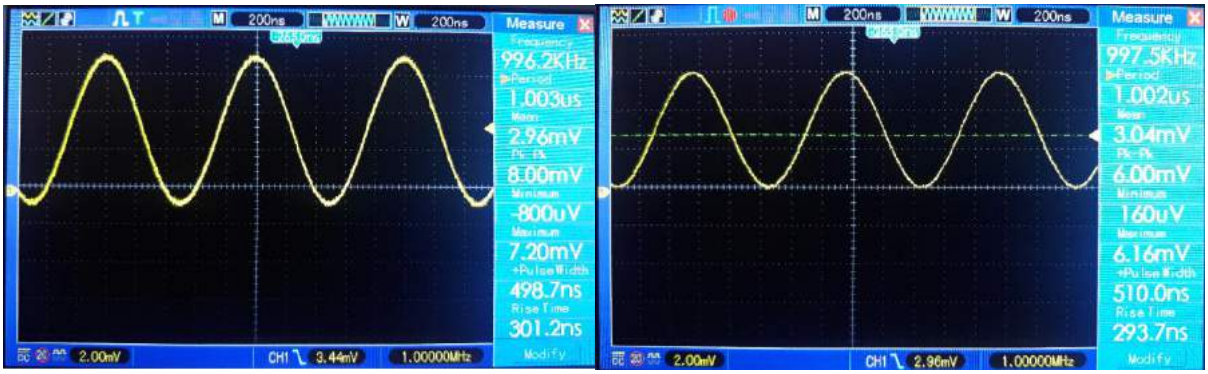

Fig. 3. Sinusoidal signal from photodiode (left), from reference capacitor (right).

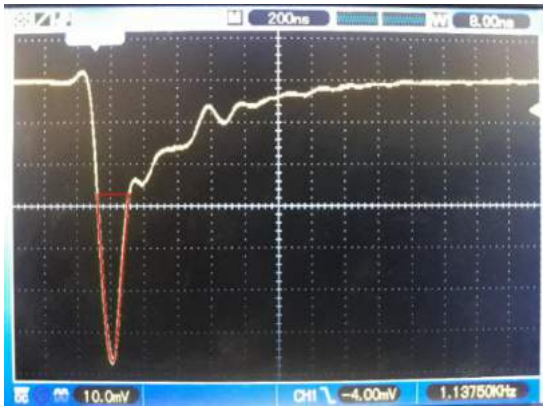

Fig. 4. Front view of the signal, regarding parasitic capacitance.

The main part of R*C is approximated and two arbitrary points (red points) of the exponent of the function (U_1, U_2) are taken and calculated by the following definition:

$$U = U_0 e^{-\frac{t}{RC}}$$

$$U_1 = U_0 e^{-\frac{t_1}{RC}}$$

$$U_2 = U_0 e^{-\frac{t_2}{RC}}$$

$$\frac{U_1}{U_2} = e^{\frac{t_2 - t_1}{RC}}$$

$$C = \frac{\Delta t}{R * ln\frac{U_1}{U_2}} \quad (1)$$

where U_1 is the value at time t_1, U_2 is the value at time t_2, C is the capacitance of the photodiode, R is the total resistance taking into account the resistance of the system (load resistor 50 Ohm).

$$R = R_{SiPM} + R_{load} = 280 + 50 = 330$$

Capacitance of diode is calculated from the definition (1),

$$C = \frac{32 * 10^{-9}}{330 * ln\frac{23.27}{3.79}} = 49{,}4 * 10^{-12}[F]$$

To verify the result, we calculate the capacitance of the photodiode (power supply is 50V; generator: 1MHz, +200mV, -200mV) according to the sinusoidal method (fig. 3, left):

$$Z = \frac{1}{\omega C}$$

$$I = \frac{U_R}{\frac{1}{\omega C}} = U_R 2\pi f C = \frac{U_R}{R} = \frac{4 * 10^{-3}}{50} = 8 * 10^{-5}$$

$$C = \frac{8*10^{-5}}{6.28*10^6*0.2} = 6.37 * 10^{-11} =$$

$$= 63.7 * 10^{-12}[F]$$

where Z is the resistance of the capacitor, U_R is voltage drop on the load resistance R, f is frequency

of the sine wave. The error of this measurement is determined by the error of the used oscilloscope, in our case the error of the result is 5%.

To confirm the experimental measurement system (without changing the equipment parameters), a nominal capacitance of 47pF was applied (Figure 3 right).

$$\frac{A_1}{A_2} * 47 * 10^{-12} = 62{,}7 * 10^{-12}[\Phi]$$

A_1-amplitude when measuring the photodiode (4 mV), A_2-amplitude when measuring the nominal capacitance (3 mV). Obtained value of capacitance is confirmed by experimental data.

It is known that, the front of the signal contains a charge (fig. 4), shunting capacitance C_s (parasitic capacitance of pixels). The charge of parasitic capacitance:

$$Q = \frac{U * t}{2R} = \frac{4 * 10^{-3} * 8 * 10^{-9}}{2 * 50} = 3{,}2 * 10^{-12}$$

$$Q = U_g C_s = 3{,}2 * 10^{-12}$$

$$C_s = \frac{Q}{U_g} = \frac{3{,}2 * 10^{-12}}{0.3} = 10666 * 10^{-15}[F]$$

Based on calculations, where the pixel capacitance of the photodiode is 49.4 pF (according to the manufacturer, this photodiode capacitance is 60 pF, experimentally 62.7 pF). The missing part, ~62.7-49.4=13.3 pF, is the parasitic capacitance of the photodiode.

As shown in the calculations, the parasitic capacitance, which plays a key role in the formation of the front edge of the pulse, occupies about 21 % of the total capacitance of the photodiode. Theoretically and experimentally, with an accuracy of 5%, the capacitance of the HAMAMATSU S13360-1325CS photodiode was determined to be 60 pF according to the manufacturer.

ACKNOWLEDGEMENT

This work is supported by science foundation SOCAR.

[1] *Z. Sadygov, A. Olshevski, I. Chirikov, I. Zheleznykh, A. Novikov.* Nucl. Instrum.and Methods in Phys. Res. A 567, 2006, 70–73.

[2] *R. Agishev et al.* "Lidar with SiPM: Some capabilities and limitationsin real environment," Optics and Laser Technology, v. 49, pp.86–90, 2013.

[3] *M. Perenzoni* et al. IEEE Journal of Solid-StateCircuits, vol. 52, № 1, pp. 151–160, 2017.

[4] *Z. Sadygov, F. Ahmadov, G. Ahmadov, A. Sadigov, S.Suleymanov, R. Madatov*. "Nuclear Instruments and Methods in Physics Research Section A824, 2016, p.137–138.

[5] *A. Sadigov, F. Ahmadov , S. Suleymanov , G. Ahmadov , Z. Sadygov*. International Journal of Advanced Research in Physical Science (IJARPS), v.3, № 2, 2016, p.9-19.

[6] *S. Nuriyev, F. Ahmadov, R. Akberov,G.Ahmadov, Z. Sadygov, A. Sadigov, S.Suleymanov*. Nuclear Instruments and Methods in Physics Research, vol. 912, pp. 320-322.

[7] https://hamamatsu.su/media/index/?type=catalog&id=50.

Received: 14.11.2019

ISSN 1028-8546

2019, Vol. XXV, № 4
Section: En

CONTENTS